On topological properties of massless fermions in a magnetic field

Lemut, G.

On topological properties of massless fermions in a magnetic field

Proefschrift

ter verkrijging van
de graad van doctor aan de Universiteit Leiden,
op gezag van rector magnificus prof. dr. ir. H. Bijl,
volgens besluit van het college voor promoties
te verdedigen op dinsdag 13 juni 2023
klokke 13.45 uur

door

Gal Lemut

geboren te Postojna (Slovenië)
in 1994

Promotores:	Prof. dr. C. W. J. Beenakker
	Prof. dr. İ. Adagideli (Sabancı University, Istanbul)
Promotiecommissie:	dr. A. R. Akhmerov (Delft University of Technology)
	prof. dr. ir. A. Brinkman (University of Twente)
	prof. dr. J. Aarts
	prof. dr. A. Achúcarro
	dr. M. Allan

Casimir PhD series, Delft-Leiden 2023-13
ISBN 978-90-8593-561-2
An electronic version of this thesis can be found
at https://openaccess.leidenuniv.nl

To Betti, to my friends and to my family.

Contents

1 Introduction

1.1 Preface

Electrons are massive, charged, elementary particles with a half-integer spin, that govern the behavior of most atoms and materials. In condensed matter physics, quantum mechanics is used to predict their behavior, leading to remarkable and sometimes counter intuitive phenomena. While free electrons in vacuum are well understood, in condensed matter systems, electrons acquire unusual properties from their interaction with the atomic lattice.

Since the discovery of the mono-layered carbon crystal graphene [1, 2] we know, that they can behave as massless particles called Dirac and Weyl fermions. These exist as low energy excitations giving electrons relativistic behaviour on non-relativistic-scales with a constant velocity analogous to the speed of light. In other systems where superconductivity [3] is present electrons can exhibit transport without resistance as a consequence of a Cooper pair condensate. This allows for exotic Bogoliubov excitations that unlike free electrons are not eigenstates of charge. Under special circumstances such Bogoliubov excitations can mimic special Majorana particles. In these systems electron excitations uniquely act as their own anti-particles [4]. While such states were first predicted in particle physics it turns out that they can be realized as elementary excitations in topological superconductors.

These examples highlight that, despite their apparent simplicity, electrons can exhibit a plethora of fascinating quasi-particle excitations in condensed matter systems. This thesis will examine the interplay of the above mentioned phenomena that arise in robust systems as a consequence of different symmetries as well as topological properties [5]. We will examine how such massless Dirac, Weyl, and Majorana quasi-particles interact with the magnetic field giving rise to new and unique phenomena. In particular, this thesis will examine the formation of zeroth Landau levels in superconducting systems, find transport signatures in Weyl superconductors [6, 7], as well as study a new type of delocalized solutions in the Fu-Kane model [8]. It will explore disordered massless systems, finding new

predictions of localized states as well as unique spectral properties. Finally, it will study the recently predicted Kramers-Weyl semimetals [9, 10] and show a new characteristic signature of the magneto-conductance.

While this thesis covers various different realizations of massless systems, the rest of this chapter will focus on introducing two of the most relevant and recently discovered systems. After a brief demonstration how massless fermions can arise in condensed matter system we will firsly show how the interplay between Dirac states in a topological insulator and superconductivity [11, 12] can give rise to the so called Fu-Kane model. This part will describe how such a model can exhibit a transition between a gapped and a gapless phase, as well as how this transition can interplay with the magnetic field to create Majorana excitations. Second, we will focus on a recent realization of three-dimensional Weyl fermions [13], demonstrating their special topological protection and discussing their surface states, which give rise to new characteristic signatures.

1.2 Massless fermions in electronic systems

In the field of condensed matter physics, our focus lies on the study of electrons far away from the relativistic limit. To predict their dynamics, we use the well known Schrödinger equation

$$i\hbar\partial_t\Psi = \left(-\frac{\hbar^2}{2m}\nabla^2 + V\right)\Psi. \tag{1.1}$$

The right-hand side consists of two terms, $-\frac{\hbar^2}{2m}\nabla^2$ represents the kinetic part, while $V(x)$ describes the potential felt by the particles. When the potential term is vanishing, the equation describes free electrons with the well known quadratic dispersion relation

$$E = \frac{p^2}{2m}, \tag{1.2}$$

connecting the energy and momentum. When electrons interact with the environment through the potential $V(x)$, we can no longer write down such a dispersion relation, as momentum is no longer a good quantum number. In condensed matter physics, we are mostly interested in the behaviour of electrons inside crystal structures. These can be described by a periodic potential that arises from the atomic structure. As a consequence of this periodicity, we can define a new quasi-momentum quantum number that forms a translationally invariant eigenspace.This quasi-momentum is restricted to the finite Brillouin zone due to the periodic structure of the

potential. In such basisc we can diagonalize the Hamiltonians of crystalline systems and find new quasi-momentum dispersion relations.

For different forms of periodic potentials, the relation between the energies and quasi-momentum can take diverse forms. While the dispersion now has to be periodic, in the simplest example, it still remains effectively quadratic around the center of the Brillouin zone. As the quadratic curvature can change, it can influence low-energy behaviour, altering the effective mass of the low energy excitations. This can give rise to very heavy quasi-particles with a flattened dispersionc as well as light excitations with a vanishing effective mass.

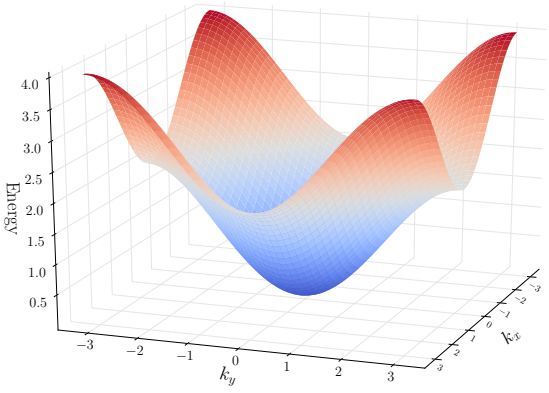

Figure 1.1: Example of a single band tight-binding Cosine dispersion. The dispersion around the minima of the band resembles free electron quadratic dispersion relation with a renormalized effective mass.

When the effective mass of elementary excitations becomes sufficiently small, the corresponding quasi-particles need to be described by a relativistic theory. In this limit, we have to include a spinor degree of freedom to satisfy the relativistic symmetries. These spinors can arise from the various orbital degrees of freedom as well as the actual electron spin. In such systems, we can describe the elementary excitations of electrons, using the full relativistic Dirac equation. In two-dimensional case, this reduces to

$$i\hbar\partial_t\Psi = (v_f\sigma_x k_x + v_f\sigma_y k_y + M_{eff}\sigma_z)\Psi, \tag{1.3}$$

where we have assumed an isotropic Fermi velocity v_f and used σ to denote the two-dimensional Pauli matrices. Such an effective theory describes two species of quasi-particle excitations with symmetric dispersions

$$E_{\pm} = \pm\sqrt{v_f^2 k_x^2 + v_f^2 k_x^2 + M_{\text{eff}}^2}. \tag{1.4}$$

In general, most crystals can exhibit perturbations that keep such an effective mass term finite. In such systems, the quasi-particle dispersion is gapped with a quadratic behaviour for small momentum. However, some crystals exhibit special symmetries that disallow such an effective mass. In such cases, the two bands of the dispersion cross, resulting in a fully gapless quasi-particle dispersion

$$E_{\pm} = \pm v_f |\vec{k}|. \tag{1.5}$$

These special types of quasi-particles, called massless fermions, exhibit a relativistic linear dispersion. They propagate at a constant velocity v_f mimicking the behaviour of photons. Such massless excitations can be generalized to different dimensions, giving rise to Majorana, Dirac and Weyl quasi-particles. While these can arise as a consequence of various crystalline symmetries, their protection can be understood using topological arguments. With these, it is possible to prove the robustness of such emergent relativistic excitations as well as the universality of their unique properties.

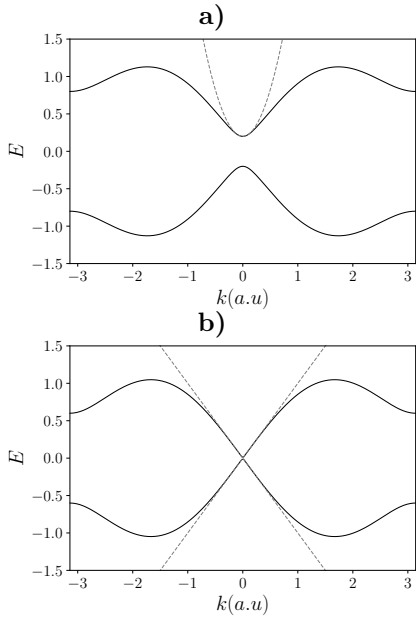

Figure 1.2: (a) Dispersion around an avoided band crossing with a quadratic behaviour around the band minima. (b) An example of a system where the band crossing is protected, giving rise to a gapless point in momentum space with a linear dispersion.

1.3 Dirac fermions to superconducting Majorana excitations

In condensed matter physics, two dimensional massless fermions are called Dirac fermions. They can be described by the two dimensional Dirac equation where a special symmetry prevents the additional mass term. Nature presents us with various mechanisms that can protect these quasi-particle excitations. One of the most famous examples is the single layer carbon crystal graphene where its two gapless Dirac points are protected by an approximate sublattice symmetry arising from the underlying hexagonal lattice.

This thesis explores a more recent realization of Dirac fermions, specifically surface excitations of a three-dimensional topological insulator. In such systems, each surface exhibits a strongly protected Dirac cone due to time-reversal symmetry. We will examine how the interplay between

such Dirac states and superconductivity gives rise to the Fu-Kane topological superconductor. While superconductivity in general gaps out the Dirac fermions it is well known that in this model strong supercurrent can be used to restore such gapless points. We have found that such supercurrents can induce another transition in the presence of magnetic field, where Majorana zero-modes extend into a novel extended superconducting state resembling a Landau level. To combine all these ingredients we will first focus on the way the magnetic field affects massless fermions. We will then examine the proximity effect and the Fu-Kane model and finally combine all these ingredients to discuss the Majorana zero energy excitations.

1.3.1 Zeroth Landau level in a 3D topological insulator

We start by introducing the three-dimensional topological insulator. We generally define insulators as non-conducting systems characterized by a large gap around the Fermi energy. Such gapped insulating systems are classified as trivial if they can be continuously transformed into the atomic limit and are therefore topologically equivalent to the vacuum. However, not all insulators can be described in this way. There exists a special type of insulator that cannot be transformed into the atomic limit without closing the band-gap. These systems are called topological insulators and are characterized by special edge states that arise from the gap closing on the interface between the topologically non-trivial insulating bulk and the trivial vacuum. In three dimensions, such topological insulators exhibit two-dimensional surface states, which can be described by the effective surface model

$$H_{\mathrm{TI}} = \tau_z \sigma_x k_x + \tau_z \sigma_y k_y + \tau_x \sigma_0 M(\vec{k}). \tag{1.6}$$

Each surface of the three-dimensional topological insulator, represented by Pauli matrices τ, exhibits a single Dirac fermion coupled together by an effective mass term $M(\vec{k})$. The surfaces become fully decoupled when they are separated from each other. In this limit, each surface exhibits a single Dirac fermion that is protected by the time-reversal symmetry.

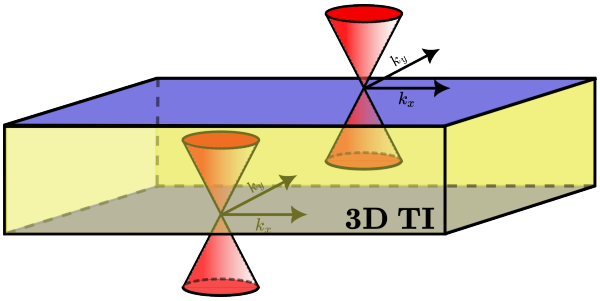

Figure 1.3: Schematic representation of a three-dimensional topological insulator. Each of the two surfaces (blue) exhibits a massless Dirac fermion.

When massless Dirac fermions are subjected to a magnetic field, they exhibit a unique type of energy spectrum. In classical mechanics, charged particles experience a Lorentz force that causes them to move in circular trajectories known as cyclotron orbits. While this intuition can hold down all the way to the quantum level, in quantum mechanics not all such orbits allowed. We call this discrete set of possible states in a magnetic field Landau levels[14]. These levels can be calculated by incorporating the magnetic field into the free particle Schrödinger equation, resulting in a quantized energy spectrum

$$E_n = \hbar\omega_c\left(n + \frac{1}{2}\right), \tag{1.7}$$

where $\omega_c = \frac{eB}{m}$ is the cyclotron frequency and n is a non-negative integer number. When we study massless fermions, the quantization condition changes into

$$E^{LL}_{\text{massless}} = \pm\sqrt{2n\hbar eBv_f^2}, \tag{1.8}$$

where v_f represents the Fermi velocity. The Landau levels are no longer equally spaced and allow for a new type of cyclotron orbits that are bound to exactly zero energy. These states are called zeroth Landau levels.

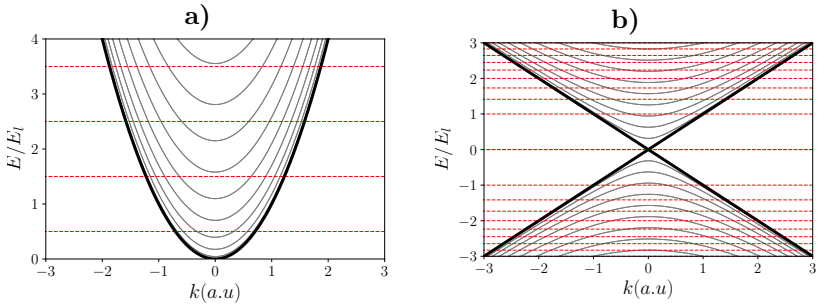

Figure 1.4: The dispersion Landau levels (red) compared to their initial dispersion (gray) for (a) massive and (b) massless particles compared to their initial dispersion.

1.3.2 Proximity effect and the Fu-Kane model

We can now explore what happens to the Dirac surface states under the effect of superconductivity. While there are a number of materials that can exhibit inherent superconducting properties at low temperatures, they usually belong to the class of trivial superconductors. Alternatively, it turns out that creating an interface between a superconducting and non-superconducting material can allow Cooper pair tunneling. This process is called the proximity effect and can induce an effective superconducting pairing. Such proximitized systems can be described by the Bogoliubov-De Gennes Hamiltonian

$$H_{BdG} = \begin{pmatrix} H(\vec{k}) & \Delta \\ \Delta^\dagger & -\mathcal{T}H(\vec{k})\mathcal{T} \end{pmatrix}, \tag{1.9}$$

where Δ denotes the superconducting pairing and $\mathcal{T}$ represents the time-reversal symmetry. This method allows us to describe the mean-field superconducting Hamiltonian by doubling the degrees of freedom. In particular, we artificially add hole-like degrees of freedom to the electronic Hamiltonian and couple them together with a superconducting pairing term Δ. Although superconducting states are not eigenstates of the electron number, this doubling allows us to introduce effective single-particle excitations called the Bogoliubov quasi-particles.

This thesis focuses on a special model of a topological superconductor called the Fu-Kane model. Such systems arise when we create an interface between a three-dimensional topological insulator and a conventional

superconductor. In this case, the Bogoliubov De-Gennes doubling creates an additional hole-like Dirac fermion on each surface. The pair of Dirac fermions can now couple through superconducting pairing without violating the time-reversal symmetry. Such coupling gives us the gapped dispersion of the Fu-Kane model.

One of the characteristic signatures of superconductors is a dissipationless current called the supercurrent. This current can be interpreted as the momentum of Cooper pairs. Such a current can split the electron-like and hole-like states in the Brillouin zone. In the particular case of the Fu-Kane heterostructure, this can separate the Dirac fermions in momentum space. We can see this in the Bogoliubov de-Gennes Hamiltonian

$$H_{BdG} = \begin{pmatrix} \left(\vec{k} - \vec{K}\right) \cdot \sigma & \Delta \\ \Delta^{\dagger} & -\left(\vec{k} + \vec{K}\right) \cdot \sigma \end{pmatrix}, \tag{1.10}$$

in which the supercurrent momentum $\vec{K}$ acts as a constant vector potential. It turns out that such separation slowly decouples the two Dirac fermions. It was shown a sufficient super-current can fully counteract the superconducting pairing creating a transition, restoring the gapless Dirac cone.

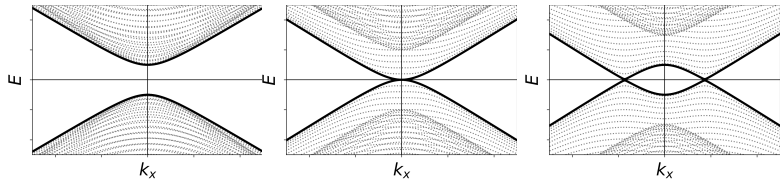

Figure 1.5: Dispersion of a Fu-Kane model with increasing suppercurrent strength (left to right), showing the transition from gapped massive Dirac fermions in a Fu-Kane model to the gapless Dirac states.

1.3.3 Majorana zero-modes in a topological superconductor

In our research, we investigated the effect of a magnetic field on the gap closing transition in the Fu-Kane model. As this is a superconducting system, the effects of a magnetic field can be very different. It is important to note that superconductors exhibit a specific property called the Meissner effect, whereby they expel the effects of magnetic fields. This phenomenon

implies that the effects of a magnetic field cannot penetrate a superconductor beyond a certain depth, known as the London penetration length. If we are interested in the effects of a magnetic field on bulk superconductors, we must focus on a specific group of superconductors called type-II superconductors. In this case, the magnetic field penetrates the superconductor in the form of localized defects called Abrikosov vortices[15]. These vortices are strong defects that carry exactly one quantum of magnetic flux, denoted as $\Phi_0 = h/(2e)$. The size of the defects is characterized by the superconducting coherence length, denoted as ξ, which is approximately equal to $1/\Delta_0$, while they carry the flux Φ_0 with circulating supercurrents that persist on a larger scale of the London penetration depth. At the level of wavefunctions, the Abrikosov vortices induce a winding of the superconducting phase parameter around their core by 2π.

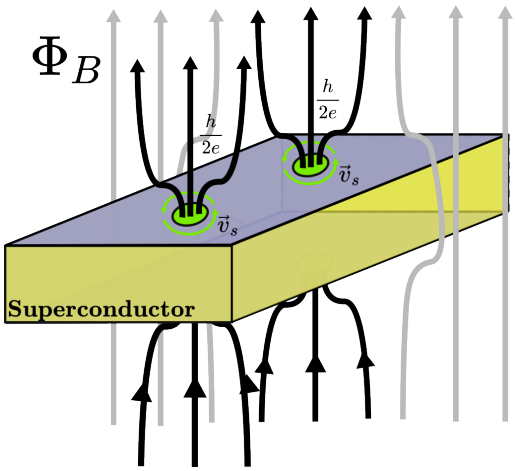

Figure 1.6: Schematic representation of a type-II superconductor in a magnetic field. The figure shows the magnetic flux-lines penetrating the superconducting sample through vortices. Each vortex carries a single ϕ_0 flux quanta and exhibits a circulating supercurrent flow $\vec{v_s}$.

In the gapped regime of the Fu-Kane model, vortex defects trap a special type of zero-energy excitation called Majorana zero-modes. These quasi-particles are unique in that they are their own antiparticles. Although they were originally predicted in particle physics to describe neutrinos, they can also appear in condensed matter systems as a consequence of particle-hole symmetry. This is an anti-unitary symmetry that anticommutes with the Hamiltonian, resulting in eigenstates of a Bogoliubov-

de Gennes Hamiltonian that are symmetric around zero energy. While eigenstates will generally occur in pairs around zero energy, a single zero-energy excitation cannot be gapped as long as the symmetry is preserved, resulting in isolated zero-energy excitations known as Majorana quasi-particles. These quasi-particles are eigenstates of the particle-hole symmetry and appear as equal superpositions of electrons and holes. To form a complete basis, such states always appear in pairs. Although this may appear to nullify their protection, they can be strongly spatially separated, allowing for protection against splitting from E=0 symmetrically in pairs. Majorana operators can be defined from their fermionic counterparts as

$$\gamma_1 = c^\dagger + c = \gamma_1^\dagger \tag{1.11}$$

$$\gamma_2 = i\big(c^\dagger - c\big) = \gamma_2^\dagger. \tag{1.12}$$

Because these operators are their own Hermitian conjugates, they exhibit a special commutation relation

$$\big\{\gamma_i, \gamma_j\big\} = 2\delta_{i,j}. \tag{1.13}$$

When these properties are combined, it turns out that Majorana zero-energy excitations exhibit non-abelian exchange statistics. This means that, unlike fermions and bosons, an exchange of Majoranas can fully change the quantum state. This unique property, combined with their strong protection, can be used in quantum computation to generate stable topological qubits that are protected from all local decoherence effects. Therefore, it is crucial to explore and discover viable new systems where Majorana zero-energy excitations can appear.

In the case of the Fu-Kane model, these Majorana states are bound to the vortex cores. Each vortex binds an exponentially localized zero-energy solution. These states appear in the presence of a magnetic field inside the superconducting gap, with a degeneracy equal to the number of flux quanta, $N = \phi/\phi_0$.

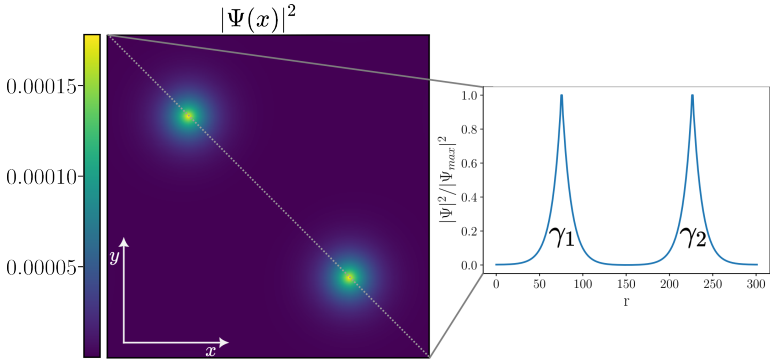

Figure 1.7: Probabilty density for zero mode solutions in a Fu-Kane superconductors. Majorana zero-modes are bound to the vortices of a superconductor with a characteristic exponential decay.

While these are the characteristic excitations in the gapped regime, it is known that the Fu-Kane superconductor becomes gapless in the presence of a strong supercurrent. We have shown that such gapless points exhibit a special type of zero-energy Landau levels. However, it turns out that this is not always the case for superconducting systems. Even though the magnetic field can become almost homogeneous in a sufficiently dense vortex lattice, the vortices still act as scatterers, which generally broadens the predicted zeroth Landau level[16].

In this thesis, we will present an example where a special symmetry prevents this broadening. We will demonstrate that the Fu-Kane model exhibits a unique type of symmetry called chiral symmetry. This is a local unitary symmetry that anti-commutes with the Hamiltonian. It allows us to write the Hamiltonian in a distinctive off-diagonal form described by

$$H_{chiral} = \begin{pmatrix} 0 & \Xi \\ \Xi^\dagger & 0 \end{pmatrix}. \tag{1.14}$$

This special form of the Hamiltonian enables us to invoke a theorem known as the Index theorem [17]. This theorem tells us that chiral Hamiltonians exhibit a unique integer value known as the index. This index can be calculated from the matrices Ξ and $\Xi^\dagger$ by looking at their corresponding kernels. While the dimensionality of the kernels (number of zero modes) of each of these two matrices can vary strongly, it turns out that their difference is very robust. This difference then defines the index, a topological invariant that cannot change under smooth local perturbation. Moreover, this invariant directly corresponds to the total number of

zero-modes in the system. Therefore, as long as the chiral symmetry is preserved, the number of zero-modes is conserved by a special topological protection. In this thesis, we will demonstrate that this invariant can not only predict the Majorana zero-modes, but remains unchanged when the Fu-Kane model transitions to the gapless regime. We will show how this leads to a new zero-energy superconducting state, where Majorana states delocalize into an extended Landau level state.

1.4 Weyl fermions in Kramers-Weyl semimetals

The concept of massless fermions can be extended to three dimensions, where they are known as Weyl fermions. These are found in specific systems called Weyl semimetals [13]. In a two-band theory of a three-dimensional crystal, there are no possible perturbations that could gap out a Weyl cone. This is due to the fact that a three-dimensional Dirac equation requires a four-dimensional representation to describe massive particles. Thus, the protection of the gapless Weyl points is much stronger, as they can only couple in pairs with opposite chirality. As we will later see, they are protected by a topological number directly related to the chirality of the Weyl fermion. This means that systems exhibiting Weyl fermions, unlike Dirac systems, do not require an additional symmetry; they only require pairs of Weyl fermions to be well separated. Such pairs are then reconnected on the surface of Weyl semimetals with a special class of two-dimensional surface states called Fermi arcs.

As Weyl cones in nature always appear in pairs of opposite chirality, Weyl semimetals need to either break time-reversal or inversion symmetry. This allows pairs of Weyl cones in momentum space to be split so that gapless points do not overlap. While there are many different realizations of Weyl fermions in nature, this thesis will focus on newly described systems that exhibit Kramers-Weyl fermions [9, 10]. These occur in crystals with preserved time-reversal symmetry but broken inversion symmetry. We have found new unique signatures of these novel states, specifically a new type of magneto-oscillations that arise as a consequence of characteristic long Fermi arcs as well as unique spectral statistics. To introduce this work, we will first discuss the general protection of three-dimensional gapless Weyl nodes. We will then focus on the specific form of Kramers-Weyl systems. Finally, we will explain the idea of Fermi arcs as one of the characteristic signatures of three-dimensional massless fermions and

explain their special extended form inside Kramers-Weyl semimetals.

1.4.1 Topological protection

As previously mentioned, the protection of Weyl points, unlike Dirac cones, does not require additional symmetries. This can be easily understood by examining the Weyl Hamiltonian, which shows that any perturbation that maintains translation symmetry will simply shift the Weyl cones in momentum space, while keeping a linear dispersion $E_{\text{Weyl}} \pm \sqrt{(k_x - V_x)^2 + (k_y - V_y)^2 + (k_y - V_y)^2}$ without introducing an effective mass.

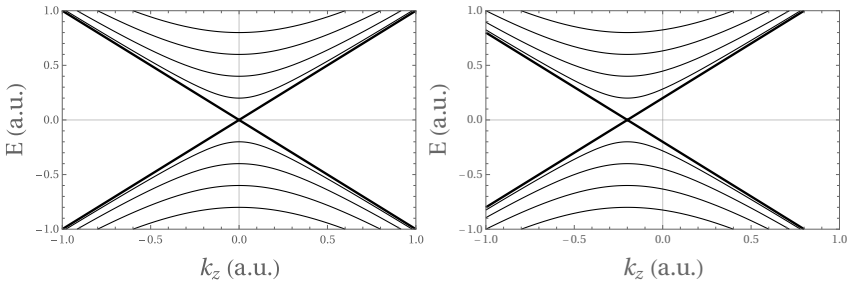

Figure 1.8: Gapless dispersion of a Weyl fermion. Left panel shows a Weyl cone in the center of the Brillouoin zone while the right panel shows a cone shifted in momentum space by a $V_z\sigma_z$ perturbation.

This type of protection is indeed very strong and quite peculiar, as we know that there must exist an atomic limit in which any system becomes strongly gapped. It is possible to achieve such a limit by coupling together two Weyl fermions, as is done in a four-dimensional representation of the Dirac equation. This process is naturally resolved in nature, as Weyl fermions can only appear in pairs. This allows the Weyl point to gap out, giving us a fully gapped dispersion $E_{\text{massive}} = \pm\sqrt{k_x^2 + k_y^2 + k_z^2 + M^2}$ that arises from the four-band Hamiltonian

$$H_{\text{Massive}} = \tau_z(\vec{\sigma} \cdot k) + \tau_x M. \tag{1.15}$$

Here the τ Pauli matrices describe the different Weyl cones, with τ_z representing two Weyl fermions with opposite chiralities, which plays an important role in the gap opening mechanism.

We can rewrite this argument independently of the exact form of the Hamiltonian by defining a topological invariant that characterizes each

Weyl cone and its protection. To do so, we must examine the behavior of the Berry curvature

$$\Omega_n(\vec{k}) = \nabla_k \times \mathcal{A}_n(R), \tag{1.16}$$

which takes the form of a quasi-magnetic field arising from the Berry connection $\mathcal{A}_n$. Such quasi-magnetic field defined by the Berry curvature acts as a magnetic monopole around the Weyl points, with the charge of such a monopole depending on the chirality of the Weyl fermion. As this charge takes discrete values, we know that no perturbation can remove it in a continuous manner. This charge therefore defines a topological invariant that tells us that such a Weyl point cannot be removed by itself. The only way to cancel out the monopole of the Berry curvature is to combine it with an additional monopole of opposite charge. This argument agrees with our previous prediction but is less reliant on the exact shape of the Hamiltonian. It tells us that as long as our system exhibits such unmerged monopoles in the Berry connection, the corresponding Weyl points will remain protected.

To summarize, the protection of Weyl points does not require additional symmetries, and it is a strong and peculiar type of protection. Coupling together two Weyl fermions can lead to a fully gapped dispersion, while the behavior of the Berry curvature provides a topological invariant that characterizes the protection of each Weyl cone.

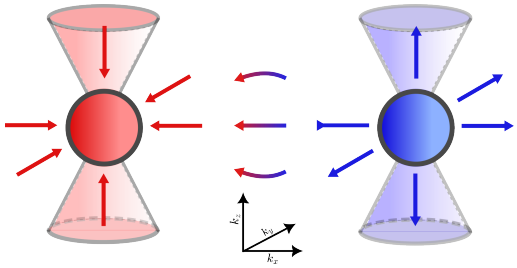

Figure 1.9: A schematic of the reconnection of two opposite monopoles of the Berry connection around the Weyl points.

1.4.2 Kramers-Weyl semimetal

We will now focus on a specific realization of Weyl fermions that occurs in Kramers-Weyl semimetals. Such systems are very exciting as they can not only provide a new approach to discovering materials described by

Weyl physics but also exhibit new characteristic behavior that is absent in conventional Weyl semimetals. This new type of massless excitation arises as a consequence of the preserved time-reversal symmetry. Specifically, we know that time-reversal symmetric systems exhibit a special degeneracy at time-reversal invariant points known as the Kramers degeneracy. This means that we can find gapless points at each corner of the three-dimensional Brillouin zone. As most crystals are invariant under inversion symmetry, which relates $E_\uparrow(k) = E_\uparrow(-k)$, the expansion around the gapless form must be even in momentum. This usually results in fully doubly degenerate bands around corners of the Brillouin zone with an effective quadratic dispersion.

However, we can focus on special chiral crystals that break inversion symmetry while still preserving time-reversal symmetry. These systems still have Kramers doublets at all the corners of the Brillouin zone but now exhibit a linear $\vec{\sigma} \cdot \delta\vec{k}$ expansion that describes Weyl excitations. This implies that all effective two-band models with time-reversal symmetry that break inversion symmetry will exhibit Weyl fermions at all the time-reversal invariant points in the Brillouin zone.

While this statement seems very robust, it turns out that while these Weyl cones are guaranteed to exist, they may not be easy to observe. This is because of two additional properties of such systems. First, the Weyl nodes can be strongly spread out in energies and can be quite far away from the Fermi surface. Second, our arguments arise from the expansion of the Hamiltonian for small momentum around the special degenerate points. While this expansion is generally linear, nothing forbids the appearance of higher-order quadratic terms. This means that the Kramers-Weyl cones are well-defined on the momentum scale where the linear term remains the governing part of the expansion. In reality, this tells us that we must consider systems that exhibit strong spin-orbit coupling in addition to the given prescription to study this novel realization of Weyl fermions.

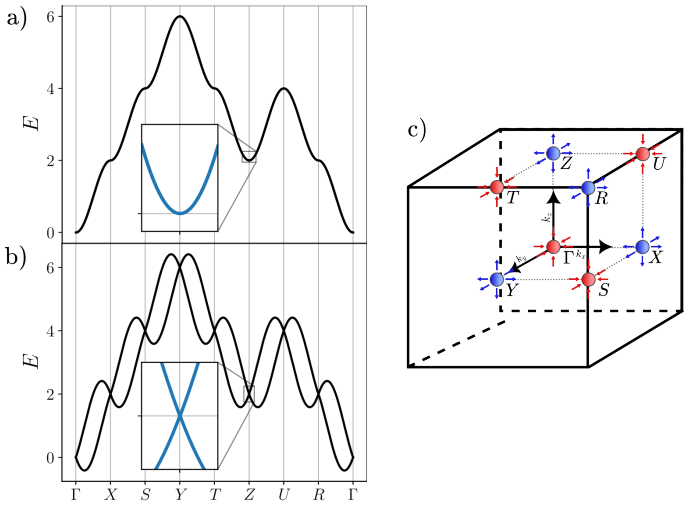

Figure 1.10: A schematic example of a generic two band dispersion for a) preserved, b) broken inversion symmetry. c) Schematic of the Kramers-Weyl Brillouin zone, identifying the time-reversal invariant momenta and their corresponding Weyl cones.

Now that we have understood the mechanisms responsible for the emergence of Kramers-Weyl fermions, it is important to explore the distinguishing features of these systems as compared to conventional Weyl semimetals. As we have already mentioned, Weyl fermions can only appear in pairs of opposite chiralities in nature. In contrast to a conventional three-dimensional semimetal, which typically hosts one or two pairs of massless fermions, Kramers-Weyl semimetals always exhibit four pairs of Weyl fermions with alternating chiralities. Since all these cones are precisely located at time-reversal-invariant momenta, they are guaranteed to have a strong separation in momentum space. This not only confers them with unusual robustness but is also quite distinct, as it is generally difficult to strongly pair Weyl fermions in the Brillouin zone. The large separation of the cones is responsible for unique signatures, as it forces the Fermi arc surface states that connect the Weyl cones to span over the entire Brillouin zone.

1.4.3 Fermi arcs

We have demonstrated that each Weyl point carries a topological invariant representing the monopole charge of the Berry connection. In the

bulk, such a monopole can only annihilate with its opposite partner, providing a mechanism for continuously transforming the Weyl system into the atomic limit where the system is fully gapped. Alternatively, we can consider a sharp interface where we truncate the Weyl semimetal, creating a contact with the surrounding vacuum. As the Weyl system exhibits pairs of monopoles and the vacuum does not, these monopoles have to recombine on the interface during the transition from the Weyl semimetal to the vacuum. As a consequence, Weyl semimetals have to exhibit special types of surface states that connect Weyl cones of opposite chiralities and annihilate the monopole charges. These states are called Fermi arcs, as they form special two-dimensional Fermi surfaces. They are massless states with linear dispersion and are one of the characteristic signatures of Weyl semimetals.

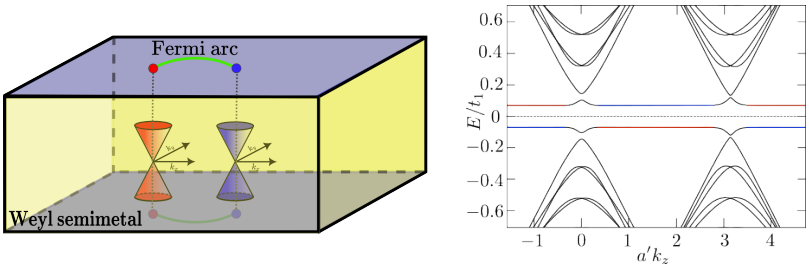

Figure 1.11: Left panel: Schematic representation of the Fermi arc surface states reconnecting the Bulk Weyl cones. Right panel: A dispersion of a Kramers-Weyl semimetal in a slab geometry showing the characteristic long Fermi arcs spanning the whole Brillouin zone.

The signature of such surface states is directly related to the separation of Weyl cones, as the Fermi arcs exhibit a higher density of states when they span over a larger region of the Brillouin zone. For this reason, Kramers-Weyl semimetals can be a good platform for their study, as they guarantee a large momentum space separation. Additionally, it turns out that unlike in conventional Weyl semimetals, Fermi arcs in Kramers-Weyl materials create a new type of periodic Fermi surface structure, where open orbits can form, giving us a completely unique magnetic behavior.

1.5 Outline of this thesis

This thesis covers a diverse range of massless electronic systems, which can be broadly divided into three parts. The first part focuses on the study of Dirac fermions and their properties. The second part focuses on the three-dimensional crystals and the signatures of Weyl physics. Finally, the thesis concludes with the last two chapters that concentrate on superconducting Majorana excitations.

1.5.1 Part 1

This part delves into the localization properties of two-dimensional massless fermions. We explore various condensed matter systems that exhibit Dirac fermions and propose a novel technique for the study of Anderson localization.

Chapter 2: Localization landscape of Dirac fermions

Non-interacting systems under the presence of random disorder exhibit universal behavior called Anderson localization. This means that electronic wave functions become strongly localized, impairing transport properties in the system. While it is generally impossible to find all the localization centers without diagonalization, it turns out that it is possible to define a special function that is strongly sensitive to the localized behavior of low-energy states. This function is called the Localization landscape and it can be efficiently calculated for a Schrödinger equation of spinless electrons with a positive definite Hamiltonian. In this chapter, we have extended this idea to spinful systems described by the Dirac equation. In particular, we have concentrated on systems with strong spin-orbit coupling to be able to study localization in graphene, topological insulators, and superconductors. We use the Ostrowski comparison matrix to treat systems that are not positive definite and extend the localization landscape bound to their comparison matrix. This defines a new landscape that can be efficiently calculated by solving the $Hu(r) = 1$ differential equation, where H is the comparison matrix of a chosen Dirac Hamiltonian. As the comparison matrix is only sensitive to real Hamiltonian elements, we were able to define a new equivalence class for Anderson localization. This allows us to find equivalent Hermitian and non-Hermitian Hamiltonians that share the same localization properties.

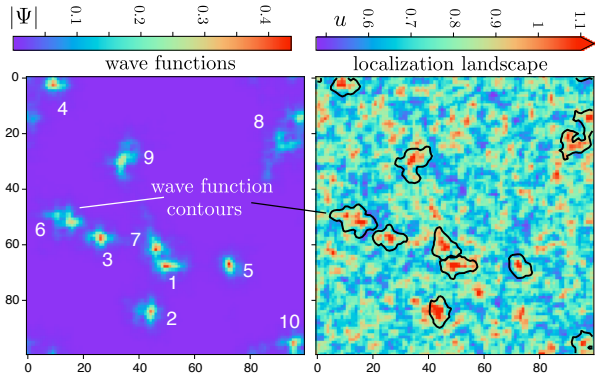

Figure 1.12: Localization centers of a disordered Dirac system (left) compared to the comparison matrix Localization landscape predictions (right).

1.5.2 Part 2

The second part of this thesis focuses on the behavior of Weyl fermions in the presence of a magnetic field. Specifically, we will investigate two systems and examine new signatures of Kramers-Weyl fermions as previously described in the introduction. Additionally, we will explore the transport properties of Landau levels in Weyl superconductors.

Chapter 3: Magnetic breakdown spectrum of a Kramers-Weyl semimetal

Kramers-Weyl semimetals exhibit four widely separated pairs of Weyl fermions at time reversal invariant points. In a finite sample, they give rise to unique extended Fermi arcs that span through the whole Brillouin zone. This chapter will focus on the consequences of the interplay between such characteristic surface states and a magnetic field. In particular, we show that the long Fermi arcs can form open orbits in momentum space. In the presence of a magnetic field, these can interact and couple with the Landau levels formed from the closed orbits in the bulk, thereby broadening their dispersion relation. We can use an effective model to describe this behavior in terms of a one-dimensional superlattice induced by the magnetic breakdown. Such a model can predict resonant behaviors when the dynamics are dominated by either open or closed orbits. This resonant behavior can be observed in terms of $1/B$ periodic magneto-oscillations, which are fully unique to the Kramers-Weyl semimetals compared to the

usual Shubnikov-de Haas oscillations that arise from Landau level quantization.

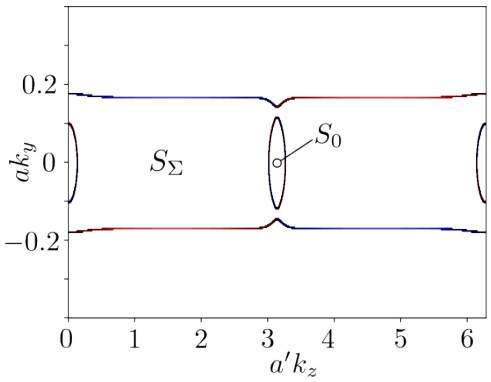

Figure 1.13: Figure shows the characteristic Fermi surface of a Kramers-Weyl semimetal in a slab geometry, focused around a single Weyl cone. Such Fermi-surface exhibits both open and closed orbits in the momentum space.

Chapter 4: Supercell symmetry modified spectral statistics of Kramers-Weyl fermions

In this chapter, we continue to investigate the unique signatures of Kramers-Weyl fermions. Using the predictions of random matrix theory, we explore the spectral statistics of a Kramers-Weyl toy model given by $H = v\sum_\alpha \sigma_\alpha \sin k_\alpha + t\sigma_0 \sum_\alpha \cos k_\alpha$ in a chaotic quantum dot. We find a hidden symmetry in the limit of small t that mimics a spinless time-reversal symmetry. This is a consequence of a special supercell symmetry that holds exactly when $t = 0$. We examine the consequences of this additional symmetry by observing the level spacing distribution $P(\alpha s^\beta)$, where we find that the calculated spectral statistic for small t truly obeys the orthogonal $\beta = 1$ ensemble instead of the expected symplectic ensemble $\beta = 4$. While this hidden symmetry is quickly broken for any realistic values of t, we find that signatures of the transition can still be detected. In particular, we show that this transition happens much slower when we observe the transition from weak localization to weak antilocalization, providing us with a new probe to detect the Kramers-Weyl fermions.

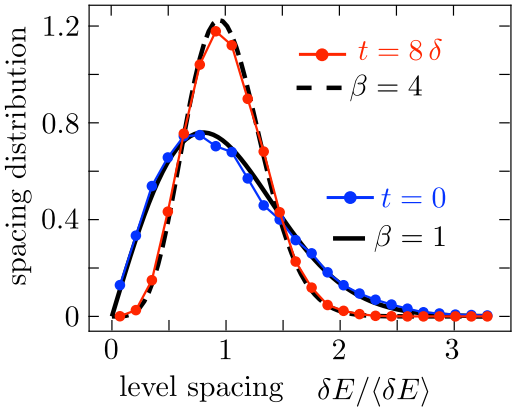

Figure 1.14: Two limiting examples of the spacing distribution comparing the orthogonal behaviour at small t and symplectic behaviour for large t.

Chapter 5: Chiral charge transfer along magnetic field lines in a Weyl superconductor

A heterostructure consisting of alternating layers of a Weyl semimetal and a conventional superconductor creates a gapless superconducting system called a Weyl superconductor. It was recently shown that, unlike conventional gapless superconductors, these systems exhibit a protected zeroth Landau level in the presence of a magnetic field. This chapter follows up on the recent study of the conductance signatures of these superconducting Landau levels. We have found a new conductance signature where the conductance depends on the direction of the magnetic field compared to the chiralities of the Weyl cones. This gives us a novel signature that can directly probe the chiralities of superconducting Weyl fermions.

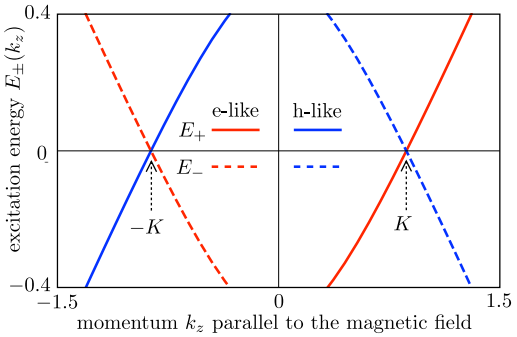

Figure 1.15: Dispersion relation of the superconducting zeroth landau level in the direction parallel to the magnetic field.

1.5.3 Part 3

The final section of this thesis will concentrate on the emergence of Majorana fermions. Specifically, we will investigate the Fu-Kane heterostructure introduced earlier and study how the interaction between the magnetic field and supercurrent can displace Majorana fermions away from the vortex cores.

Chapter 6: Deconfinement of Majorana vortex modes produces a superconducting Landau level

Shared contribution with Michał Pacholski; I was responsible for the numerical simulations.

A Fu-Kane superconductor in the presence of a magnetic field binds Majorana zero-energy excitations to the cores of the magnetic vortices. These are strongly localized excitations, topologically protected because of their exponentially small overlaps. This chapter examines how such protected states behave in the presence of a strong supercurrent, which can be interpreted as a spatially oscillating pair potential $\Delta(\vec{r}) = \Delta_0 e^{2i\vec{K}\cdot\vec{r}}$ describing Cooper pairs with momentum $\vec{K}$. We show that such a supercurrent induces a delocalization transition when $K > \Delta_0/\hbar v$, extending the Majorana modes into a new fully delocalized state with a unique oscillatory pattern. Using the index theorem, we prove that at $\mu = 0$, these states surprisingly remain gapless despite their strong overlaps. In fact, they form a dispersionless superconducting Landau level that is fully protected from broadening by the inter-vortex scattering. We then find an exact analytical solution for this new superconducting state and calculate the characteristic wave vector as $\sqrt{K^2 - (\Delta_0/\hbar v)}$. We show that this striped

pattern can be used to measure the chirality of Majorana fermions and propose a local density of states measurement to investigate such states experimentally.

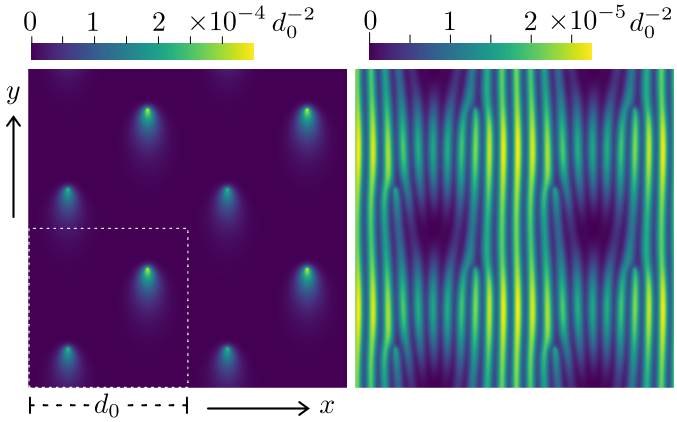

Figure 1.16: Two plots show the transition in the local density of states, induced by the supercurrent, for a Fu-Kane model with a vortex lattice. The first image is showing the strongly localized Majorana solutions at small supercurrent momentum $\Delta_0 < K/\hbar v$ while the second image shows the new strongly oscillating extended states at $\Delta_0 > K/\hbar v$.

Chapter 7: Magnus effect on a Majorana zero-mode

In the last chapter, we will continue studying the newly discovered delocalization transition of Majorana zero-modes in the Fu-Kane model. Specifically, we will examine how the dynamics of delocalization can manifest as a manifestation of the Magnus effect. In our system, this effect arises from the coupling between the superflow and the velocity profile inside the vortex core. This effect induces an acceleration on the Majorana vortex modes perpendicular to the superflow. As the supercurrent velocity profile around the vortex core depends on the chirality, if the supercurrent is strong enough, it can induce a full escape where the localized Majorana modes propagate away from the vortex core in the form of a localized wave-packet with a constant velocity. This effect is extremely surprising as, unlike the magnetic field, it is actually inducing a force on chargeless Majorana states that do not feel the conventional Lorentz force. We demonstrate this effect numerically by simulating a quench of the superflow. Furthermore, we find a semiclassical description for the

wave packet that allows us to predict and match the final velocity of this escape regime.

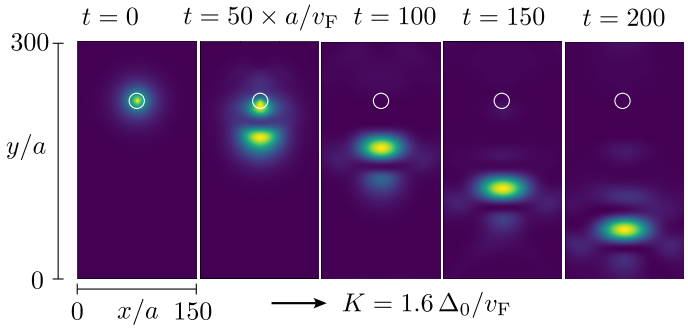

Figure 1.17: The escape behaviour of the chragless Majorana zero-modes under the influence of a strong superflow. The figure shows the propagation of the wave packet in a straight trajectory defined by chirality in the plane perpendicular to the superflow.

2 Localization landscape for Dirac fermions

2.1 Introduction

The localization landscape is a new tool in the study of Anderson localization, pioneered in 2012 by Filoche and Mayboroda [18], which has since stimulated much computational and conceptual progress [19–28]. The "landscape" of a Hamiltonian H is a function $u(\boldsymbol{r})$ that provides an upper bound for eigenstates ψ at energy $E > 0$:

$$|\psi(\boldsymbol{r})|/|\psi|_{\max} \leq E\, u(\boldsymbol{r}), \quad |\psi|_{\max} = \max_{\boldsymbol{r}} |\psi(\boldsymbol{r})|. \tag{2.1}$$

This inequality implies that a localized state is confined to spatial regions where $u \gtrsim 1/E$. Extensive numerical simulations [26] confirm the expectation that higher and higher peaks in u identify the location of states at smaller and smaller E.

Such a predictive power would be unremarkable for particles confined to potential wells (deeper and deeper wells trap particles at lower and lower energies). But Anderson localization happens because of wave interference in a random "white noise" potential, and inspection of the potential landscape $V(\boldsymbol{r})$ gives no information on the localization landscape $u(\boldsymbol{r})$.

Filoche and Mayboroda considered the localization of scalar waves, or equivalently of spinless electrons, governed by the Schrödinger Hamiltonian $H = -\nabla^2 + V$. They used the maximum principle for elliptic partial differential equations to derive [18] that the inequality (2.1) holds if $V > 0$ and u is the solution of

$$[-\nabla^2 + V(\boldsymbol{r})]u(\boldsymbol{r}) = 1. \tag{2.2}$$

Our objective here is to generalize this to spinful electrons, to include the effects of spin-orbit coupling and study localization of Dirac fermions.

2.2 Construction of the landscape function

Our key innovation is to use Ostrowski's comparison matrix [29–32] as a general framework for the construction of a localization landscape on a lattice. By definition, the comparison matrix $\overline{H}$ of a complex matrix H has elements

$$\overline{H}_{nm} = \begin{cases} |H_{nn}| & \text{if } n = m, \\ -|H_{nm}| & \text{if } n \neq m. \end{cases} \tag{2.3}$$

In our context the index $n = 1, 2, \ldots$ labels both the discrete space coordinates as well as any internal (spinor) degrees of freedom. The comparison theorem [29] states that if the comparison matrix is positive-definite, then [1]

$$|H^{-1}| \leq \overline{H}^{-1}, \tag{2.4}$$

where both the absolute value and the inequality is taken elementwise.

We apply Eq. (2.4) to an eigenstate Ψ of H at energy E,

$$\begin{aligned} |E^{-1}\Psi_n| = |(H^{-1}\Psi)_n| &\leq \textstyle\sum_m \left|\left(H^{-1}\right)_{nm}\right| |\Psi_m| \\ &\leq |\Psi|_{\max} \textstyle\sum_m \left(\overline{H}^{-1}\right)_{nm}, \end{aligned} \tag{2.5}$$

with $|\Psi|_{\max} = \max_n |\Psi_n|$. We now define a landscape function u with elements u_n in terms of a set of linear equations with coefficients given by the comparison matrix:

$$\overline{H}\, u = 1 \Leftrightarrow \textstyle\sum_m \overline{H}_{nm} u_m = 1, \quad n = 1, 2, \ldots N, \tag{2.6}$$

which implies that

$$\textstyle\sum_m \left(\overline{H}^{-1}\right)_{nm} = u_n. \tag{2.7}$$

Substitution into Eq. (2.5) thus gives the desired inequality

$$|\Psi_n| / |\Psi|_{\max} \leq |E|\, u_n. \tag{2.8}$$

As a sanity check, we make contact with the original landscape function [18] for the Schrödinger Hamiltonian $H_{\rm S} = p^2/2m + V$, with $V > 0$. The Laplacian is discretized in terms of nearest-neighbor hoppings on a lattice. For each dimension

$$\begin{aligned} &p^2 \mapsto (\hbar/a)^2 (2 - 2\cos ka) \Rightarrow \\ &(H_{\rm S})_{nm} = t_0 (2\delta_{nm} - \delta_{n-1,m} - \delta_{n+1,m}) + V_n \delta_{nm}, \end{aligned} \tag{2.9}$$

[1] The comparison inequality (2.4) does not require a Hermitian H. More generally, if H is not Hermitian and $\overline{H}$ has complex eigenvalues the requirement of positive-definiteness is that all eigenvalues have positive real part. We give a general proof of Eq. (2.4) in the Appendix (supplemental material).

with lattice constant a and hopping matrix element $t_0 = \hbar^2/2ma^2$. The comparison matrix $\overline{H}_{\rm S}$ is equal to $H_{\rm S}$ and is positive-definite, so that Eq. (2.6) is a discretized version of the original landscape equation $H_{\rm S}u = 1$ [18, 33].

2.3 Rashba Hamiltonian

Our first novel application is to introduce spin-orbit coupling of the Rashba form,

$$H_{\rm R} = H_{\rm S} + \tfrac{1}{2}\{\lambda, p_x\}\sigma_y - \tfrac{1}{2}\{\lambda, p_y\}\sigma_x. \tag{2.10}$$

(The anticommutator $\{\cdots\}$ enforces Hermiticity when λ is spatially dependent.) The comparison matrix is now no longer equal to the Hamiltonian, in 1D one has

$$(\overline{H}_{\rm R})_{ij} = (H_{\rm S})_{ij} - \frac{\hbar}{4a}|\lambda_i + \lambda_j|(\delta_{i-1,j} + \delta_{i+1,j})\sigma_x. \tag{2.11}$$

The i, j, indices label the spatial positions, the spinor indices are implicit in the Pauli matrix.

As a test, to isolate the effect of spin-orbit coupling, we place all the disorder in the Rashba strength λ_n, which fluctuates randomly from site to site, uniformly in the interval $(\bar{\lambda} - \delta\lambda, \bar{\lambda} + \delta\lambda)$. The electrostatic potential is a constant offset V_0, chosen sufficiently large that $\overline{H}_{\rm R}$ is positive-definite [2]. Examples in 1D and in 2D are shown in Figs. 2.1 and 2.2. The highest peaks in the landscape function match well with the lowest eigenfunctions.

2.4 Dirac Hamiltonian

We next turn to Dirac fermions, first in 1D. The Dirac Hamiltonian

$$H_{\rm D} = v_{\rm F} p_x \sigma_x + V\sigma_0 + \mu\sigma_z \tag{2.12}$$

contains a scalar potential V proportional to the 2×2 unit matrix σ_0 and a staggered potential μ proportional to σ_z, acting on the two-component

[2] A *sufficient* condition for a positive-definite comparison matrix $\overline{H}$ is that H is diagonally dominant, meaning $|H_{nn}| > \sum_{m \neq n} |H_{nm}|$ for each n. For the Rashba Hamiltonian (2.10) this implies $V_0 > d \times (\bar{\lambda} + \delta\lambda)$ on a d-dimensional square lattice. A *necessary and sufficient* condition [32] for positive-definiteness of $\overline{H}$ is that there exists a vector v with positive elements such that $(\overline{H}\, v)_n > 0$ for all n. For the sufficient condition of diagonal dominance one would take $v = (1, 1, \ldots 1, 1)$.

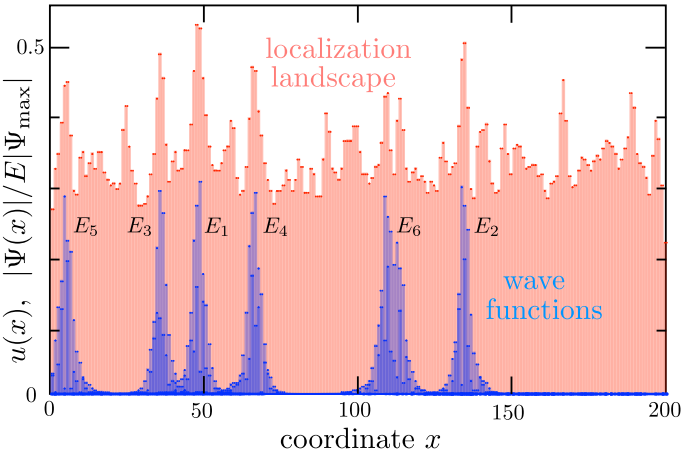

Figure 2.1: Landscape function $u(x)$ (red) and normalized wave function profile $|\Psi(x)|/E|\Psi_{\max}|$ (blue) for the 6 lowest (twofold degenerate) eigenstates of the disordered 1D Rashba Hamiltonian (2.11) (parameters $V_0 = 4t_0$, $\bar{\lambda} = 0$, $\delta\lambda = 3\hbar/a$, hard-wall boundary conditions). The 1D array has $n = 1, 2, \ldots 200$ sites, in the plot $x = n$ shows the first spinor component and $x = n + 1/2$ shows the second spinor component. The wave functions are labeled by the corresponding energy levels $\{E_1, \ldots E_6\} = \{3.273, 3.3371, 3.414, 3.446, 3.508, 3.516\}$ (in units of t_0).

wave function $\Psi = (\psi_A, \psi_B)$. This would apply to a graphene nanoribbon on a substrate such as hexagonal boron nitride, which differentiates between the two carbon atoms in the unit cell without causing intervalley scattering [34].

The symmetric discretization $\partial_x \Psi \mapsto (1/2a)[\Psi(x+a) - \Psi(x-a)]$ suffers from fermion doubling [35, 36] — it corresponds to a sin ka dispersion with a second species of massless Dirac fermions at the edge of the Brillouin zone ($k = \pi/a$). To avoid this, and restrict ourselves to a single valley, we use a staggered-fermion discretization *a la* Susskind [37, 38]:

$$p_x \sigma_x \Psi \mapsto (-i\hbar/a) \begin{pmatrix} \psi_B(x) - \psi_B(x-a) \\ \psi_A(x+a) - \psi_A(x) \end{pmatrix}. \tag{2.13}$$

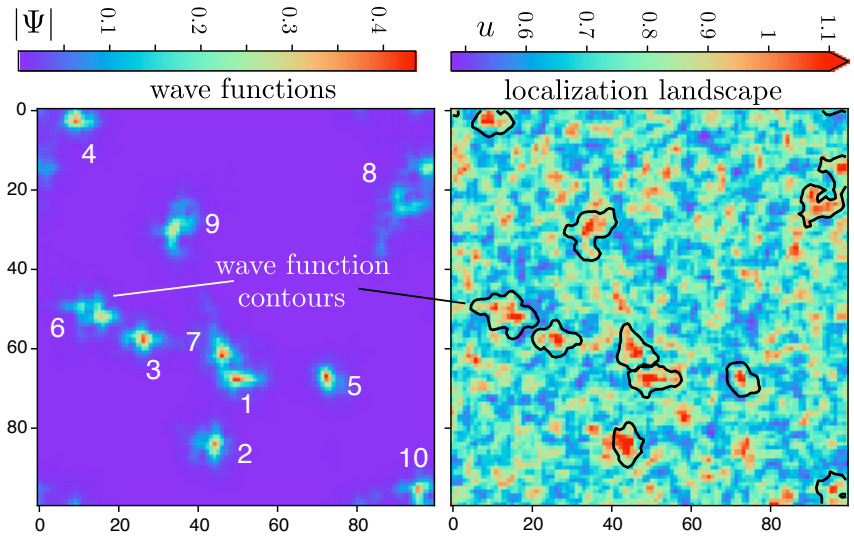

Figure 2.2: Same comparison as in Fig. 2.1, but now for the 2D Rashba Hamiltonian, discretized on a 100×100 square lattice (parameters $V_0 = 6t_0$, $\bar{\lambda} = 2\delta\lambda = 2\hbar/a$, periodic boundary conditions).The left panel shows the spinor norm $|\Psi_n(\boldsymbol{r})|$ for the 10 lowest (twofold degenerate) eigenstates of $H_{\rm R}$. The right panel shows the localization landscape. The black contours (computed at 10% of the peak height of $|\Psi|$) identify the location of the 10 eigenstates — to show the close correspondence with the local maxima of $u(\boldsymbol{r})$.

The corresponding dispersion [3]

$$E(k) = \pm t_1\sqrt{2 - 2\cos ka}, \quad t_1 = \hbar v_{\rm F}/a, \tag{2.14}$$

has massless fermions only at the center of the Brillouin zone ($k = 0$).

The comparison matrix takes the form

$$(\overline{H}_{\rm D})_{ij} = \begin{pmatrix} |V_i + \mu_i|\delta_{ij} & -t_1(\delta_{ij} + \delta_{i+1,j}) \\ -t_1(\delta_{ij} + \delta_{i-1,j}) & |V_i - \mu_i|\delta_{ij} \end{pmatrix}. \tag{2.15}$$

We take random $V(x) \in (\bar{V} - \delta V, \bar{V} + \delta V)$ and $\mu(x) \in (\bar{\mu} - \delta\mu, \bar{\mu} + \delta\mu)$, chosen independently and uniformly at each lattice site. The condition $|V_i \pm \mu_i| > 2t_1$ ensures a positive-definite $\overline{H}_{\rm D}$. As shown in Figs. 2.3 and

[3] The staggered discretization (2.13) corresponds to the tight-binding Hamiltonian $H = (\hbar v_{\rm F}/a)\sigma_x \sin ka + (\hbar v_{\rm F}/a)(1 - \cos ka)\sigma_y + V\sigma_0 + \mu\sigma_z$, which gives the dispersion relation (2.14) when $V = \mu = 0$.

2.4, the landscape function computed from $\overline{H}_{\rm D} u = 1$ again accurately identifies the locations of the low-lying eigenfunctions (near the band edge in Fig. 2.3 and near the gap in Fig. 2.4).

For the 2D Dirac equation we consider a chiral p-wave superconductor, with Bogoliubov-De Gennes Hamiltonian [39]

$$H_{\rm BdG} = \Delta(p_x\sigma_x + p_y\sigma_y) + (V + p^2/2m)\sigma_z. \tag{2.16}$$

The Pauli matrices act on the electron-hole degree of freedom of a Bogoliubov quasiparticle, and the Hamiltonian is constrained by particle-hole symmetry: $\sigma_x H_{\rm BdG}\sigma_x = -H^*_{\rm BdG}$. (A scalar offset $\propto \sigma_0$ is thus forbidden.) The pair potential Δ opens a gap in the spectrum in the entire Brillouin zone, provided that the electrostatic potential V is nonzero. The gap-closing transition at $V = 0$ is a topological phase transition [40].

We take a uniform real Δ (no vortices) and a disordered $V(x, y)$, fluctuating randomly from site to site in the interval $(\bar{V}+\delta V, \bar{V}-\delta V)$. Positive V ensures we do not cross the gap-closing transition, so we will not be introducing Majorana zero-modes [41] (the levels are Andreev bound states). Unlike in the case of graphene we can use the symmetric discretization $p \mapsto \sin ka$ — there is no need for a staggered discretization because the kinetic energy $p^2 \mapsto 2 - 2\cos ka$ prevents fermion doubling at $k = \pi/a$. Results are shown in Fig. 2.5.

Equivalence classes — In the final part of this chapter we move beyond applications to address a conceptual implication of the theory. Two complex matrices A, B are called equimodular if $|A_{nm}| = |B_{nm}|$. By the construction (2.3), they have the same comparison matrix, $\overline{A} = \overline{B}$, and therefore the same landscape function $u_A = u_B$, uniquely determined by the same equation $\overline{A}\, u_A = 1 = \overline{B}\, u_B$. We thus obtain an equivalence class for Anderson localization: *Equimodular Hamiltonians have localized states at the same position, identified by peaks in the landscape function.*

We have checked this for the 2D Rashba Hamiltonian (2.10): Randomly varying the sign of the coefficient $\lambda(\boldsymbol{r})$ from site to site shifts the energy levels around, but the states remain localized at the same positions. More generally, one could try to vary the coefficients over the complex plane, preserving the norm. This would produce a non-Hermitian eigenvalue problem, and one might wonder whether the whole approach breaks down. It does not, as we will now demonstrate.

The non-Hermitian Anderson Hamiltonian [42, 43]

$$\mathcal{H} = -\nabla^2 + V_1(\boldsymbol{r}) + iV_2(\boldsymbol{r}) \tag{2.17}$$

has been studied in the context of a random laser [44]: a disordered optical lattice with randomly varying absorption and amplication rates, described

by a complex dielectric function $V_1 + iV_2$. On a d-dimensional square lattice (lattice constant a), the discretization of $-\nabla^2 \mapsto a^{-2}\sum_{i=1}^{d}(2 - 2\cos k_i a)$ produces a spectral band width of $W_0 = 4d/a^2$.

The Hermitian Hamiltonian

$$H_{\text{eff}} = -\nabla^2 + V_{\text{eff}}, \quad V_{\text{eff}} = |\tfrac{1}{2}W_0 + V_1 + iV_2| - \tfrac{1}{2}W_0, \tag{2.18}$$

is positive-definite if $V_{\text{eff}}(\boldsymbol{r}) > 0$ for all $\boldsymbol{r}$. The transformation from complex V to real V_{eff} does not change the landscape function, because $\overline{\mathcal{H}} = \overline{H}_{\text{eff}} = H_{\text{eff}}$. The localization landscapes are therefore the same and we would expect the eigenstates [4] of $\mathcal{H}$ and H_{eff} to appear at the same positions, provided that $V_{\text{eff}} > 0$. This works out, as shown in Fig. 2.6.

2.5 Conclusion and outlook

We have shown that the comparison matrix $\overline{H}$ provides a route to the landscape function for Hamiltonians that are not of the Schrödinger form $H = -\nabla^2 + V$. We have explored Hamiltonians for massive or massless Dirac fermions, with or without superconducting pairing. The broad generality of the approach is highlighted by the application to the non-Hermitian Anderson Hamiltonian.

The localization landscape can be used as a tool to quickly and efficiently find low-lying localized states in a disordered medium, since the landscape function $u(\boldsymbol{r})$ is obtained from a single differential equation $\overline{H}\,u = 1$. These applications have been demonstrated for the Schrödinger Hamiltonian [22–25], and we anticipate similar applications for the Dirac Hamiltonian in the context of graphene or of topological insulators.

The comparison matrix offers a conceptual insight as well: Since equimodular Hamiltonians have the same comparison matrix, they form an equivalence class that localizes at the same spatial positions. This notion is distinct from the familiar notion of "universality classes" of Anderson localization [45], which refers to ensemble-averaged properties. The equivalence class, instead, refers to sample-specific properties.

As an outlook to future research, it would be interesting to extend the approach from wave functions to energy levels. This has been recently demonstrated for the Schrödinger Hamiltonian [26], where the peak height of the localization function predicts the energy of the localized state. The

[4] Because $\mathcal{H}^\dagger = \mathcal{H}^*$, the left and right eigenvectors are each others complex conjugate and we do not need to distinguish between these when plotting the absolute value in Fig. 2.6b.

correlation between peak heights and energy levels evident in Fig. 2.1 suggests that the comparison matrix has this predictive power as well. Another direction to investigate is to see if the comparison matrix would make it possible to incorporate spin degrees of freedom in the *many-body* localization landscape introduced recently [46].

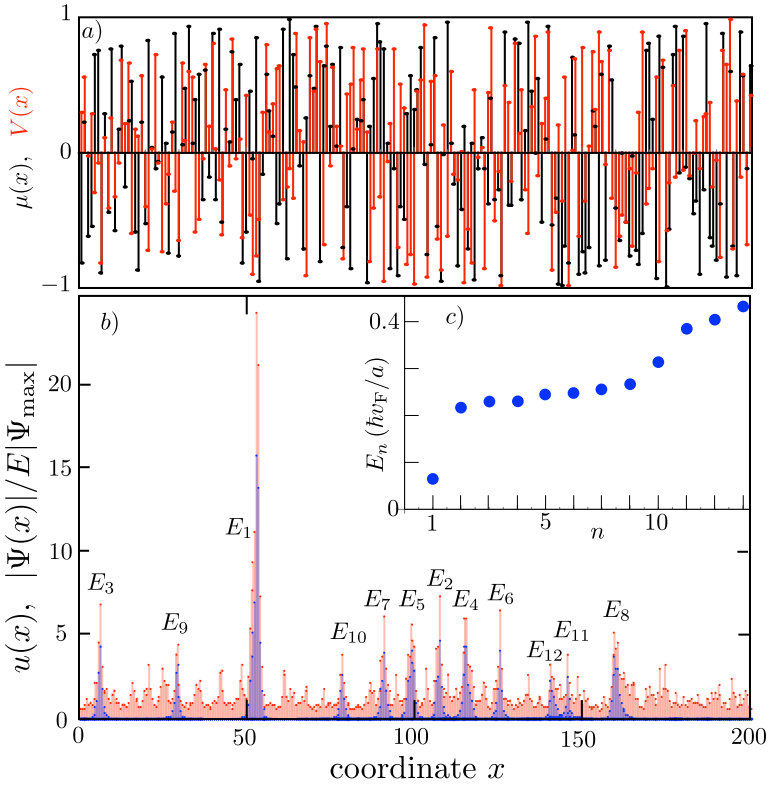

Figure 2.3: Panel *(*a): Random scalar potential $V(x)$ (red) and staggered potential $\mu(x)$ (black) for the 1D Dirac Hamiltonian (2.12) (parameters $\bar{V} = 3t_1$, $\bar{\mu} = 0$, $\delta V = \delta\mu = t_1$, hard-wall boundary conditions). Panel *b)*: Corresponding localization landscape (red) and eigenfunctions of the 12 lowest energy levels (blue), at energies E_n near the band edge plotted in the inset (panel *c*). The peaks in the localization landscape are not correlated in any obvious way with the random potentials, but they accurately predict the location of the low-lying modes.

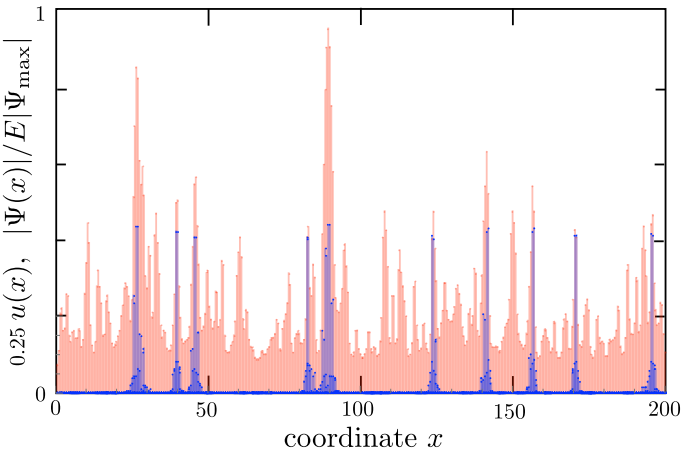

Figure 2.4: Same as Fig. 2.3b, but now for a gapped system ($\bar{V} = \delta V = 0$, $\bar{\mu} = 3.5\,t_1$, $\delta\mu = 1.5\,t_1$). The eigenfunctions of the 20 levels closest to the gap are shown (blue, $2.3\,t_1 < |E_n| < 2.5\,t_1$). There are only 10 distinct peaks, because of an approximate $\pm E$ symmetry. The landscape function (red, rescaled by a factor 1/4) accurately identifies the location of the states near the gap.

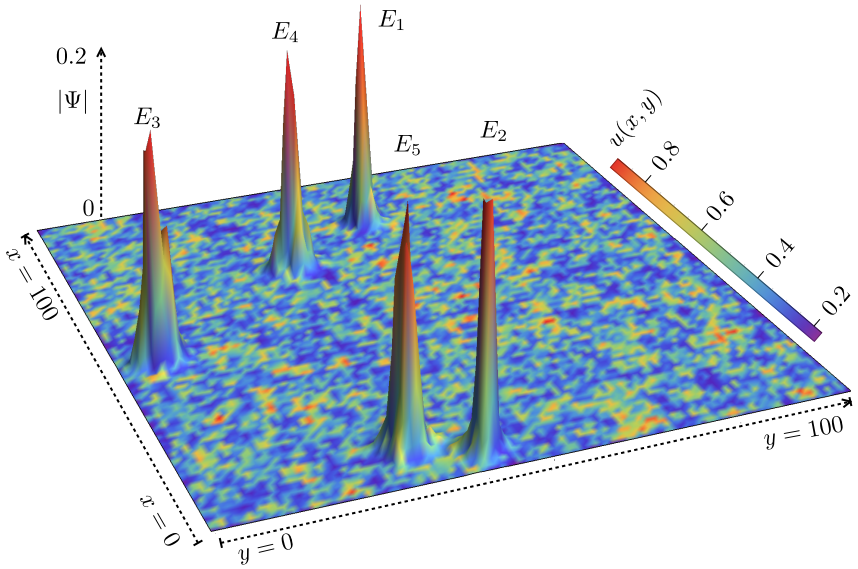

Figure 2.5: Comparison of the landscape function (2D color scale plot) with wave function amplitudes (3D profile) of the chiral p-wave superconductor with Hamiltonian (2.16) (parameters $\Delta = 1$, $\bar{V} = 6$, $\delta V = 4$, in units of $t_0 = \hbar^2/2ma^2$). The wave functions show the five Andreev levels with smallest $E_n > 0$ ($E_1, E_2, \ldots E_5 = 3.763, 3.799, 3.875, 3.882, 3.893$). (The charge-conjugate states at $-E_n$ have the same spinor amplitude $|\Psi|$.) The colors of the wave function profile correspond to the landscape function, so a red wave function peak indicates that $u(x, y)$ peaks at the same position.

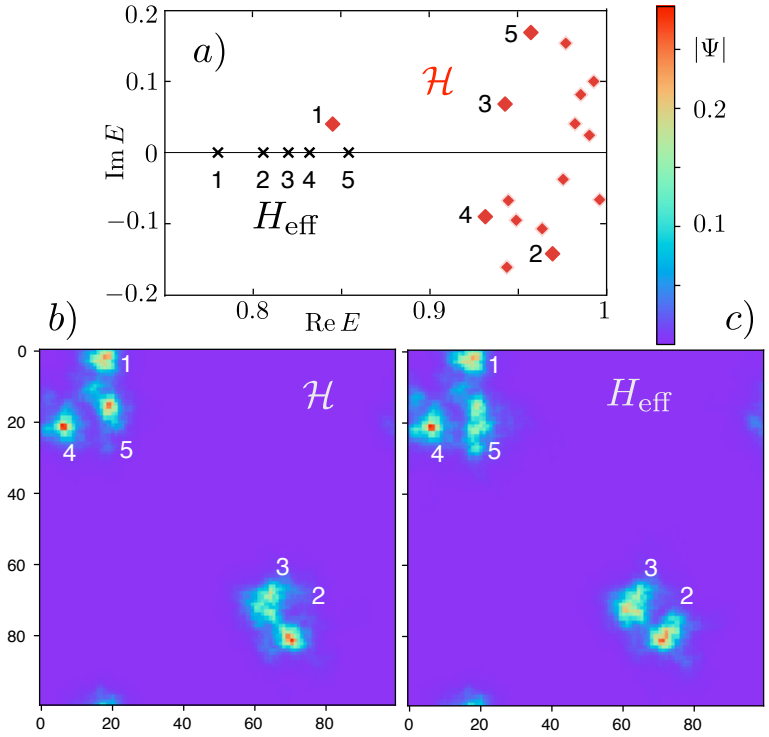

Figure 2.6: Energy levels (panel a) and localized eigenstates (panels b,c) of the non-Hermitian Hamiltonian $\mathcal{H}$ from Eq. (2.17) and its Hermitian counterpart $H_{\rm eff}$ from Eq. (2.18). The calculations are performed on a 2D square lattice (lattice constant $a \equiv 1$, band width $W_0 = 8$, periodic boundary conditions) for potentials V_1 and V_2 randomly and independently chosen at each site, uniformly in the interval $(-1, 1)$. A constant offset $V_0 = 1$ was added to V_1 in order to ensure a positive $V_{\rm eff}$. The mapping from $\mathcal{H}$ to $H_{\rm eff}$ preserves the spatial location of the localized states, while the ordering of the energy levels $|E_n|$ in absolute value is changed. Panels b,c show the eigenstates of the five lowest energy levels of $H_{\rm eff}$ and the corresponding eigenstates of $\mathcal{H}$. The locations are preserved but E_2 of $\mathcal{H}$ is pushed to higher absolute values.

Appendices

2.A Derivation of the comparison inequality

The comparison inequality (2.4) is derived by Ostrowski [29]. Here we give an alternative derivation, to make the chapter self-contained.

In the most general case the matrix H is a complex matrix, not necessarily Hermitian. We will initially assume that the diagonal elements H_{nn} are real ≥ 0 and relax that assumption at the end.

Decompose $H = \lambda \mathbb{1} - L$, with $\lambda > \max_n H_{nn}$, so that the diagonal elements of L are all positive. If we denote by $|L|$ the elementwise absolute value of the matrix L, one has

$$\lambda \mathbb{1} - |L| = \overline{H}, \tag{2.19}$$

under the assumption that $H_{nn} \geq 0$.

Consider the Euclidean propagator e^{-Ht} for $t \geq 0$, and start from the inequality

$$\left|\sum_m \left(e^{-Ht}\right)_{nm} \Psi_m\right| \leq \sum_m \left|\left(e^{-Ht}\right)_{nm}\right| |\Psi_m|. \tag{2.20}$$

We expand e^{-Ht} in a Taylor series,

$$\begin{aligned} \left|\left(e^{-Ht}\right)_{nm}\right| &= e^{-\lambda t} \left| \sum_{p=0}^{\infty} \frac{t^p}{p!} (L^p)_{nm} \right| \\ &\leq e^{-\lambda t} \sum_{p=0}^{\infty} \frac{t^p}{p!} (|L|^p)_{nm} = e^{-\lambda t} \left(e^{|L|t}\right)_{nm} = \left(e^{-\overline{H}\, t}\right)_{nm}. \end{aligned} \tag{2.21}$$

Substitution into Eq. (2.20) gives

$$\left|\sum_m \left(e^{-Ht}\right)_{nm} \Psi_m\right| \leq \sum_m \left(e^{-\overline{H}\, t}\right)_{nm} |\Psi_m|. \tag{2.22}$$

This may also be written more compactly as

$$|e^{-Ht}| \leq e^{-\overline{H} t}, \tag{2.23}$$

with the understanding that the absolute value and inequality is taken elementwise.

If we now assume that all eigenvalues of $\overline{H}$ have a positive real part, then we may integrate both e^{-Ht} and $e^{-\overline{H}\,t}$ over t from 0 to ∞. On the one hand we have,

$$\int_0^\infty e^{-Ht}\,dt = H^{-1}, \tag{2.24}$$

and on the other hand, in view of Eq. (2.23), we have

$$\left|\int_0^\infty e^{-Ht}\,dt\right| \le \int_0^\infty |e^{-Ht}|\,dt \le \int_0^\infty e^{-\overline{H}\,t}\,dt = \overline{H}^{\,-1}. \tag{2.25}$$

We thus arrive at the desired comparison inequality (2.4),

$$|H^{-1}| \le \overline{H}^{\,-1}. \tag{2.26}$$

The assumption that H_{nn} is real ≥ 0 can be removed my multiplying H with the diagonal matrix

$$D_{nm} = \delta_{nm}\, e^{-i \arg H_{nn}} \tag{2.27}$$

(setting $D_{nn} = 1$ if $H_{nn} = 0$). This matrix multiplication changes neither the comparison matrix, $\overline{DH} = \overline{H}$, nor the absolute value of the inverse, $|(DH)^{-1}| = |H^{-1}D^{-1}| = |H^{-1}|$, hence Eq. (2.26) still holds. Only the assumption of positive-definite $\overline{H}$ remains.

3 Magnetic breakdown spectrum of a Kramers-Weyl semimetal

3.1 Introduction

Kramers-Weyl fermions are massless low-energy excitations that may appear in the Brillouin zone near time-reversally invariant momenta (TRIM). Their gapless nature is protected by Kramers degeneracy, which enforces a band crossing at the TRIM. Crystals that support Kramers-Weyl fermions have strong spin-orbit coupling and belong to one of the chiral point groups, without reflection or mirror symmetry, to allow for a linear rather than quadratic band splitting away from the TRIM. The materials are called topological chiral crystals or Kramers-Weyl semimetals — to be distinguished from generic Weyl semimetals where Kramers degeneracy plays no role. Several candidates were predicted theoretically [9, 10] and some have been realized in the laboratory [48–52].

These recent developments have motivated the search for observables that would distinguish Kramers-Weyl fermions from generic Weyl fermions [53–55]. Here we report on the fundamentally different Landau level spectrum when the semimetal is confined to a thin slab in a perpendicular magnetic field.

Generically, Landau levels are dispersionless: The energy does not depend on the momentum in the plane perpendicular to the magnetic field B. In contrast, we have found that the Landau levels of a Kramers-Weyl semimetal are broadened into a Landau band. The band width oscillates periodically in $1/B$, producing an oscillatory contribution to the magnetoconductance.

The phenomenology is similar to that encountered in a semiconductor 2D electron gas in a superlattice potential [56–60]. In that system the dispersion is due to the drift velocity of cyclotron orbits in perpendicular electric and magnetic fields. Here the surface Fermi arcs provide for open orbits, connected to closed orbits by magnetic breakdown at Weyl points

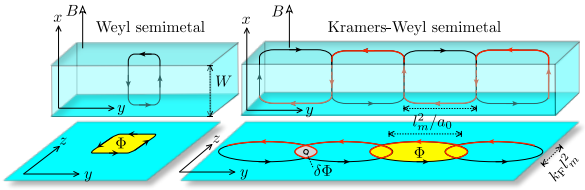

Figure 3.1: Electron orbits in a thin slab geometry perpendicular to a magnetic field (along the x-axis), for a generic Weyl semimetal [61, 62] (at the left) and for a Kramers-Weyl semimetal (at the right). In each case we show separately a front view (in the x–y plane, to show how the orbits switch between top and bottom surfaces of the slab) and a top view (in the y–z plane, to indicate the magnetic flux enclosed by the orbits). The Kramers-Weyl semimetal combines open orbits (red arrows) with closed orbits enclosing either a large flux Φ or a small flux $\delta\Phi$. Open and closed orbits are coupled by a periodic chain of magnetic breakdown events, spaced by l_m^2/a_0 (with a_0 the lattice constant and $l_m = \sqrt{\hbar/eB}$ the magnetic length). The open orbits broaden the Landau levels into a band, the band width varies from minimal to maximal when $\delta\Phi$ is incremented by h/e. Because $\delta\Phi \propto Bl_m^4 \propto 1/B$, the band width oscillations are periodic in $1/B$.

(see Fig. 3.1).

No open orbits appear in a generic Weyl semimetal [61, 62], because the Weyl points are closely separated inside the first Brillouin zone, so the Fermi arcs are short and do not cross the Brillouin zone boundaries (a prerequisite for open orbits). The Landau band dispersion therefore directly ties into a defining property [9] of a Kramers-Weyl semimetal: surface Fermi arcs that span the entire Brillouin zone because they connect TRIM at zone boundaries.

In the next two sections 3.2 and 3.3 we first compute the spectrum of a Kramers-Weyl semimetal slab in zero magnetic field, to obtain the equi-energy contours that govern the orbits when we apply a perpendicular field. The resonant tunneling between open and closed orbits via magnetic breakdown is studied in Sec. 3.4. With these preparations we are ready to calculate the dispersive Landau bands and the magnetoconductance oscillations in Secs. 3.5 and 3.6. The analytical calculations are then compared with the numerical solution of a tight-binding model in Secs. 3.7 and 6.A. We conclude in Sec. 7.6.

3.2 Boundary condition for Kramers-Weyl fermions

The first step in our analysis is to characterize the surface Fermi arcs in a Kramers-Weyl semimetal, which requires a determination of the boundary condition for Kramers-Weyl fermions. This is more strongly constrained by time-reversal symmetry than the familiar boundary condition on the Dirac equation [63]. In that case the confinement by a Dirac mass $V_\mu = \mu(\hat{\boldsymbol{n}}_\parallel \cdot \boldsymbol{\sigma})$ generates a boundary condition

$$\Psi = (\hat{\boldsymbol{n}}_\perp \times \hat{\boldsymbol{n}}_\parallel) \cdot \boldsymbol{\sigma} \Psi. \tag{3.1}$$

The unit vectors $\hat{\boldsymbol{n}}_\parallel$ and $\hat{\boldsymbol{n}}_\perp$ are parallel and perpendicular to the boundary, respectively.

Although $\boldsymbol{\sigma} \mapsto -\boldsymbol{\sigma}$ upon time reversal, the Dirac mass may still preserve time-reversal symmetry if the Weyl fermions are not at a time-reversally invariant momentum (TRIM). For example, in graphene a Dirac mass $+\mu$ at the K-point in the Brillouin zone and a Dirac mass $-\mu$ at the K$'$-point preserves time-reversal symmetry. In contrast, for Kramers-Weyl fermions at a TRIM the V_μ term in the Hamiltonian is incompatible with time-reversal symmetry. To preserve time-reversal symmetry the boundary condition must couple two Weyl cones, it cannot be of the single-cone form (3.1).

In App. 3.A we demonstrate that, indeed, pairs of Weyl cones at a TRIM are coupled at the boundary of a Kramers-Weyl semimetal. Relying on that result, we derive in this section the time-reversal invariant boundary condition for Kramers-Weyl fermions.

We consider a Kramers-Weyl semimetal in a slab geometry, confined to the y–z plane by boundaries at $x = 0$ and $x = W$. In a minimal description we account for the coupling of two Weyl cones at the boundary. To first order in momentum $\boldsymbol{k}$, measured from a Weyl point, the Hamiltonian of the uncoupled Weyl cones is

$$\begin{aligned} H_\pm(\boldsymbol{k}) &= \begin{pmatrix} H_0(\boldsymbol{k}) + \varepsilon & 0 \\ 0 & \pm H_0(\boldsymbol{k}) - \varepsilon \end{pmatrix}, \\ H_0(\boldsymbol{k}) &= \textstyle\sum_{\alpha=x,y,z} v_\alpha k_\alpha \sigma_\alpha. \end{aligned} \tag{3.2}$$

The $\pm$ sign indicates whether the two Weyl cones have the same chirality $(+)$ or the opposite chirality $(-)$. The two Weyl points need not be at the same energy, we allow for an offset ε. We also allow for anisotropy in the velocity components v_α.

The σ_α's are Pauli matrices acting on the spin degree of freedom. We will also use τ_α Pauli matrices that act on the Weyl cone index, with σ_0 and τ_0 the corresponding 2×2 unit matrix. We can then write

$$H_+ = H_0\tau_0 + \varepsilon\tau_z, \quad H_- = H_0\tau_z + \varepsilon\tau_z. \tag{3.3}$$

The current operator in the x-direction is $j_+ = v_x\sigma_x\tau_0$ for H_+ and $j_- = v_x\sigma_x\tau_z$ for H_-. The time-reversal operation $\mathcal{T}$ does not couple Weyl cones at a TRIM, it only inverts the spin and momentum:

$$\mathcal{T}H_\pm(\boldsymbol{k})\mathcal{T}^{-1} = \sigma_y H_\pm^*(-\boldsymbol{k})\sigma_y = H_\pm(\boldsymbol{k}). \tag{3.4}$$

An energy-independent boundary condition on the wave function Ψ has the general form [63]

$$\Psi = M_\pm \cdot \Psi, \quad M_\pm = M_\pm^\dagger, \quad M_\pm^2 = 1, \tag{3.5}$$

in terms of a Hermitian and unitary matrix $M_\pm$. The matrix $M_\pm$ anticommutes with the current operator $j_\pm$ perpendicular to the surface, to ensure current conservation. Time-reversal symmetry further requires that

$$\sigma_y M_\pm^* \sigma_y = M_\pm. \tag{3.6}$$

These restrictions reduce $M_\pm$ to the single-parameter form

$$\begin{aligned} M_+(\phi) &= \tau_y\sigma_y \cos\phi + \tau_y\sigma_z \sin\phi, \\ M_-(\phi) &= \tau_x\sigma_0 \cos\phi + \tau_y\sigma_x \sin\phi. \end{aligned} \tag{3.7}$$

The angle ϕ has a simple physical interpretation in the case H_+, M_+ case of two coupled Weyl cones of the same chirality: It determines the direction of propagation of the helical surface states (the Fermi arcs). We will take $\phi = 0$ at $x = 0$ and $\phi = \pi$ at $x = W$. This produces a surface state that is an eigenstate of $\tau_y\sigma_y$ with eigenvalue $+1$ on one surface and eigenvalue -1 on the opposite surface, so a circulating surface state in the $\pm y$-direction. (Alternatively, if we would take $\phi = \pm\pi/2$ the state would circulate in the $\pm z$-direction.)

Notice that these are helical rather than chiral surface states: The eigenstates Ψ of $\tau_y\sigma_y$ with eigenvalue $+1$ contain both right-movers ($\sigma_y\Psi = +\Psi$) and left-movers ($\sigma_y\Psi = -\Psi$). This is the key distinction with surface states in a magnetic Weyl semimetal, which circulate unidirectionally around the slab [13, 64–66].

In the case H_-, M_- that the coupled Weyl cones have the opposite chirality there are no helical surface states and the physical interpretation of the angle ϕ in Eq. (3.7) is less obvious. Since our interest here is in the Fermi arcs, we will not consider that case further in what follows.

3.3 Fermi surface of Kramers-Weyl fermions in a slab

3.3.1 Dispersion relation

We calculate the energy spectrum of H_+ with boundary condition M_+ from Eq. (3.7) along the lines of Ref. 67. Integration in the x-direction of the wave equation $H_\pm\Psi = E\Psi$ with $k_x = -i\hbar\partial/\partial x$ relates the wave amplitudes at the top and bottom surface via $\Psi(W) = e^{i\Xi}\Psi(0)$, with

$$\Xi = \frac{W}{\hbar v_x}\sigma_x(E - v_y k_y\sigma_y - v_z k_z\sigma_z - \varepsilon\tau_z). \tag{3.8}$$

As discussed in Sec. 3.2 we impose the boundary condition $\Psi = M_+(0)\Psi$ on the $x = 0$ surface and $\Psi = M_+(\pi)\Psi$ on the $x = W$ surface.

The round-trip evolution

$$\Psi(0) = M_+(0)e^{-i\Xi}M_+(\pi)e^{i\Xi}\Psi(0) \tag{3.9}$$

then gives the determinantal equation

$$\mathrm{Det}\left(1 + \tau_y\sigma_y e^{-i\Xi}\tau_y\sigma_y e^{i\Xi}\right) = 0, \tag{3.10}$$

which evaluates to

$$\begin{aligned}[E^2 - \varepsilon^2 + (v_z k_z)^2 - (v_y k_y)^2]\frac{\sin w_- \sin w_+}{q_- q_+} \\ = 1 + \cos w_- \cos w_+,\end{aligned} \tag{3.11}$$

with the definitions

$$q_\pm^2 = (E \pm \varepsilon)^2 - (v_y k_y)^2 - (v_z k_z)^2, \;\; w_\pm = \frac{W}{\hbar v_x}q_\pm. \tag{3.12}$$

In the zero-offset limit $\varepsilon = 0$ Eq. (3.11) reduces to the more compact expression

$$\left(\frac{v_z k_z}{q}\tan\frac{Wq}{\hbar v_x}\right)^2 = 1, \;\; q^2 = E^2 - (v_y k_y)^2 - (v_z k_z)^2, \tag{3.13}$$

which is a squared Weiss equation [67, 68].

The dispersion relation $E(k_y, k_z)$ which follows from Eq. (3.11) is plotted in Fig. 3.2. The surface states (indicated in red) are nearly flat as function of k_z, so they propagate mainly in the $\pm y$ direction. In the limit $\varepsilon \to 0$ the bands cross at $k_z = 0$, this crossing is removed by the energy offset.

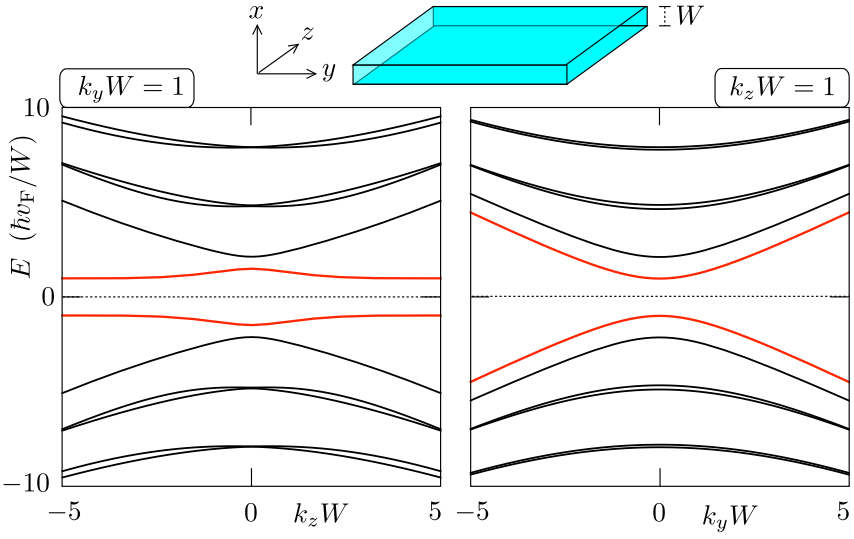

Figure 3.2: Dispersion relation $E(k_y, k_z)$ as a function of k_z for fixed $k_y = 1/W$ (left panel) and as a function of k_y for fixed $k_z = 1/W$ (right panel), calculated from Eq. (3.11) for $v_x = v_y = v_z \equiv v_\mathrm{F}$ and $\varepsilon = \hbar v_\mathrm{F}/W$. The surface states are indicated in red. The avoided crossings at $k_z = 0$ become real crossings for $\varepsilon = 0$.

3.3.2 Fermi surface topology

The equi-energy contours $E(k_y, k_z) = E_\mathrm{F}$ are plotted in Fig. 3.3 for several values of W. The topology of the Fermi surface changes at a critical width

$$W_\mathrm{c} = \frac{\pi}{2}\frac{\hbar v_x}{E_\mathrm{F}} + \mathcal{O}(\varepsilon). \tag{3.14}$$

At $W = W_\mathrm{c}$ the surface bands from upper and lower surface touch at the Weyl point $k_y = k_z = 0$, and for larger widths the upper and lower surface bands decouple from a bulk band, in the interior of the slab.

For $\varepsilon = 0$ the surface and bulk bands intersect at $k_z = 0$ when $W > W_\mathrm{c}$. The gap δk_y which opens up for nonzero ε is

$$\delta k_y = \frac{4}{\pi v_y}|\varepsilon| + \mathcal{O}(\varepsilon^2), \quad W > W_c. \tag{3.15}$$

For later use we also record the area S_0 enclosed by the bulk band,

$$S_0 = \tfrac{4}{3}\pi\sqrt{2}(W/W_c - 1)^{3/2}k_\mathrm{F}^2 + \mathcal{O}(W/W_c - 1)^2 + \mathcal{O}(\varepsilon), \tag{3.16}$$

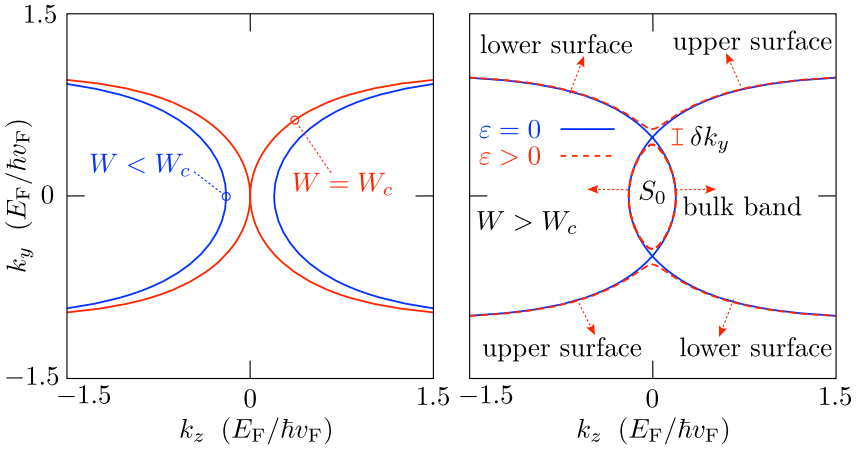

Figure 3.3: Solid curves: equi-energy contours $E(k_y, k_z) = E_F$ for $\varepsilon = 0$ at three values of W (in units of $\hbar v_F/E_F$ with $E_F > 0$): $W = \pi/2 = W_c$ (red curve in left panel), $W = 1.4 < W_c$ (blue curve in left panel), and $W = 1.8 > W_c$ (blue curve in right panel). The calculations are based on Eq. (3.11) with $v_x = v_y = v_z \equiv v_F$. The red dashed curve in the right panel shows the effect of a nonzero $\varepsilon = 0.1\,E_F$: The intersecting contours break up into two open and one closed contour, separated at $k_z = 0$ by a gap δk_y. The dotted arrows, perpendicular to the equi-energy contours, point into the direction of motion in real space. The assignment of the bands to the upper and lower surface is in accord with the time-reversal symmetry requirement that a band stays on the same surface when $(k_y, k_z) \mapsto -(k_y, k_z)$.

where we have defined the 2D Fermi wave vector of the Weyl fermions via

$$E_F = \hbar k_F \sqrt{v_y v_z}. \tag{3.17}$$

3.4 Resonant tunneling between open and closed orbits in a magnetic field

Upon application of a magnetic field B in the x-direction, perpendicular to the slab, the Lorentz force causes a wave packet to drift along an equi-energy contour. Because $\dot{\boldsymbol{k}} = e\dot{\boldsymbol{r}} \times \boldsymbol{B}$ the orbit in real space is obtained from the orbit in momentum space by rotation over $\pi/2$ and rescaling by a factor $\hbar/eB = l_m^2$ (magnetic length squared).

Inspection of Fig. 3.3 shows that for $W > W_c$ closed orbits in the interior of the slab coexist with open orbits on the surface. The open

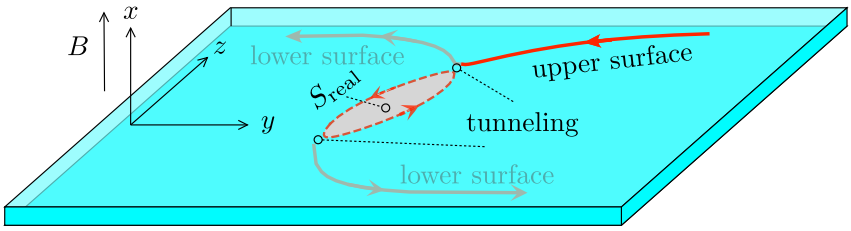

Figure 3.4: Electron orbits in a magnetic field perpendicular to the slab, following from the Fermi surface in Fig. 3.3 ($W > W_c$, $\varepsilon > 0$). The tunneling events (magnetic breakdown) between open and closed orbits are indicated. These happen with probability T_{MB} given by Eq. (3.18). Backscattering of the open orbit via the closed orbit happens with probability $\mathcal{R}$ given by Eq. (3.19). The area $S_{\text{real}} \propto 1/B^2$ of the closed orbit in real space determines the $1/B$ periodicity of the magnetoconductance oscillations via the resonance condition $BS_{\text{real}} = nh/e$.

and closed orbits are coupled via tunneling through a momentum gap δk_y (magnetic breakdown [69, 70]), with tunnel probability $T_{\text{MB}} = 1 - R_{\text{MB}}$ given by the Landau-Zener formula

$$T_{\text{MB}} = \exp(-B_c/B), \quad B_c \simeq (\hbar/e)\delta k_y^2 \simeq (\hbar\varepsilon/ev_{\text{F}})^2. \tag{3.18}$$

In the expression for the breakdown field B_{c} a numerical prefactor of order unity is omitted [70, 71].

The real-space orbits are illustrated in Fig. 3.4: An electron in a Fermi arc on the top surface switches to the bottom surface when the Fermi arc terminates at a Weyl point [61]. The direction of propagation (helicity) of the surface electron may change as a consequence of the magnetic breakdown, which couples a right-moving electron on the top surface to a left-moving electron on the bottom surface. This backscattering process occurs with reflection probability

$$\mathcal{R} = \left| \frac{T_{\text{MB}}}{1 - R_{\text{MB}} e^{i\phi}} \right|^2 = \frac{T_{\text{MB}}^2}{T_{\text{MB}}^2 + 4R_{\text{MB}} \sin^2(\phi/2)}. \tag{3.19}$$

The phase shift ϕ accumulated in one round trip along the closed orbit is determined by the enclosed area S_0 in momentum space,

$$\phi = S_0 l_m^2 + 2\pi\nu, \tag{3.20}$$

with $\nu \in [0, 1)$ a magnetic-field independent offset.

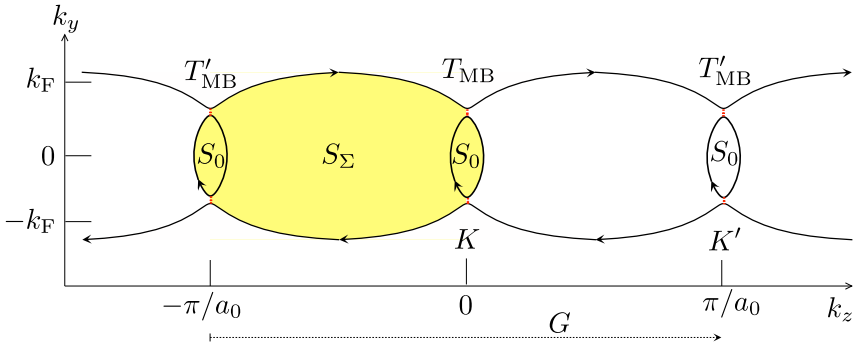

Figure 3.5: Equi-energy contours in the k_y–k_z plane, showing open orbits coupled to closed orbits via magnetic breakdown (red dotted lines). The closed contours encircle Weyl points at $\boldsymbol{K} = (0, 0)$ and $\boldsymbol{K}' = (0, \pi/a_0)$ — periodically translated by the reciprocal lattice vector $\boldsymbol{G} = (0, 2\pi/a_0)$. Arrows indicate the spectral flow in a perpendicular magnetic field. The large area S_Σ (yellow) determines the spacing of the Landau bands, while the small area S_0 and the magnetic breakdown probabilities $T_\mathrm{MB}, T'_\mathrm{MB}$ determine the band width.

Resonant tunneling through the closed orbit, resulting in $\mathcal{R} = 1$, happens when ϕ is an integer multiple of 2π. We thus see that the resonances are periodic in $1/B$, with period

$$\Delta(1/B) = \frac{2\pi e}{\hbar S_0} \approx \frac{e}{h}(W/W_c - 1)^{-3/2} k_\mathrm{F}^{-2}. \tag{3.21}$$

(We have substituted the small-ε expression (3.16) for S_0.)

The Shubnikov-de Haas (SdH) oscillations due to Landau level quantisation are also periodic in $1/B$. Their period is determined by the area $S_\Sigma \approx 2\pi k_\mathrm{F}/a_0$ in Fig. 3.5, hence

$$\Delta(1/B)_\mathrm{SdH} = \frac{2\pi e}{\hbar S_\Sigma} \approx \frac{e a_0}{\hbar k_\mathrm{F}}. \tag{3.22}$$

Comparison with Eq. (3.21) shows that the period of the SdH oscillations is smaller than that of the magnetic breakdown oscillations by a factor $k_\mathrm{F} a_0 (W/W_c - 1)^{3/2}$, which is typically $\ll 1$.

3.5 Dispersive Landau bands

Let us now discuss how magnetic breakdown converts the flat dispersionless Landau levels into dispersive bands. The mechanism crucially relies

on the fact that the surface Fermi arcs in a Kramers-Weyl semimetal connect Weyl points at time-reversally invariant momenta. Consider two TRIM $\boldsymbol{K}$ and $\boldsymbol{K}'$ in the (k_y, k_z) plane of the surface Brillouin zone. We choose $\boldsymbol{K} = (0, 0)$ at the zone center and $\boldsymbol{K}' = (0, \pi/a_0)$ at the zone boundary, with $\boldsymbol{G} = (0, 2\pi/a_0)$ a reciprocal lattice vector.

In the periodic zone scheme, the Weyl points can be repeated along the k_z-axis with period $2\pi/a_0$, to form an infinite one-dimensional chain (see Fig. 3.5). The perpendicular magnetic field B induces a flow along this chain in momentum space, which in real space is oriented along the y-axis with period

$$\mathcal{L} = (2\pi/a_0) l_m^2 = 2\pi v_y/\omega_c, \quad \omega_c = eBv_y a_0/\hbar. \tag{3.23}$$

In the weak-field regime $l_m \gg a_0$ the period $\mathcal{L}$ of the magnetic-field induced superlattice is large compared to the period a_0 of the atomic lattice. We seek the band structure of the superlattice.

We distinguish the Weyl points at $\boldsymbol{K}$ and $\boldsymbol{K}'$ by their different magnetic breakdown probabilities, denoted respectively by $T_{\rm MB} = 1 - R_{\rm MB}$ and $T'_{\rm MB} = 1 - R'_{\rm MB}$. We focus on the case that $T_{\rm MB}$ and $T'_{\rm MB}$ are close to unity and the areas S_0 and S'_0 of the closed orbits are the same — this is the small-ε regime in Eqs. (3.16) and (3.18). (The more general case is treated in App. 3.C.)

The phase shift ψ accumulated upon propagation from one Weyl point to the next is gauge dependent, we choose the Landau gauge $\boldsymbol{A} = (0, -Bz, 0)$. For simplicity we ignore the curvature of the open orbits, approximating them by straight contours along the line $k_y = E/\hbar v_y$. The phase shift is then given by

$$\psi = \frac{E}{\hbar v_y} \frac{\pi}{a_0} l_m^2 = \frac{\pi E}{\hbar \omega_c}, \tag{3.24}$$

the same for each segment of an open orbit connecting two Weyl points.

The quantization condition for a Landau level at energy E_n is $2\psi + \phi = 2\pi n$, $n = 1, 2, \ldots$, which amounts to the quantization in units of h/e of the magnetic flux through the real-space area $S_\Sigma l_m^4$. Since $S_\Sigma \gg S_0$ the Landau level spacing is governed by the energy dependence of ψ,

$$E_{n+1} - E_n \approx \pi (d\psi/dE)^{-1} = \hbar\omega_c. \tag{3.25}$$

The Landau level spacing increases $\propto B$ and not $\propto \sqrt{B}$, as one might have expected for massless electrons. The origin of the difference is explained in Fig. 3.6.

The Landau levels are flat when $T_{\rm MB} = T'_{\rm MB} = 1$, so that there are no open orbits. The open orbits introduce a dispersion along k_y, see Fig. 3.7.

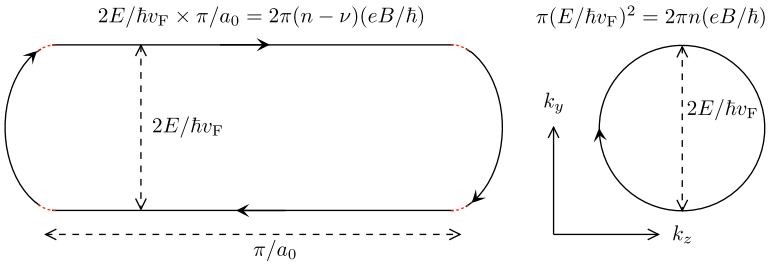

Figure 3.6: Equi-energy contours in the k_y–k_z plane for surface Fermi arcs coupled by magnetic breakdown (left panel, schematic) and for the bulk cyclotron orbit of a Weyl fermion (right panel). The quantization condition for the enclosed area is indicated, to explain why the Landau level spacing is $\propto B$ for the Fermi arcs, while it is $\propto \sqrt{B}$ for the cyclotron orbit.

Full expressions are given in App. 3.C. For $R_\mathrm{MB}, R'_\mathrm{MB} \ll 1$ and $S_0 = S'_0$ we have the dispersion

$$E(k_y) = (n-\nu)\hbar\omega_c \pm (\hbar\omega_c/\pi)\sin(\phi/2) \times \left(R_\mathrm{MB} + R'_\mathrm{MB} + 2\sqrt{R_\mathrm{MB}R'_\mathrm{MB}}\cos k_y\mathcal{L}\right)^{1/2}, \tag{3.26}$$

where the phase ϕ is to be evaluated at $E = (n-\nu)\hbar\omega_c$.

Each Landau level is split into two subbands having the same band width

$$|E(0) - E(\pi/\mathcal{L})| = 2(\hbar\omega_c/\pi)|\sin(\phi/2)|\min(\sqrt{R}_\mathrm{MB}, \sqrt{R'}_\mathrm{MB}). \tag{3.27}$$

The band width oscillates periodically in $1/B$ with period (3.21).

3.6 Magnetoconductance oscillations

The dispersive Landau bands leave observable signatures in electrical conduction, in the form of magnetoconductance oscillations due to the resonant coupling of closed and open orbits. These have been previously studied when the open orbits are caused by an electrostatic superlattice [56–60]. We apply that theory to our setting.

From the dispersion relation (3.26) we calculate the square of the group

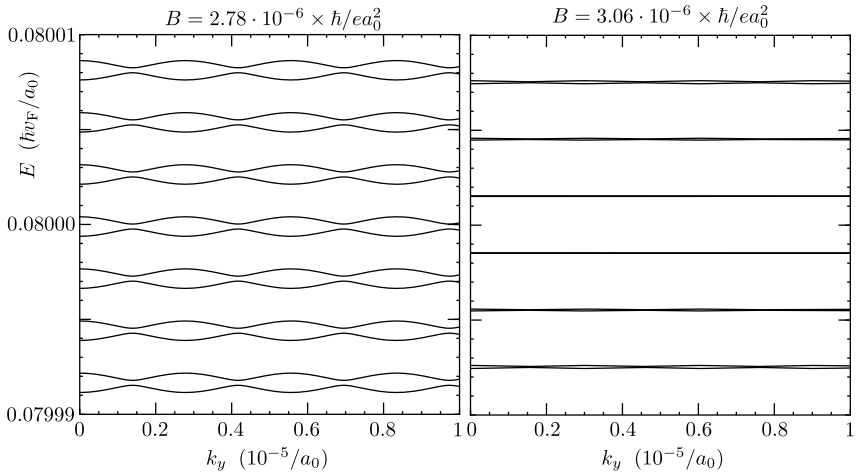

Figure 3.7: Dispersion relation of the slab in a perpendicular magnetic field B, calculated from Eqs. (3.47) and (3.48) (for $W = 20\,a_0$, $T_{\rm MB} = 0.85$, $T'_{\rm MB} = 0.95$, $S_0{=}S'_0$, $\nu = 0$). In the left panel B is chosen such that the phase ϕ accumulated by a closed orbit at $E = 0.08\,\hbar v_{\rm F}/a_0$ equals 11π, in the right panel $\phi = 10\pi$. When ϕ is an integer multiple of 2π the magnetic breakdown is resonant, all orbits are closed and the Landau bands are dispersionless. When ϕ is a half-integer multiple of 2π the magnetic breakdown is suppressed and the Landau bands acquire a dispersion from the open orbits.

velocity $\mathcal{V} = \partial E/\hbar\partial k_y$, averaged over the Landau band,

$$\begin{aligned}\langle \mathcal{V}^2 \rangle &= \frac{\mathcal{L}}{2\pi} \int_0^{2\pi/\mathcal{L}} \left(\frac{dE(k_y)}{\hbar dk_y} \right)^2 dk_y \\ &= 2v_y^2 \sin^2(\phi/2) \min(R_{\rm MB}, R'_{\rm MB}). \end{aligned} \tag{3.28}$$

For weak impurity scattering, scattering rate $1/\tau_{\rm imp} \ll \omega_c$, the effective diffusion coefficient [60],

$$D_{\rm eff} = \tau_{\rm imp} \langle \mathcal{V}^2 \rangle, \tag{3.29}$$

and the 2D density of states $N_{\rm 2D} = (\pi\hbar v_y a_0)^{-1}$ of the Landau band, determine the oscillatory contribution $\delta\sigma_{yy}$ to the longitudinal conductivity via the Drude formula for a 2D electron gas,

$$\begin{aligned}\delta\sigma_{yy} &= e^2 N_{\rm 2D} D_{\rm eff} \\ &= \frac{4e^2}{h} \frac{v_y \tau_{\rm imp}}{a_0} \sin^2(\phi/2) \min(R_{\rm MB}, R'_{\rm MB}). \end{aligned} \tag{3.30}$$

The magnetoconductance oscillations due to magnetic breakdown (MB) coexist with the Shubnikov-de Haas (SdH) oscillations due to Landau level quantization. Both are periodic in $1/B$, but with very different period, see Eqs. (3.21) and (3.22).

The difference in period causes a different temperature dependence of the magnetoconductance oscillations. A conductance measurement at temperature T corresponds to an energy average over a range $\Delta E \approx 4k_{\rm B}T$ (being the full-width-at-half-maximum of the derivative of the Fermi-Dirac distribution). The oscillations become unobservable when the energy average changes the area S_0 or S_Σ by more than π/l_m^2. This results in different characteristic energy or temperature scales,

$$\Delta E_{\rm SdH} = \frac{\pi}{l_m^2}\left(\frac{\partial S_\Sigma}{\partial E}\right)^{-1} \simeq \tfrac{1}{2}\hbar\omega_c, \tag{3.31a}$$

$$\Delta E_{\rm MB} = \frac{\pi}{l_m^2}\left(\frac{\partial S_0}{\partial E}\right)^{-1} \simeq \tfrac{1}{4}\sqrt{2}(W/W_c-1)^{-1/2}\frac{\hbar\omega_c}{k_{\rm F}a_0}. \tag{3.31b}$$

(In the second equation we took $W/W_c \gtrsim 1$.) For $k_{\rm F}a_0 \ll 1$ and W/W_c close to unity we may have $\Delta E_{\rm SdH} \ll \Delta E_{\rm MB}$, so there is an intermediate temperature regime $\Delta E_{\rm SdH} \lesssim 4k_{\rm B}T \lesssim \Delta E_{\rm MB}$ where the Shubnikov-de Haas oscillations are suppressed while the magnetic breakdown oscillations remain.

3.7 Tight-binding model on a cubic lattice

We have tested the analytical calculations from the previous sections numerically, on a tight-binding model of a Kramers-Weyl semimetal [9]. In this section we describe the model, results are presented in the next section.

3.7.1 Hamiltonian

We take a simple cubic lattice (lattice constant a, one atom per unit cell), when the nearest-neighbor hopping terms are the same in each direction $\alpha \in \{x, y, z\}$. There are two terms to consider, a spin-independent term $\propto t_0$ that is even in momentum and a spin-orbit coupling term $\propto t_1\sigma_\alpha$ that is odd in momentum,

$$H = t_0\sum_\alpha \cos(k_\alpha a) + t_1\sum_\alpha \sigma_\alpha \sin(k_\alpha a) - t_0. \tag{3.32}$$

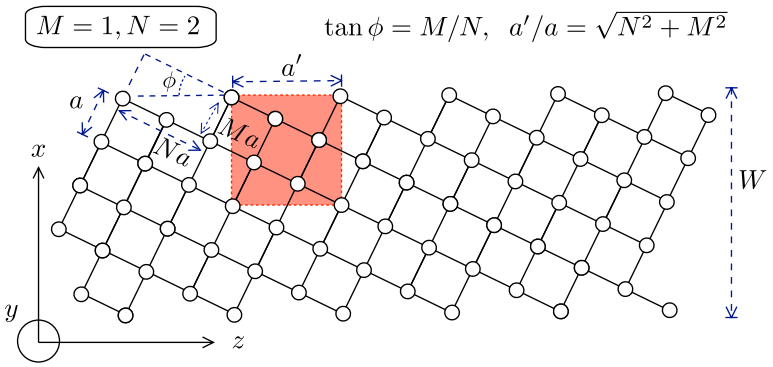

Figure 3.8: Slice at $y = 0$ through the cubic lattice, rotated around the y-axis by an angle $\phi = \arctan(M/N)$ with $M = 1$, $N = 2$. The enlarged unit cell (red square), parallel to a lattice termination at $x = 0$ and $x = W$, has volume $a' \times a' \times a = (N^2 + M^2)a^3$.

The offset is arbitrarily fixed at $-t_0$.

There are 8 Weyl points (momenta $\boldsymbol{k}$ in the Brillouin zone of a linear dispersion), located at $k_x, k_y, k_z \in \{0, \pi\}$ modulo 2π. The Weyl points at $(k_x, k_y, k_z) = (0,0,0), (\pi,\pi,0), (\pi,0,\pi), (0,\pi,\pi)$ have positive chirality and those at $(\pi,\pi,\pi), (\pi,0,0), (0,\pi,0), (0,0,\pi)$ have negative chirality [9].

The geometry is a slab, with a normal $\hat{n}$ in the x–z plane at an angle ϕ with the x-axis (so the normal is rotated by ϕ around the y-axis). The boundaries of the slab are constructed by removing all sites at $x < 0$ and $x > W$. In the rotated basis aligned with the normal to the slab one has

$$\begin{pmatrix} k'_x \\ k'_z \end{pmatrix} = \begin{pmatrix} \cos\phi & \sin\phi \\ -\sin\phi & \cos\phi \end{pmatrix} \begin{pmatrix} k_x \\ k_z \end{pmatrix}, \quad k'_y = k_y. \tag{3.33}$$

We will work in this rotated basis and for ease of notation omit the prime, writing k_x or $k_\perp$ for the momentum component perpendicular to the slab and $(k_y, k_z) = \boldsymbol{k}_\parallel$ for the parallel momenta.

3.7.2 Folded Brillouin zone

The termination of the lattice in the slab geometry breaks the translation invariance in the perpendicular x-direction as well as in the z-direction parallel to the surface. If the rotation angle $\phi \in (0, \pi/2]$ is chosen such that $\tan\phi = M/N$ is a rational number (M and N being coprime integers), the translational invariance in the z-direction is restored with a larger lattice

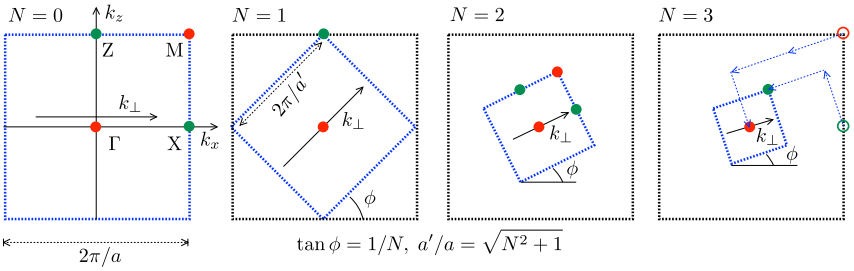

Figure 3.9: Slice at $k_y = 0$ through the Brillouin zone of the rotated cubic lattice, for rotation angles $\phi = \arctan(M/N)$ with $M = 1$, $N = 0, 1, 2, 3$. Weyl points of opposite chirality are marked by a green or red dot. The panel for $N = 3$ shows how translation by reciprocal lattice vectors (blue arrows) folds two Weyl points onto each other.

constant $a' = a\sqrt{N^2 + M^2}$, see Fig. 3.8. There are then $N^2 + M^2$ atoms in a unit cell.

In reciprocal space the enlarged unit cell folds the Brillouin zone. Relative to the original Brillouin zone the folded Brillouin zone is rotated by an angle ϕ around the y-axis and scaled by a factor $(N^2 + M^2)^{-1/2}$ in the x and z-directions, see Fig. 3.9. The reciprocal lattice vectors in the rotated basis are

$$\boldsymbol{e}_x = (2\pi/a')\hat{x}, \quad \boldsymbol{e}_y = (2\pi/a)\hat{y}, \quad \boldsymbol{e}_z = (2\pi/a')\hat{z}. \tag{3.34}$$

The corner in the $k_y = 0$ plane of the original Brillouin zone (the M point) has coordinates

$$\frac{\pi}{a}(\cos\phi + \sin\phi, \cos\phi - \sin\phi, 0) = \frac{\pi}{a'}(N + M, N - M, 0)$$

in the rotated lattice. Upon translation over a reciprocal lattice vector this is folded onto the center of the Brillouin zone (the Γ point) when $N + M$ is an even integer, while it remains at a corner for $N + M$ odd. The midpoints of a zone boundary, the X and Z points, are folded similarly, as summarized by

$$\begin{aligned} &\mathrm{M} \mapsto \Gamma, \quad \Gamma \mapsto \Gamma, \quad \mathrm{X} \mapsto \mathrm{M}, \quad \mathrm{Z} \mapsto \mathrm{M}, \quad \text{for} \quad N + M \quad \text{even}, \\ &\mathrm{M} \mapsto \mathrm{M}, \quad \Gamma \mapsto \Gamma, \quad \mathrm{X} \mapsto \mathrm{X}, \quad \mathrm{Z} \mapsto \mathrm{Z}, \quad \text{for} \quad N + M \quad \text{odd}. \end{aligned}$$

Since the Weyl points at Γ and M have the same chirality, for $N + M$ even we are in the situation that the surface of the slab couples Weyl

points of the same chirality — which is required for surface Fermi arcs to appear (see Sec. 3.2). For $N + M$ odd, in contrast, the Weyl points at the Γ and X points of opposite chirality are coupled by the surface, since these line up along the $k_\perp$ axis. Then surface Fermi arcs will not appear. In App. 3.B we present a general analysis, for arbitrary Bravais lattices, that determines which lattice terminations support Fermi arcs and which do not.

3.8 Tight-binding model results

We present results for $M = N = 1$, corresponding to a $\phi = \pi/4$ rotation of the lattice around the y-axis. The folded and rotated Brillouin zone has a pair of Weyl points of + chirality at $\boldsymbol{K} = (0, 0, 0)$ and a second pair of − chirality at $\boldsymbol{K}' = (\pi/a', 0, \pi/a')$ in the rotated coordinates (see Fig. 3.9, second panel, with $a' = a\sqrt{2}$). There is a second pair translated by $k_y = \pi/a$.

Each Weyl point supports a pair of Weyl cones of the same chirality, folded onto each other in the first Brillouin zone. The Weyl cones at $\boldsymbol{K}$ have energy offset $\varepsilon = |2t_0|$, while those at $\boldsymbol{K}'$ have $\varepsilon' = 0$. We may adjust the offset by adding a rotational symmetry breaking term $\delta H = \delta t_0 \cos k_z a$ to the tight-binding Hamiltonian (3.32). This changes the offsets into

$$\varepsilon = |2t_0 + \delta t_0|, \quad \varepsilon' = |\delta t_0|. \tag{3.35}$$

In Fig.3.10 we show how the Fermi arcs appear in the dispersion relation connecting the Weyl cones at $k_z = 0$ and $k_z = \pi/a'$. This figure extends the local description near a Weyl cone from Fig. 3.2 to the entire Brillouin zone. The corresponding equi-energy contours are presented in Fig. 3.11. Increasing the spin-independent hopping term t_0 introduces more bands, but the qualitative picture near the center of the Brillouin zone remains the same as in Fig. 3.3 for $W > W_c$.

The effect on the dispersion of a magnetic field B, perpendicular to the slab, is shown in Fig. 3.12 (see also App. 3.D). The field was incorporated in the tight-binding model via the Peierls substitution in the gauge $\boldsymbol{A} = (0, -Bz, 0)$, with coordinate z restricted to $|z| < L/2$. Translational invariance in the y-direction is maintained, so we have a one-dimensional dispersion $E(k_y)$. The boundaries of the system at $z = \pm L/2$ introduce edge modes, which are visible in panel a as linearly dispersing modes near $k_y = \pm\frac{1}{2}L/l_m^2$ (modulo π/a). Panels b,c,d focus on the region near $k_y = 0$, where these edge effects can be neglected. The effect on the dispersion of a variation in ε and ε' is qualitatively similar to that obtained from the

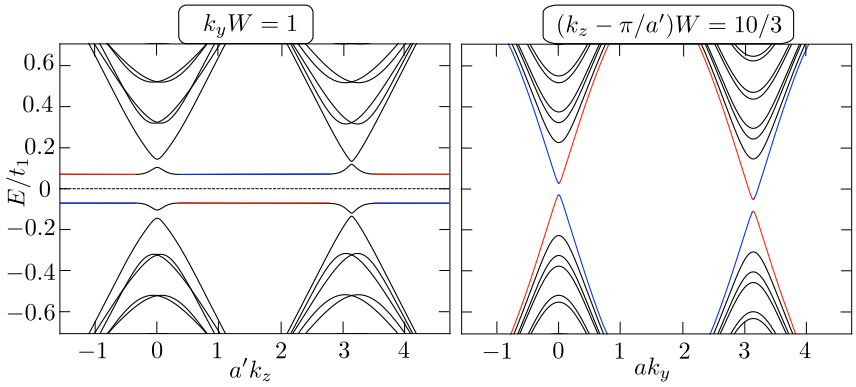

Figure 3.10: Dispersion relations of a slab (thickness $W = 10\sqrt{2}\,a$ in the x-direction, infinitely extended in the y–z plane) in zero magnetic field. The plots are calculated from the tight-binding model of Sec. 6.A (with $t_0 = 0.04\,t_1$, $\delta t_0 = -0.02\,t_1$, corresponding to $\varepsilon = 0.06\,t_1$, $\varepsilon' = 0.02\,t_1$). The left and right panels show the dispersion as a function of k_z and k_y, respectively. The curves are colored according to the electron density on the surfaces: red for the bottom surface, blue for the top surface, with bulk states appearing black.

analytical solution of the continuum model, compare the four panels of Fig. 3.12 with the corresponding panels in Fig. 3.16.

The width δE of the dispersive Landau bands (from maximum to minimum energy) is plotted as a function of $1/B$ in Fig. 3.13 and the periodicity $\Delta(1/B)$ is compared with the predicted Eq. (3.21) in Fig. 3.14. To remove the rapid Shubnikov-De Haas (SdH) oscillations we averaged over an energy interval ΔE around E_F. This corresponds to a thermal average at effective temperature $T_\mathrm{eff} = \Delta E/4k_\mathrm{B}$. From Eq. (3.31), with $k_\mathrm{F}a \approx 0.2$, $W/W_c \approx 1.5$, we estimate that the characteristic energy scale at which the oscillations average out is five times smaller for the SdH oscillations than for the oscillations due to magnetic breakdown, consistent with what we see in the numerics.

3.9 Conclusion

In conclusion, we have shown that Kramers-Weyl fermions (massless fermions near time-reversally invariant momenta) confined to a thin slab have a fundamentally different Landau level spectrum than generic massless electrons: The Landau levels are not flat but broadened with a band

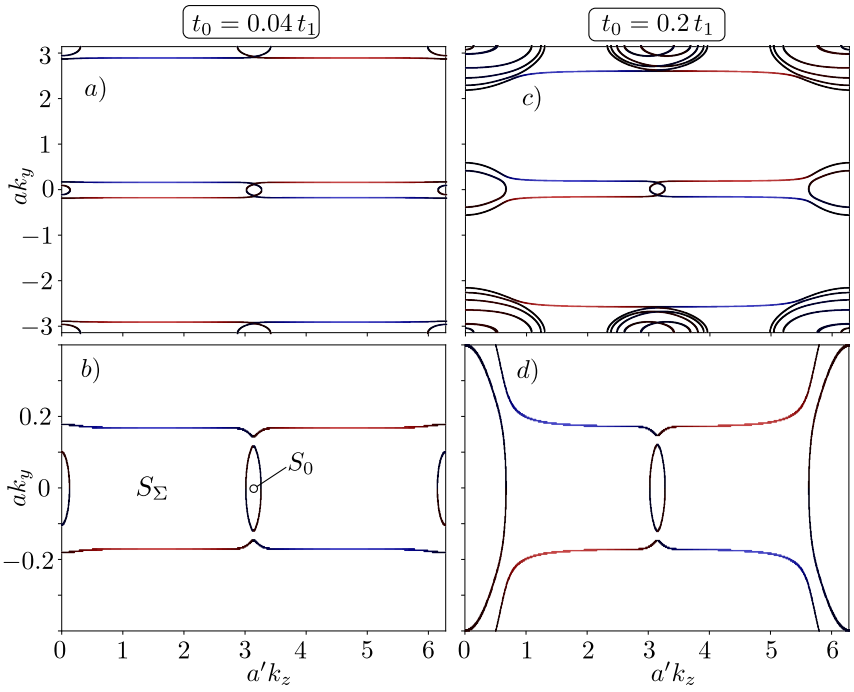

Figure 3.11: Panels a (full Brillouin zone) and b (zoom-in near $k_y = 0$) show equi-energy contours at $E = 0.167\,t_1$ (when $W \approx 1.5\,W_c$), for the same system as in Fig. 3.10. In panels c and d the spin-independent hopping term t_0 is increased by a factor 5 (at the same $\delta t_0 = -0.02\,t_1$).

width that oscillates periodically in $1/B$. The origin of the dispersion is magnetic breakdown at Weyl points, which couples open orbits from surface Fermi arcs to closed orbits in the interior of the slab.

The band width oscillations are observable as a slow modulation of the conductance with magnetic field, on which the rapid Shubnikov-de Haas oscillations are superimposed. The periodicities are widely separated because the quantized areas in the Brillouin zone are very different (compare the areas S_0 and S_Σ in Fig. 3.5). This is a robust feature of the band structure of a Kramers-Weyl semimetal, as illustrated in the model calculation of Fig. 3.11. Since generic Weyl fermions have only the Shubnikov-de Haas oscillations, the observation of two distinct periodicities in the magnetoconductance would provide for a unique signature of Kramers-Weyl fermions.

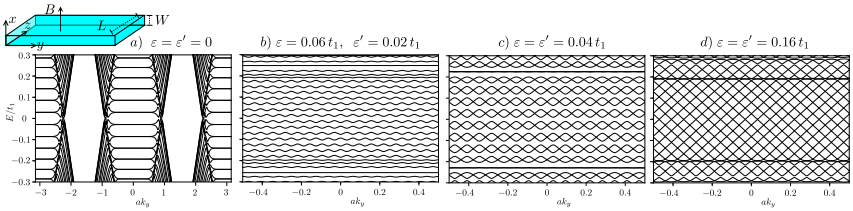

Figure 3.12: Dispersion relation of a strip (cross-section $W \times L$ with $W = 10a'$ and $L = 30a'$) in a perpendicular magnetic field $B = 0.00707\,(h/ea^2)$ (magnetic length $l_m = 4.74\,a$). The four panels correspond to $t_0/t_1, \delta t_0/t_1$ equal to $0, 0$ (panel a), $0.04, -0.02$ (panel b), $0.04, -0.04$ (panel c), $0.16, -0.16$ (panel d). The surface Fermi arcs near $k_y = 0$ form closed orbits in panel a, producing flat Landau levels, while in panel d they form open orbits with the same linear dispersion as in zero field. Panels b,c show an intermediate regime where magnetic breakdown between closed and open orbits produces Landau bands with an oscillatory dispersion.

The dispersive Landau band is interpreted as the band structure of a one-dimensional superlattice of magnetic breakdown centra, separated in real space by a distance $\mathcal{L} = (eBa_0/h)^{-1}$ — which in weak fields is much larger than the atomic lattice constant a_0. Such a magnetic breakdown lattice has been studied in the past for massive electrons [70], the Kramers-Weyl semimetals would provide an opportunity to investigate their properties for massless electrons.

The tight-binding model calculations were performed using the Kwant code [47].

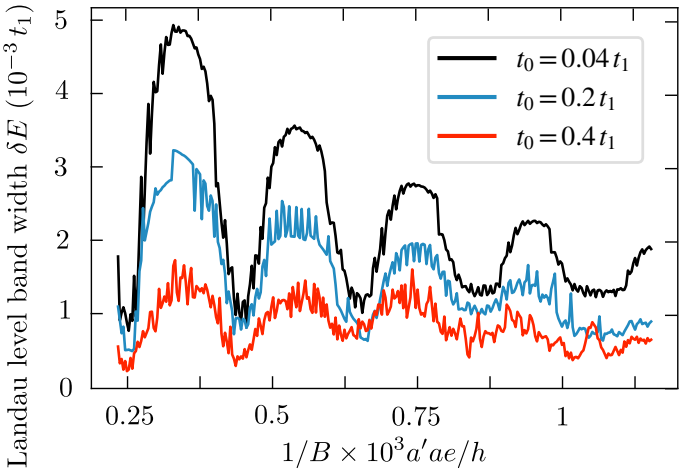

Figure 3.13: Band width of the Landau levels versus inverse of magnetic field for $W = 10a'$, $L = 500a'$, $\delta t_0 = -0.02\,t_1$ and three different values of t_0. The band widths are averaged over an energy window $\Delta E = 0.004\,t_1$ around the Fermi energy $E_\mathrm{F} = 0.167\,t_1$. The rapid Shubnikov-de Haas oscillations are averaged out, only the slow oscillations due to magnetic breakdown persist.

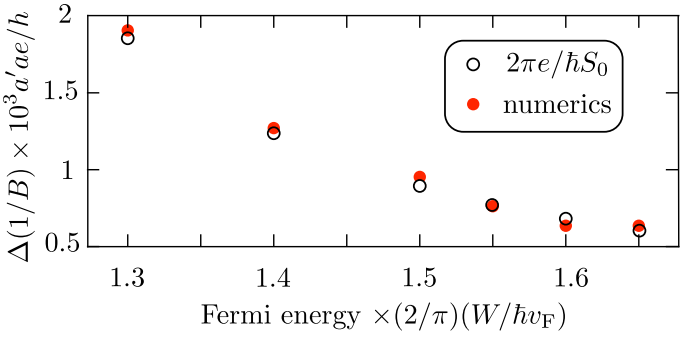

Figure 3.14: Periodicity in $1/B$ of the Landau band width oscillations as a function of the Fermi energy, for $W = 10a'$, $L = 500a'$, $t_0 = 0.04\,t_1$, and $\delta t_0 = -0.02\,t_1$. The filled data points are obtained numerically from the Landau band spectrum, similarly to the data shown for one particular E_F in Fig. 3.13. The open circles are calculated from the area S_0 of the closed orbit in momentum space (as indicated in Fig. 3.11*b*), using the formula $\Delta(1/B) = 2\pi e/\hbar S_0$.

Appendices

3.A Coupling of time-reversally invariant momenta by the boundary

The derivation of the boundary condition for Kramers-Weyl fermions in Sec. 3.2 relies on pairwise coupling of Weyl cones at a TRIM by the boundary. Let us demonstrate that this is indeed what happens.

Consider a 3D Bravais lattice and its Brillouin zone. A time-reversally-invariant momentum (TRIM) is by definition a momentum $\boldsymbol{K}$ such that $\boldsymbol{K} = -\boldsymbol{K} + \boldsymbol{G}$ with $\boldsymbol{G}$ a reciprocal lattice vector, or equivalently, $\boldsymbol{K} = \frac{1}{2}\boldsymbol{G}$. Now consider the restriction of the lattice to $x > 0$, by removing all lattice points at $x < 0$. Assume that the restricted lattice is still periodic in the y–z plane, with an enlarged unit cell. Fig. 3.8 shows an example for a cubic lattice.

The enlarged unit cell will correspond to a reduced Brillouin zone, with a new set of reciprocal lattice vectors $\tilde{\boldsymbol{G}}$. The original set $\boldsymbol{K}_1, \boldsymbol{K}_2, \boldsymbol{K}_3, \ldots$ of TRIM is folded onto a new set $\tilde{\boldsymbol{K}}_1, \tilde{\boldsymbol{K}}_2, \tilde{\boldsymbol{K}}_3, \ldots$ in the reduced Brillouin zone. The folding may introduce degeneracies, such that two different $\boldsymbol{K}$'s are folded onto the same $\tilde{\boldsymbol{K}}$. The statement to prove is this:

- Each TRIM $\tilde{\boldsymbol{K}}$ in the folded Brillouin zone is either degenerate (because two $\boldsymbol{K}$'s were folded onto the same $\tilde{\boldsymbol{K}}$), or there is a second TRIM $\tilde{\boldsymbol{K}}'$ along the k_x-axis.

Fig. 3.9 illustrates that this statement is true for the cubic lattice. We wish to prove that it holds for any Bravais lattice.

Enlargement of the unit cell changes the primitive lattice vectors from $\boldsymbol{a}_1, \boldsymbol{a}_2, \boldsymbol{a}_3$ into $\tilde{\boldsymbol{a}}_1, \tilde{\boldsymbol{a}}_2, \tilde{\boldsymbol{a}}_3$. The two sets are related by integer coefficients n_{ij},

$$\tilde{\boldsymbol{a}}_i = \sum_{j=1}^{3} n_{ij} \boldsymbol{a}_j, \quad n_{ij} \in \mathbb{Z}. \tag{3.36}$$

The corresponding primitive vectors $\boldsymbol{b}$, $\tilde{\boldsymbol{b}}$ in reciprocal space satisfy

$$\boldsymbol{b}_i \cdot \boldsymbol{a}_j = 2\pi\delta_{ij}, \quad \tilde{\boldsymbol{b}}_i \cdot \tilde{\boldsymbol{a}}_j = 2\pi\delta_{ij}. \tag{3.37}$$

Any momentum $\boldsymbol{k}$ can thus be expanded as

$$\boldsymbol{k} = \frac{1}{2\pi}\sum_{i=1}^{3}(\tilde{\boldsymbol{a}}_i \cdot \boldsymbol{k})\tilde{\boldsymbol{b}}_i = \frac{1}{2\pi}\sum_{i,j=1}^{3} n_{ij}(\boldsymbol{a}_j \cdot \boldsymbol{k})\tilde{\boldsymbol{b}}_i. \tag{3.38}$$

A TRIM $\boldsymbol{K}_\alpha$ in the first Brillouin zone of the original lattice is given by

$$\boldsymbol{K}_\alpha = \tfrac{1}{2}\sum_{i=1}^{3} m_{\alpha,i}\boldsymbol{b}_i, \quad m_{\alpha,i} \in \{0,1\}. \tag{3.39}$$

The index α labels each TRIM, identified by the 8 distinct triples $(m_{\alpha,1}, m_{\alpha,2}, m_{\alpha,3}) \in \mathbb{Z}_2 \otimes \mathbb{Z}_2 \otimes \mathbb{Z}_2$. Subsitution into the expansion (3.38) gives

$$\begin{aligned}\boldsymbol{K}_\alpha &= \tfrac{1}{2}\sum_{l=1}^{3} m_{\alpha,l}\left(\frac{1}{2\pi}\sum_{i,j=1}^{3} n_{ij}(\boldsymbol{a}_j \cdot \boldsymbol{b}_l)\tilde{\boldsymbol{b}}_i\right) \\ &= \tfrac{1}{2}\sum_{i,j=1}^{3} m_{\alpha,j} n_{ij}\tilde{\boldsymbol{b}}_i. \end{aligned} \tag{3.40}$$

	$m_{\alpha,1}\, m_{\alpha,2}\, m_{\alpha,3}$							
$n_{i1}\, n_{i2}\, n_{i3}$ (mod 2)	000	001	010	011	100	101	110	111
000	0	0	0	0	0	0	0	0
001	0	$\frac{1}{2}$	0	$\frac{1}{2}$	0	$\frac{1}{2}$	0	$\frac{1}{2}$
010	0	0	$\frac{1}{2}$	$\frac{1}{2}$	0	0	$\frac{1}{2}$	$\frac{1}{2}$
011	0	$\frac{1}{2}$	$\frac{1}{2}$	0	0	$\frac{1}{2}$	$\frac{1}{2}$	0
100	0	0	0	0	$\frac{1}{2}$	$\frac{1}{2}$	$\frac{1}{2}$	$\frac{1}{2}$
101	0	$\frac{1}{2}$	0	$\frac{1}{2}$	$\frac{1}{2}$	0	$\frac{1}{2}$	0
110	0	0	$\frac{1}{2}$	$\frac{1}{2}$	$\frac{1}{2}$	$\frac{1}{2}$	0	0
111	0	$\frac{1}{2}$	$\frac{1}{2}$	0	$\frac{1}{2}$	0	0	$\frac{1}{2}$

Table 3.1: Values of $\nu_{\alpha,i}$ calculated from Eq. (3.41), for each triple $n_{i1}\, n_{i2}\, n_{i3}$ and each triple $m_{\alpha,1}\, m_{\alpha,2}\, m_{\alpha,3}$ (both $\in \mathbb{Z}_2 \otimes \mathbb{Z}_2 \otimes \mathbb{Z}_2$). If we select any two rows and intersect with any column to obtain an ordered pair of values ν, ν', we can then find a second column with the same ν, ν' at the intersection.

We now fold $\boldsymbol{K}_\alpha \mapsto \tilde{\boldsymbol{K}}_\alpha$ into the first Brillouin zone of the $\tilde{\boldsymbol{b}}$ reciprocal

vectors,

$$\begin{aligned} \tilde{\boldsymbol{K}}_\alpha &= \sum_{i=1}^{3} \nu_{\alpha,i} \tilde{\boldsymbol{b}}_i, \quad \nu_{\alpha,i} \in [0,1), \\ \nu_{\alpha,i} &= \tfrac{1}{2} \sum_{j=1}^{3} m_{\alpha,j} n_{ij} \pmod 1. \end{aligned} \tag{3.41}$$

In Table 3.1 we list for each TRIM and each choice of $(n_{i1}, n_{i2}, n_{i3}) \in \mathbb{Z}_2 \otimes \mathbb{Z}_2 \otimes \mathbb{Z}_2$ the corresponding value of $\nu_{\alpha,i} \in \{0, \frac{1}{2}\}$.

We fix the y and z-components of $\tilde{\boldsymbol{K}}_\alpha$ by specifying $\nu_{\alpha,2}$ and $\nu_{\alpha,3} \in \{0, \frac{1}{2}\}$ and ask how many choices of α remain, so how many values of α satisfy the two equations

$$\begin{aligned} \nu_{\alpha,2} &= \tfrac{1}{2} \sum_{i=1}^{3} n_{2i} m_{\alpha,i} \pmod 1, \\ \nu_{\alpha,3} &= \tfrac{1}{2} \sum_{i=1}^{3} n_{3i} m_{\alpha,i} \pmod 1. \end{aligned} \tag{3.42}$$

Inspection of Table 3.1 shows that the number of solutions is even. More specifically, there are

- 8 solutions if n_{21}, n_{22}, n_{23} and n_{31}, n_{32}, n_{33} both equal 000 mod 2;
- 4 solutions if only one of n_{21}, n_{22}, n_{23} and n_{31}, n_{32}, n_{33} equals 000 mod 2;
- 4 solutions if n_{21}, n_{22}, n_{23} and n_{31}, n_{32}, n_{33} are identical and different from 000 mod 2;
- 2 solutions otherwise.

The multiple solutions correspond to pairs $\boldsymbol{K}_\alpha$ and $\boldsymbol{K}_\beta$ that are either folded onto the same $\tilde{\boldsymbol{K}}_\alpha = \tilde{\boldsymbol{K}}_\beta$ (if $\det n = 0 \bmod 2$), or onto $\tilde{\boldsymbol{K}}_\alpha$ and $\tilde{\boldsymbol{K}}_\beta$ that differ only in the x-component (if $\det n = 1 \bmod 2$). These are the TRIM that are coupled by the boundary normal to the x-axis.

3.B Criterion for the appearance of surface Fermi arcs

When the boundary couples only Weyl cones of the same chirality, these persist and give rise to surface Fermi arcs. If, however, opposite chiralities

are coupled, then the boundary gaps out the Weyl cones and no Fermi arcs appear. Which of these two possibilities is realized can be determined by using that the parity of $m_{\alpha 1} + m_{\alpha 2} + m_{\alpha 3}$ determines the chirality of the Weyl cone at $\boldsymbol{K}_\alpha$.

Table 3.2 identifies for each choice of n_{21}, n_{22}, n_{33} and n_{31}, n_{32}, n_{33} how many pairs of Weyl cones of opposite chirality are folded onto the same point of the surface Brillouin zone. We conclude that surface Fermi arcs appear if either

- $n_{2i} + n_{3i} = 1 \bmod 2$ for each i, or
- $n_{21}, n_{22}, n_{23} = 111 \bmod 2$, or
- $n_{31}, n_{32}, n_{33} = 111 \bmod 2$.

	$n_{31}\, n_{32}\, n_{33}$ (mod 2)							
$n_{21}\, n_{22}\, n_{23}$ (mod 2)	000	001	010	011	100	101	110	111
000	4	2	2	2	2	2	2	0
001	2	2	1	1	1	1	0	0
010	2	1	2	1	1	0	1	0
011	2	1	1	2	0	1	1	0
100	2	1	1	0	2	1	1	0
101	2	1	0	1	1	2	1	0
110	2	0	1	1	1	1	2	0
111	0	0	0	0	0	0	0	0

Table 3.2: Number of pairs of opposite-chirality Weyl cones that are coupled by a surface termination characterized by the integers n_{2i}, n_{3i}, $i \in \{1, 2, 3\}$. When this number equals 0 the surface couples only Weyl cones of the same chirality and surface Fermi arcs will appear. If the number is different from zero the surface does not support Fermi arcs.

3.C Calculation of the dispersive Landau bands due to the coupling of open and closed orbits

To calculate the effect of the coupling of open and closed orbits on the Landau levels we apply the scattering theory of Refs. 60, 70, 72 to the equi-energy contours shown in Fig. 3.15. We distinguish the two Weyl points at

$k_z = 0$ and $k_z = \pi/a_0$ by their different magnetic breakdown probability, denoted respectively by $T_{\mathrm{MB}} = 1 - R_{\mathrm{MB}}$ and $T'_{\mathrm{MB}} = 1 - R'_{\mathrm{MB}}$. The areas of the closed orbits may also differ, we denote these by S_0 and S'_0 and the corresponding phase shifts by $\phi = S_0 l_m^2 + 2\pi\nu$ and $\phi' = S'_0 l_m^2 + 2\pi\nu$.

The coupling of the closed and open orbits at these two Weyl points is described by a pair of scattering matrices, given by

$$\begin{pmatrix} b_{\mathrm{L}}^- \\ b_{\mathrm{R}}^+ \end{pmatrix} = \begin{pmatrix} r & t \\ t & r \end{pmatrix} \cdot \begin{pmatrix} b_{\mathrm{L}}^+ \\ b_{\mathrm{R}}^- \end{pmatrix}, \quad r = \frac{T_{\mathrm{MB}} e^{i\phi/2}}{1 - R_{\mathrm{MB}} e^{i\phi}}, \tag{3.43a}$$

$$t = -\sqrt{R}_{\mathrm{MB}} + \frac{T_{\mathrm{MB}} \sqrt{R}_{\mathrm{MB}} e^{i\phi}}{1 - R_{\mathrm{MB}} e^{i\phi}}, \tag{3.43b}$$

for the Weyl point at $k_z = 0$, and similarly for the other Weyl point at $k_z = \pi/a_0$ (with $T_{\mathrm{MB}} \mapsto T'_{\mathrm{MB}}$, $\phi \mapsto \phi'$). The coefficients can be rearranged in an energy-dependent transfer matrix,

$$\begin{pmatrix} b_{\mathrm{R}}^+ \\ b_{\mathrm{R}}^- \end{pmatrix} = \mathcal{T}(E) \begin{pmatrix} b_{\mathrm{L}}^+ \\ b_{\mathrm{L}}^- \end{pmatrix}, \quad \mathcal{T} = \begin{pmatrix} t - r^2/t & r/t \\ -r/t & 1/t \end{pmatrix}, \tag{3.44}$$

and similarly for $\mathcal{T}'$ (with $t \mapsto t'$, $r \mapsto r'$). The transfer matrices are energy dependent via the energy dependence of S_0 and hence of ϕ.

We ignore the curvature of the open orbits, approximating them by straight contours along the line $k_y = E/\hbar v_y$. The phase shift accumulated upon propagation from one Weyl point to the next, in the Landau gauge $\boldsymbol{A} = (0, -Bz, 0)$, is then given by

$$\psi = \frac{E}{\hbar v_y} \frac{\pi}{a_0} l_m^2 = \frac{\pi E}{\hbar \omega_c}, \quad \omega_c = eBv_y a_0/\hbar. \tag{3.45}$$

The full transfer matrix over the first Brillouin zone takes the form

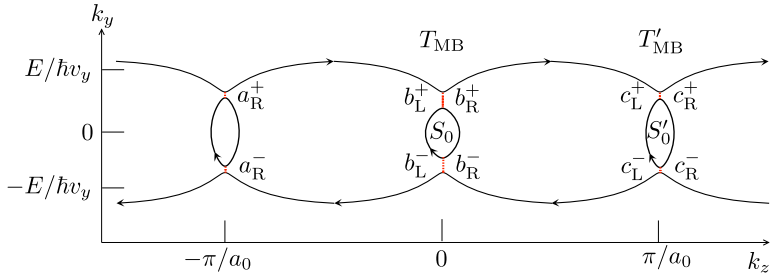

Figure 3.15: Equi-energy contours in the k_y–k_z plane. The labeled wave amplitudes are related by the scattering and transfer matrices (3.43)–(3.46).

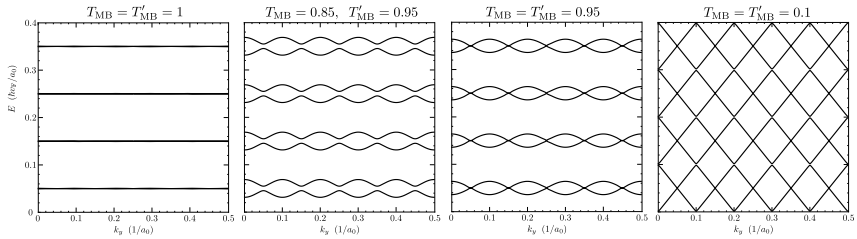

Figure 3.16: Dispersion relation of the slab in a perpendicular magnetic field, calculated from Eqs. (3.47) and (3.48) for $W = 1.8\,a_0$, $S_0{=}S'_0$, $\nu = 1/2$, $B = 0.1\,\hbar/ea_0^2$. The four panels correspond to different choices of the magnetic breakdown probabilities $T_{\rm MB}$ and $T'_{\rm MB}$ at the two Weyl points. At the two extremes of strong and weak magnetic breakdown we see dispersionless Landau levels (left-most panel) and linearly dispersing surface modes (right-most panel).

$$\begin{pmatrix} c_{\rm R}^{+} \\ c_{\rm R}^{-} \end{pmatrix} = \mathcal{T}_{\rm total}(E) \begin{pmatrix} a_{\rm R}^{+} \\ a_{\rm R}^{-} \end{pmatrix},$$
$$\mathcal{T}_{\rm total} = \begin{pmatrix} t' - r'^2/t' & r'/t' \\ -r'/t' & 1/t' \end{pmatrix} \begin{pmatrix} e^{i\psi} & 0 \\ 0 & e^{-i\psi} \end{pmatrix} \begin{pmatrix} t - r^2/t & r/t \\ -r/t & 1/t \end{pmatrix} \begin{pmatrix} e^{i\psi} & 0 \\ 0 & e^{-i\psi} \end{pmatrix}, \tag{3.46}$$

$$\operatorname{tr} \mathcal{T}_{\rm total} = \frac{\left(e^{i\phi} - R_{\rm MB}\right)\left(e^{i\phi'} - R'_{\rm MB}\right) + \left(1 - e^{i\phi} R_{\rm MB}\right)\left(1 - e^{i\phi'} R'_{\rm MB}\right)}{e^{2i\psi}\left(e^{i\phi} - 1\right)\left(e^{i\phi'} - 1\right)\sqrt{R_{\rm MB} R'_{\rm MB}}} - \frac{-2T_{\rm MB} T'_{\rm MB} e^{\frac{1}{2}i(\phi+\phi')+2i\psi}}{e^{2i\psi}\left(e^{i\phi} - 1\right)\left(e^{i\phi'} - 1\right)\sqrt{R_{\rm MB} R'_{\rm MB}}}. \tag{3.47}$$

Because $\det \mathcal{T}_{\rm total} = 1$, the eigenvalues of $\mathcal{T}_{\rm total}$ come in inverse pairs $\lambda, 1/\lambda$. The transfer matrix translates the wave function over a period $\mathcal{L}$ in real space, so we require that $\lambda = e^{iq\mathcal{L}}$ for some real wave number q, hence $\lambda + 1/\lambda = e^{iq\mathcal{L}} + e^{-iq\mathcal{L}}$, or equivalently [72]

$$\operatorname{tr} \mathcal{T}_{\rm total}(E) = 2\cos q\mathcal{L}. \tag{3.48}$$

(In the main text we denote q by k_y, here we choose a different symbol as a reminder that q is a conserved quantity, while the zero-field wave vector is not.) A numerical solution of Eq. (3.48) is shown in Figs. 3.7 and 3.16.

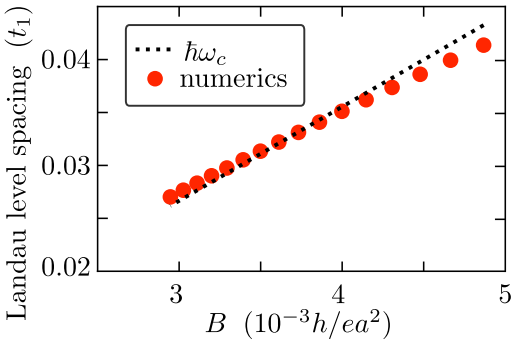

Figure 3.17: Magnetic field dependence of the energy spacing of the Landau levels near $E = 0$. The numerical data is for the slab geometry of Fig. 3.12 ($W = 11a'$, $L = 30a'$) at $t_0 = \delta t_0 = 0$ so that the probability of magnetic breakdown is unity and the Landau levels are dispersionless. The predicted energy spacing $\hbar\omega_c = eBv_{\rm F}a'$ is the black dotted line.

For $T_{\rm MB}$ and $T'_{\rm MB}$ close to unity an analytical solution $E_n(q)$ for the dispersive Landau bands can be obtained. We substitute $\psi = \pi(n-\nu) - (\phi+\phi')/4 + \pi\delta E/\hbar\omega_c$ into Eq. (3.47) and expand to second order in δE and to first order in $R_{\rm MB}, R'_{\rm MB}$. Then we equate to $2\cos q\mathcal{L}$ to arrive at

$$E_n^{\pm}(q) = (n-\nu)\hbar\omega_c \pm \delta E(q), \tag{3.49a}$$

$$(\pi\delta E/\hbar\omega_c)^2 = \rho + \rho' + 2\sqrt{\rho\rho'}\cos q\mathcal{L}, \tag{3.49b}$$

$$\rho = R_{\rm MB}\sin^2(\phi/2), \quad \rho' = R'_{\rm MB}\sin^2(\phi'/2), \tag{3.49c}$$

where ϕ and ϕ' are evaluated at $E = (n-\nu)\hbar\omega_c$. Corrections are of second order in $R_{\rm MB}$ and $R'_{\rm MB}$ and we have assumed that the areas S_0, S'_0 of the closed orbit are small compared to $k_{\rm F}/a_0$ — so that variations of ϕ and ϕ' over the Landau band can be neglected relative to the band spacing $\hbar\omega_c$.

3.D Landau levels from surface Fermi arcs

As explained in Fig. 3.6, the spacing of Landau levels formed out of surface Fermi arcs varies $\propto B$ — in contrast to the $\sqrt{B}$ dependence for unconfined massless electrons. In the tight-binding model of Sec. 6.A we can test this by setting $\varepsilon = \varepsilon' = 0$, so that there are only closed orbits and the Landau levels are dispersionless. The expected quantization is

$$E_n = (n-\nu)\hbar\omega_c, \quad \omega_c = eBv_{\rm F}a'/\hbar, \quad n = 0, 1, 2, \ldots \tag{3.50}$$

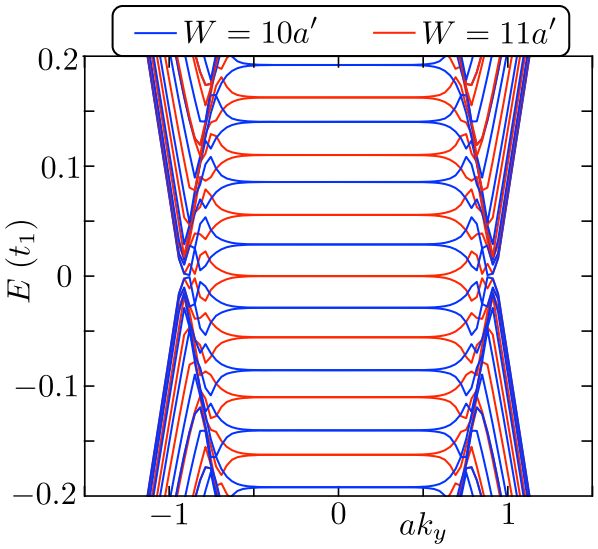

Figure 3.18: Dispersion relation of the tight-binding model with $t_0 = \delta t_0 = 0$, for $B = 7.07 \cdot 10^{-3}\, h/ea^2$, $L = 30a'$, and two values of $W = 10a'$ and $11a'$. The Landau levels are shifted by half a level spacing when W/a' switches from odd to even, indicating a shift of the offset ν from 0 to 1/2.

with v_F the velocity in the surface Fermi arc, connecting Weyl points spaced by π/a'. As shown in Fig. 3.17, this agrees nicely with the numerics.

In an unconfined 2D electron gas, the offset ν equals 1/2 or 0 for massive or massless electrons, respectively. For the surface Fermi arcs we observe that ν depends on the parity of the number of unit cells between top and bottom surface: $\nu = 0$ if W/a' is odd, while $\nu = 1/2$ if W/a' is even. This parity effect suggests that the coupling of Fermi arc states on opposite surfaces, needed to close the orbit in Fig. 3.1, introduces a phase shift that depends on the parity of W/a'. We are not aware of such a phase shift for generic Weyl semimetals [61, 62, 73, 74], it seems to be a characteristic feature of Kramers-Weyl fermions that deserves further study.

4 Supercell symmetry modified spectral statistics of Kramers-Weyl fermions

4.1 Introduction

The Wigner surmise $P(s) \propto s^\beta$ for the probability distribution of level spacings [75] is a quantum signature of chaos [76]. The exponent β, the Dyson index [77], can take on the values 1, 2 or 4, depending on the presence or absence of time-reversal symmetry and spin-rotation symmetry. Electrons in zero magnetic field have $\beta = 1$ in the absence of spin-orbit coupling and $\beta = 4$ with spin-orbit coupling, while $\beta = 2$ in a magnetic field irrespective of the spin degree of freedom. In the context of random-matrix theory one says that the Hamiltonian belongs to the universality class of the Gaussian Orthogonal Ensemble ($\beta = 1$, GOE), Gaussian Unitary Ensemble ($\beta = 2$, GUE), or Gaussian Symplectic Ensemble ($\beta = 4$, GSE).[1]

This classification applies both to massive electrons [78] (e.g. in a metal grain or in a semiconductor quantum dot) and to massless electrons [79] (e.g. in graphene or on the surface of a topological insulator). Here we consider a specific model in the latter category: Massless electrons (Weyl fermions) with a band crossing (Weyl point) enforced by Kramers degeneracy [9, 10]. These low-energy excitations known as Kramers-Weyl fermions appear at time-reversally invariant momenta $\mathbf{\Pi}$ in the Brillouin zone (such that $\mathbf{\Pi}$ and $-\mathbf{\Pi}$ differ by a reciprocal lattice vector). A strong spin-orbit coupling without reflection or mirror symmetry produces a linear band splitting $\pm(\boldsymbol{p} - \mathbf{\Pi}) \cdot \boldsymbol{\sigma}$ near each of the high-symmetry points. The $\pm$ sign designates the chirality of the excitations.

On a three-dimensional (3D) cubic lattice (unit lattice constant a_0) the

[1] The orthogonal, unitary, and symplectic matrices in this nomenclature refer to the matrix that diagonalizes the Hamiltonian.

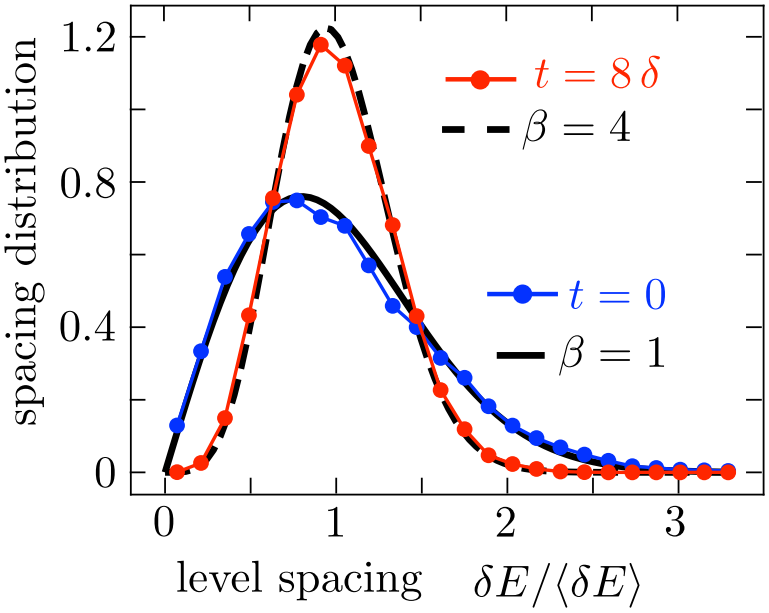

Figure 4.1: Distribution of the level spacings δE (normalized by the mean spacing $\langle\delta E\rangle \equiv \delta = 4.04 \cdot 10^{-3}\, v/a_0$) of the Hamiltonian (6.2), for $t = 0$ (blue) and $t \neq 0$ (red), on a $20\times20\times20$ cubic lattice. The potential V was chosen independently on each site from a uniform distribution in the interval $(-V_0/2, V_0/2)$ with $V_0 = 1.5\, v/a_0$. The solid and dashed black curves give the Wigner surmise for $\beta = 1$ and $\beta = 4$, respectively.

Hamiltonian

$$\begin{aligned} H = {} & v(\sigma_x \sin p_x + \sigma_y \sin p_y + \sigma_z \sin p_z) \\ & + t\sigma_0(\cos p_x + \cos p_y + \cos p_z) + V(\boldsymbol{r})\sigma_0 \end{aligned} \tag{4.1}$$

describes Kramers-Weyl fermions of positive chirality with momenta near $(0,0,0)$, $(\pi,\pi,0)$, $(\pi,0,\pi)$, $(0,\pi,\pi)$ and of negative chirality near (π,π,π), $(\pi,0,0)$, $(0,\pi,0)$, $(0,0,\pi)$. The Hamiltonian contains spin-independent terms, hopping terms $\propto \cos p_\alpha$ and a scalar potential V, as well as spin-orbit coupling terms $\propto \sigma_\alpha \sin p_\alpha$.

The numerical study of the spectral statistics of Kramers-Weyl fermions that prompted our investigation is shown in Fig. 4.1. A quantum dot is formed by restricting the lattice to a small region and chaotic dynamics is produced by a random potential. For $t = 0$ the level spacing distribution

is well described by the $\beta = 1$ Wigner surmise (orthogonal statistics), while the spin-orbit coupling would have suggested symplectic $\beta = 4$ statistics. Paradoxically, the $\beta = 4$ distribution requires the addition of spin-*independent* hopping.

In the next section we construct the "fake" time-reversal operation $\mathcal{T}^*$ that squares to $+1$ and is responsible for the $\beta = 1$ spacing distribution when $t = 0$. The supercell symmetry that enables $\mathcal{T}^*$ is broken by the $\cos p$ terms, which reveal the true $\mathcal{T}$, squaring to -1 with a $\beta = 4$ spacing distribution. In Sec. 4.3 we investigate how the symmetry breaking manifests itself in a transport property (the magnetoconductance). The analytical results are compared with numerical simulations in Sec. 6.A. In the concluding section we make contact with the spectrum of lattice Dirac operators on a torus, which shows a similar shift of symmetries when the number of lattice sites changes from even to odd [80, 81].

4.2 Supercell symmetry

4.2.1 Zero magnetic field

The tight-binding Hamiltonian of a spin-1/2 degree of freedom with nearest-neighbor hopping and on-site disorder on an orthorhombic lattice (lattice constants a_x, a_y, a_z) has the generic form [9]

$$\mathcal{H} = \sum_{\alpha=x,y,z} \left[t_\alpha \sigma_0 \cos a_\alpha p_\alpha + v_\alpha \sigma_\alpha \sin a_\alpha p_\alpha \right] + V(\boldsymbol{r})\sigma_0. \tag{4.2}$$

Both the spin-independent hopping energies t_α and the spin-orbit coupling amplitudes v_α may be anisotropic. We set $\hbar$ equal to unity, $p_\alpha = -i\partial/\partial x_\alpha$ is the momentum operator, the Pauli spin matrices are $\boldsymbol{\sigma} = (\sigma_x, \sigma_y, \sigma_z)$, and σ_0 is the 2×2 unit matrix.

The Hamiltonian (7.5) is constrained by the symplectic symmetry

$$\mathcal{H} = \sigma_y \mathcal{H}^* \sigma_y \equiv \mathcal{T}\mathcal{H}\mathcal{T}. \tag{4.3}$$

This is a time-reversal operation that changes the sign of both $\boldsymbol{\sigma}$ and $\boldsymbol{p} = -i\boldsymbol{\nabla}$, leaving $\mathcal{H}$ invariant. The operator $\mathcal{T} = \sigma_y \times$ complex conjugation squares to -1, thus we expect GSE statistics, while GOE statistics would require a time-reversal operator that squares to $+1$.

The eight flavors of Kramers-Weyl fermions at $p_\alpha \in \{0, \pi/a_\alpha\}$ are displaced in energy from $E = 0$ by the t_α terms. Without these terms, the Hamiltonian

$$\mathcal{H}_0 = \sum_\alpha v_\alpha \sigma_\alpha \sin a_\alpha p_\alpha + V(\boldsymbol{r})\sigma_0 \tag{4.4}$$

has the supercell symmetry[2]

$$U_y \mathcal{H}_0 U_y^\dagger = \mathcal{H}_0, \;\; U_y = \sigma_y e^{i\pi n_x + i\pi n_z}, \;\; n_\alpha = \frac{x_\alpha}{a_\alpha} \in \mathbb{Z}, \tag{4.5}$$

which transforms $p_x \to p_x + \pi/a_x$, $p_z \to p_z + \pi/a_z$, while leaving p_y unaffected. The operator U_y thus maps each Kramers-Weyl fermion onto a partner of the same chirality.

Since $U_y^2 = 1$ its eigenvalues are ± 1 and we can block-diagonalize $\mathcal{H}_0$ in sectors of the Hilbert space where $U_y \Psi = \pm \Psi$. In a given sector the time-reversal operator $\mathcal{T} = \sigma_y \times$ complex conjugation can be replaced by

$$\mathcal{T}^* = \pm \mathcal{T} U_y = \mp e^{i\pi n_x + i\pi n_z} \times \text{complex conjugation}. \tag{4.6}$$

The "fake" time-reversal operator $\mathcal{T}^*$ squares to $+1$, so each sector has an orthogonal time-reversal symmetry.

The spin-independent hopping terms in the full Hamiltonian (7.5) break the supercell symmetry if two or more of the t_α's are nonzero. (If only a single $t_\alpha \neq 0$ the symmetry $U_\alpha = \sigma_\alpha e^{i\pi \sum_{\alpha' \neq \alpha} n_{\alpha'}}$ remains unbroken.) We would thus expect a $\beta = 1$ to $\beta = 4$ transition in the level spacing distribution $P(s) \propto s^\beta$ when t becomes larger than the mean level spacing δ.

4.2.2 Nonzero magnetic field

A magnetic field B breaks time-reversal symmetry, driving both orthogonal ($\beta = 1$) and symplectic ($\beta = 4$) level spacing distributions towards the unitary ($\beta = 2$) result. The degeneracy of the $\beta = 2$ spectra is different in the two cases.

For $B = 0$ each energy level is twofold degenerate (Kramers degeneracy). In a magnetic field the degeneracy is broken for a nonzero t_α, but it remains when $t_x, t_y, t_z = 0$ if the magnetic field enters only via the substitution $\boldsymbol{p} \to \boldsymbol{p} + e\boldsymbol{A}$ — so only as an orbital effect, no Zeeman effect on the spin.

This persistent degeneracy is due to the fact that the supercell symmetry U_α is not broken by the substitution $\boldsymbol{p} \to \boldsymbol{p} + e\boldsymbol{A}$. Starting from a Hamiltonian which commutes with U_x and U_y and an energy eigenstate Ψ such that $U_y \Psi = \Psi$ we can then construct another eigenstate $\Psi' = U_x \Psi$

[2] The unitary transformation (4.5) has a periodicity of twice the lattice constant, hence the name "supercell symmetry", suggested to us by Anton Akhmerov.

at the same energy eigenvalue. The two states Ψ and Ψ' are orthogonal,

$$\begin{aligned}\langle\Psi|\Psi'\rangle &= \langle\Psi|U_x|\Psi\rangle = \langle\Psi|U_y^\dagger U_x U_y|\Psi\rangle \\ &= -\langle\Psi|U_x|\Psi\rangle = -\langle\Psi|\Psi'\rangle \Rightarrow \langle\Psi|\Psi'\rangle = 0,\end{aligned} \tag{4.7}$$

so the energy eigenvalue is twofold degenerate.

4.3 Supercell symmetry effects on the conductance

The appearance of the supercell symmetry can be probed via the electrical conductance G. In a magnetic field, the $\beta = 1 \to \beta = 2$ transition gives an increase in G (weak localization), while the $\beta = 4 \to \beta = 2$ transition gives a decrease in G (weak antilocalization). The theoretical prediction for this quantum correction $\delta G = G(B) - G(0)$ is [82]

$$\delta G = \frac{2e^2}{h} \times \begin{cases} 1/3 & \text{for } \beta = 1 \to 2, \\ -1/6 & \text{for } \beta = 4 \to 2. \end{cases} \tag{4.8}$$

This result applies to the disorder-averaged conductance in a wire geometry (length L large compared to the width W), with a large number $N \gg 1$ of propagating modes, in the diffusive regime (L much larger than the mean free path l, but much smaller than the localization length $\xi = Nl$).

An alternative way to probe the symmetry class is via the sample-to-sample fluctuations of the conductance. According to the theory of universal conductance fluctuations [83, 84], the variance $\operatorname{Var} G$ of the conductance is proportional to g^2/β, where g is the level degeneracy factor. In our case the $\beta = 1 \to \beta = 2$ transition happens at fixed $g = 2$, while the $\beta = 4 \to \beta = 2$ transition is accompanied by $g = 2 \to g = 1$, hence in both cases the magnetic field reduces the variance by a factor of two. The predicted values in a wire geometry are [82]

$$\operatorname{Var} G = \left(\frac{2e^2}{h}\right)^2 \times \begin{cases} 2/15 \to 1/15 & \text{for } \beta = 1 \to 2, \\ 1/30 \to 1/60 & \text{for } \beta = 4 \to 2. \end{cases} \tag{4.9}$$

For these quantum interference effects the crossover to $\beta = 2$ happens when the magnetic flux through the wire becomes larger than a flux quantum h/e. Which of the two transitions applies, $\beta = 1 \to \beta = 2$ or $\beta = 4 \to \beta = 2$, depends on whether the supercell symmetry breaking

term t is small or large compared to the Thouless energy $E_\mathrm{T} = (h/e^2)G\delta$. In a diffusive multimode wire $G \gg e^2/h \Rightarrow E_\mathrm{T} \gg \delta$, hence the range of t governed by the supercell symmetry is much larger for the conductance, when we need $t \ll E_\mathrm{T}$, than it is for the level repulsion, when the condition is $t \ll \delta$.

4.4 Numerical results

We have studied the effect of the supercell symmetry numerically, using the *Kwant* tight-binding package [47, 85]. For computational efficiency we took a 2D square lattice, rather than a 3D lattice, given by the Hamiltonian

$$H = v(\sigma_x \sin a_0 p_x + \sigma_y \sin a_0 p_y) + t\sigma_0(\cos a_0 p_x + \cos a_0 p_y) + V(\boldsymbol{r})\sigma_0. \tag{4.10}$$

The random potential V was chosen independently on each site, uniformly in the interval $(-V_0/2, V_0/2)$.

For the level statistics we took a square geometry,[3] on a lattice of size $200\,a_0 \times 200\,a_0$. We calculated the distribution of the nearest-neigbor spacings of the twofold degenerate levels in the interval $|E - 0.2\,v/a_0| < 4\cdot 10^{-3}\,v/a_0$ (mean level spacing $\delta = 3.56\cdot 10^{-4}\,v/a_0$, approximately constant in this energy range), averaging over some 2000 disorder realizations. Note that the disorder potential breaks chiral symmetry,[4] so there is no $\pm E$ symmetry in the spectrum.

As an extra check, we also calculated the ratio distribution [86], meaning the probability distribution $P(r)$ of the ratio $r_n = s_n/s_{n-1}$ of two consecutive level spacings $s_n = E_{n+1} - E_n$.

For the conductance we took a disordered wire of width $W = 200\,a_0$ and length $L = 1000\,a_0$. The end points are connected to heavily doped metal leads, modelled on the lattice by breaking the transverse bonds. The transmission matrix $\boldsymbol{t}$ at Fermi energy E determines the zero-temperature two-terminal conductance $G = (e^2/h)\,\mathrm{Tr}\,\boldsymbol{t}\boldsymbol{t}^\dagger$. We took $E = 0.2\,v/a_0$, when the number of propagating modes through the disordered region equals $N = 52$ (counting degeneracies). The mean free path for $V_0 = 0.5\,v/a_0$ is estimated at $l = 150\,a_0$, from the Drude formula $G \approx (Ne^2/h)(1 + L/l)^{-1}$.

[3] In all our systems we truncate the lattice without applying periodic boundary conditions. The parity of the number of lattice sites then does not matter.

[4] Chiral symmetry means that the Hamiltonian $\sigma_x \sin p_x + \sigma_y \sin p_y$ anticommutes with σ_z, enforcing a $\pm E$ symmetry in the spectrum. This symmetry plays no role in our analysis, because it is broken by the $V\sigma_0$ disorder potential.

The localization length $\xi = Nl$ is then larger than L, so we are in the diffusive regime.

Fig. 4.2 shows the transition from the $\beta = 1$ to $\beta = 4$ level spacing and ratio distributions. The transition from weak localization to weak anti-localization is shown in Fig. 4.3, as well as the transition from $\beta = 1$ to $\beta = 4$ conductance fluctuations. It is difficult to fully reach the large-N regime where the analytical results (4.8) and (4.9) apply, so the agreement analytics–numerics remains qualitative for the conductance.

In Fig. 4.4 we show that the effect of the supercell symmetry is suppressed more rapidly by the spin-independent hopping energy t if we consider the level spacings (when we need $t \gtrsim \delta$) than it is if we consider the conductance (when we need $t \gtrsim E_\mathrm{T}$). In the conductance calculations $G \approx 7e^2/h \Rightarrow E_\mathrm{T}/\delta \approx 7$, so we expect about an order of magnitude difference in the onset of the two transitions, in accord with Fig. 4.4.

4.5 Conclusion

In summary, we have identified a supercell symmetry and a resulting "fake" time-reversal symmetry operation, squaring to $+1$ rather than -1, which explains the $\beta = 1$ spectral statistics of the Kramers-Weyl Hamiltonian (6.2) in the absence of the spin-independent hopping term $\propto t \cos p$. The same symmetry is responsible for the appearance of weak localization in the magnetoconductance.

The crossover from $\beta = 1$ to $\beta = 4$ level repulsion happens quickly, when t becomes larger than the mean level spacing δ. The crossover from weak localization to weak antilocalization happens at larger t, larger by a factor of conductance $G \times h/e^2$. This delayed crossover in the magnetoconductance may make the effect of the supercell symmetry more easily observable.

A similar shift of symmetries has been observed when comparing two discretization schemes of lattice Dirac operators on a torus [80, 81]. The Dirac Hamiltonian $-i\boldsymbol{\nabla} \cdot \boldsymbol{\sigma}$ needs a special "staggered" discretization of the spatial derivative to make sure that the low-energy states are only near $\boldsymbol{p} = 0$. The "naive" discretization $\partial f/\partial x \mapsto (2a)^{-1}[f(x+a) - f(x-a)]$ introduces an additional Dirac cone at $\boldsymbol{p} = \pi/a$ (fermion doubling [88, 89]).

If one then imposes periodic boundary conditions, the naive discretization obeys the supercell symmetry (4.5) if the number of lattice sites is even but not if it is odd. The way this works out for the spectral statistics is different in Refs. [80, 81] than it is here, because of the presence of chiral

symmetry, but the mechanism is the same.

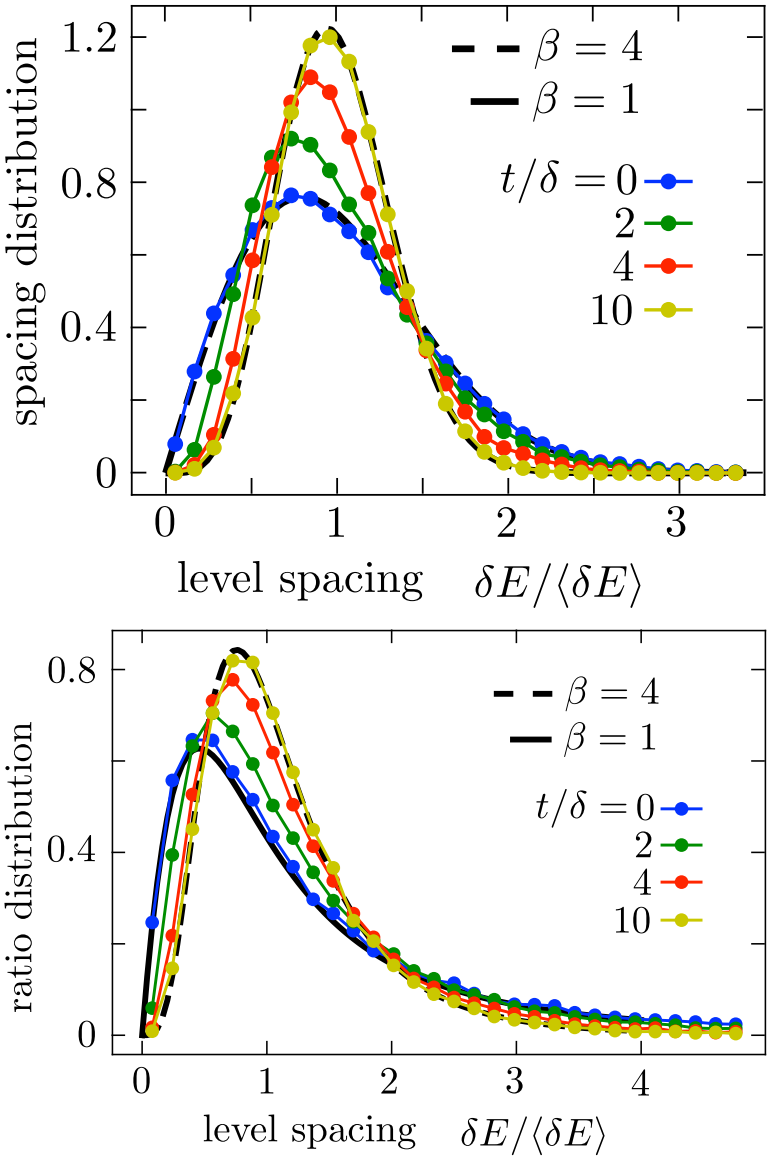

Figure 4.2: Top panel: Same as Fig. 4.1, but now for a 2D square lattice (size 200×200, disorder strength $V_0 = 0.5\, v/a_0$) and for four values of the spin-independent hopping energy t. The bottom panel shows the corresponding ratio distribution (with the $\beta = 1$ and $\beta = 4$ limits from Ref. 86).

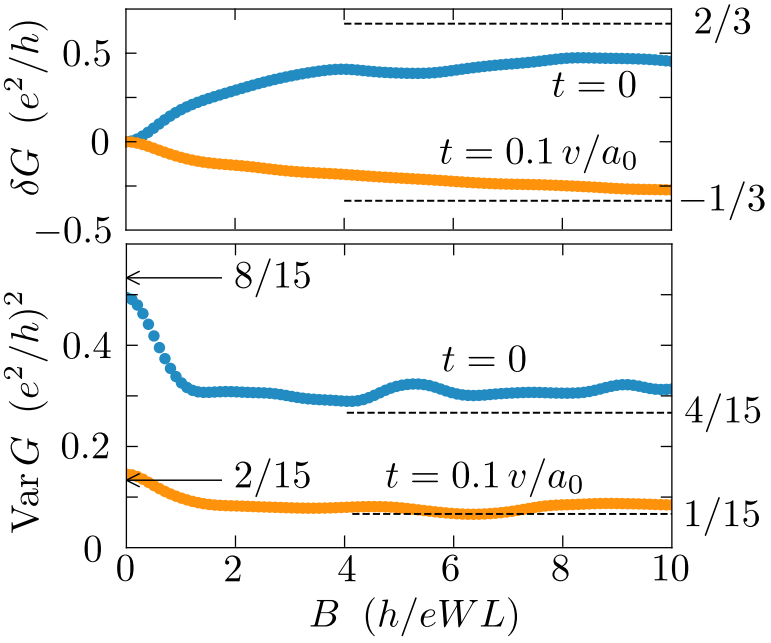

Figure 4.3: Magnetic field dependence of the conductance mean $\delta G = \langle G(B)\rangle - \langle G(0)\rangle$ (top panel) and conductance variance $\mathrm{Var}\, G = \langle G(B)^2\rangle - \langle G(B)\rangle^2$ (bottom panel), averaged over disorder in a conducting wire (length $L = 1000$, width $W = 200$, disorder strength $V_0 = 0.5\,v/a_0$, Fermi energy $E = 0.2\,v/a_0$). The blue data points are in the presence of the supercell symmetry ($t = 0$), for the gold data points the symmetry is broken ($t = 0.1\,v/a_0$). The arrows and dashed lines indicate the analytical predictions (4.8) and (4.9) in the limit $N \to \infty$.

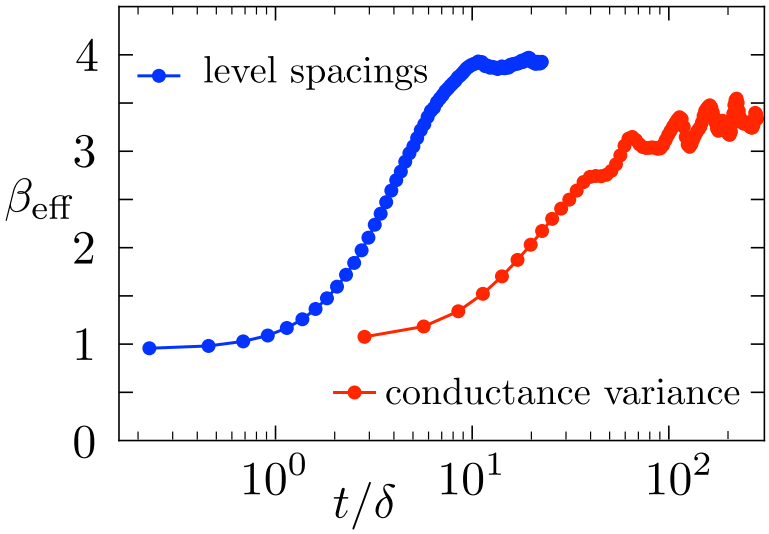

Figure 4.4: Transition from $\beta = 1$ to $\beta = 4$ with increasing spin-independent hopping energy t, as measured via the level spacing distribution (red data points, same parameters as in Fig. 4.2) or via the variance of the conductance (blue data points, same parameters as in Fig. 4.3, at $B = 0$). The transition is quantified by an effective parameter β_{eff}. For the conductance this is defined by $\beta_{\text{eff}} = \frac{8}{15}(e^2/h)^2(\text{Var}\, G)^{-1}$. For the level spacing we fitted the data to the Wigner surmise interpolation [87] $P(s) = cs^{\beta_{\text{eff}}} \exp(-c's^2)$, with $s = \delta E/\delta$ and coefficients c, c' such that the zeroth and first moments of $P(s)$ are equal to unity.

5 Chiral charge transfer along magnetic field lines in a Weyl superconductor

5.1 Introduction

Three-dimensional Weyl fermions have a definite chirality, given by the $\pm$ sign in the Weyl Hamiltonian $\pm \boldsymbol{p} \cdot \boldsymbol{\sigma}$. Three spatial dimensions are essential, if $\boldsymbol{p} \cdot \boldsymbol{\sigma} = p_x \sigma_x + p_y \sigma_y$ contains only two Pauli matrices, then $+\boldsymbol{p} \cdot \boldsymbol{\sigma}$ and $-\boldsymbol{p} \cdot \boldsymbol{\sigma}$ can be transformed into each other by a unitary transformation (conjugation with σ_z). The chirality is therefore a characteristic feature of 3D Weyl semimetals, not shared by 2D graphene.

The search for observable signatures of chirality is a common theme in the study of this new class of materials [13, 66, 90, 91]. The basic mechanism used for that purpose is the chirality dependent motion in a magnetic field: Weyl fermions in the zeroth Landau level propagate parallel or antiparallel to the field lines, dependent on their chirality [92]. A population imbalance between the two chiralities then produces the chiral magnetic effect [93, 94]: An electrical current along the field lines, which changes sign if the field is inverted.

Here we present a novel, albeit less dramatic, signature of chirality: An electrical conductance which depends on the magnetic field direction. The effect appears if superconductivity is induced in a magnetic topological insulator, in the layered geometry of Meng and Balents [6] (see Fig. 7.1). The superconductor cannot gap out the Weyl points of opposite chirality, provided that the induced pair potential Δ_0 remains smaller than the magnetization energy β. The main effect of the superconductor is to renormalize the charge of the quasiparticles [95], by a factor $\kappa = \sqrt{1 - \Delta_0^2/\beta^2}$.

A magnetic field B perpendicular to the layers penetrates in an array of $h/2e$ vortices. The zeroth Landau level is a dispersionless flat band in the plane of the layers — the chirality of the Weyl fermions prevents broadening of the Landau band by vortex scattering [96].

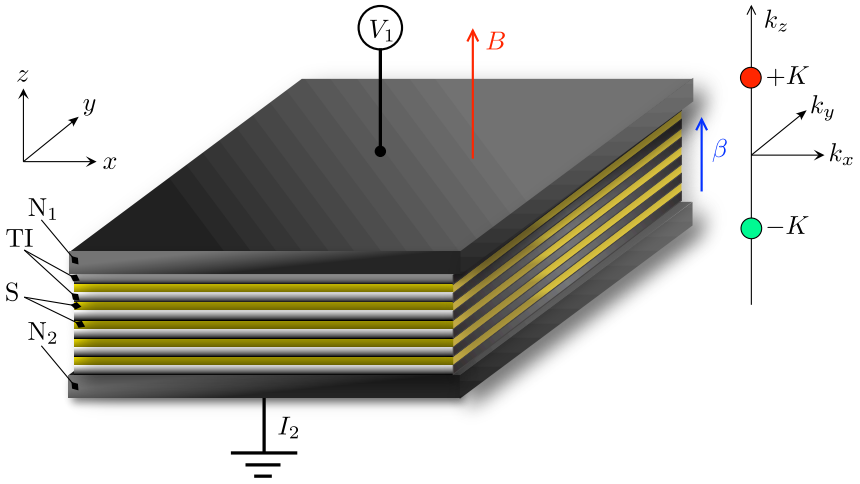

Figure 5.1: Left panel: Weyl superconductor formed by alternating layers of magnetic topological insulator (TI, magnetization β) and s-wave superconductor (S, pair potential Δ_0, chemical potential μ), between normal-metal contacts (N_1 and N_2. A magnetic field B perpendicular to the layers (along z) produces a Landau band that is dispersionless in the x–y plane, with free propagation in the z-direction. Right panel: Weyl points of opposite chirality at $k_z = \pm K$. For $\mu \neq 0$ the conductance $G = I_2/V_1$ depends on whether the magnetic field points parallel or antiparallel to the vector from $-K$ to $+K$.

Following Ref. 97 we probe the Landau band by electrical conduction: A voltage V_1 applied to contact N_1 induces a current $I_2 = GV_1$ in contact N_2. This is a three-terminal circuit, the grounded superconductor being the third terminal. The chemical potential μ_N in the normal-metal contacts is assumed to be large compared to the value μ in the superconductor. We calculate the dependence of the conductance $G(\pm B)$ on the direction of the magnetic field B, relative to the separation of the Weyl points of opposite chirality.

When the chemical potential is at the Weyl point ($\mu = 0$) the conductance is determined by the renormalized charge and B only enters via the Landau band degeneracy [97],

$$G = \kappa^2 G_0, \quad G_0 = (e^2/h)N_\Phi, \quad \text{at} \quad \mu = 0, \tag{5.1}$$

with $N_\Phi = eBS/h$ the flux through an area S in units of h/e. We generalize this result to nonzero μ and find that

$$\delta G = G(B) - G(-B) = (4\mu/\beta)(\kappa^2 - \kappa)G_0. \tag{5.2}$$

The conductance thus depends on whether the magnetic field points from + chirality to − chirality, or the other way around.

The outline of the chapter is as follows. In the next section we formulate the problem of electrical conduction along the magnetic vortices of a Weyl superconductor. The key quantity to calculate is the charge e^* transferred by the quasiparticles across the normal-superconductor interface. At $\mu = 0$ this is simply given by the renormalized charge κe of the Weyl fermions [97], but that no longer holds at nonzero μ. In Secs. 5.3 and 5.4 we apply a mode matching technique developed in Ref. 98 to calculate e^*. The conductance then follows in Sec. 5.5. These are all analytical results, we test them on a computer simulation of a tight-binding model in Sec. 6.A. We conclude in Sec. 7.6.

5.2 Weyl superconductor in a magnetic vortex lattice

We consider a three-dimensional Weyl superconductor [6] (Fermi velocity $v_{\rm F}$, chemical potential μ, s-wave pair potential $\Delta_0 e^{i\phi}$), sandwiched between metal contacts $\rm N_1$ and $\rm N_2$ at $z = \pm L/2$ (see Fig. 7.1). A magnetic field $B > 0$ in the z-direction penetrates the superconductor in the form of a vortex lattice. The superconducting phase ϕ winds by 2π around each vortex (at position $\boldsymbol{R}_n$),

$$\nabla \times \nabla\phi = 2\pi\hat{z}\sum_n \delta(\boldsymbol{r} - \boldsymbol{R}_n). \tag{5.3}$$

The Bogoliubov-De Gennes Hamiltonian is

$$\begin{aligned}\mathcal{H} = {} & v_{\rm F}\nu_z\tau_z(\boldsymbol{k}\cdot\boldsymbol{\sigma}) - ev_{\rm F}\nu_0\tau_z(\boldsymbol{A}\cdot\boldsymbol{\sigma}) + \nu_0\tau_0\boldsymbol{\beta}\cdot\boldsymbol{\sigma} \\ & - \mu\nu_z\tau_0\sigma_0 + \Delta_0(\nu_x\cos\phi - \nu_y\sin\phi)\tau_0\sigma_0.\end{aligned} \tag{5.4}$$

The Pauli matrices $\sigma_\alpha, \tau_\alpha, \nu_\alpha$ act respectively on the spin, subband, and electron-hole degree of freedom. We set $\hbar$ to unity and choose the electron charge as $+e$. The magnetization $\boldsymbol{\beta} = \beta\boldsymbol{n}_\beta$ (with $\boldsymbol{n}_\beta$ a unit vector) may point in an arbitary direction relative to $\boldsymbol{B} = \nabla\times\boldsymbol{A} = B\hat{z}$. We choose a gauge in which $A_z = 0$ and both $\boldsymbol{A}$ and ϕ are z-independent.

The Weyl points in zero magnetic field are at momentum $\boldsymbol{k} = \pm\boldsymbol{K} = \pm K\boldsymbol{n}_\beta$ with

$$v_{\rm F}K = \kappa\beta, \quad \kappa = \sqrt{1 - \Delta_0^2/\beta^2}. \tag{5.5}$$

The Weyl cones remain gapless provided that $\Delta_0 < \beta$. In a magnetic field the states condense into Landau bands, dispersionless in the plane perpendicular to $\boldsymbol{B}$, but freely moving along $\boldsymbol{B}$.

A quasiparticle in a Landau band, at energy E, has charge expectation value $Q = -e\partial E/\partial\mu$. At the Weyl point, $\mu = 0 = E$, this equals [95]

$$Q_0 = \kappa e = e\sqrt{1 - \Delta_0^2/\beta^2}. \tag{5.6}$$

We seek the charge e^* transferred into the normal-metal contact by a quasiparticle in the Landau band. At $\mu = 0$ this was calculated in Ref. 97, with the result $e^* = Q_0$. We wish to generalize this to nonzero μ. For that purpose we apply a methodology developed for a different problem in Ref. 98, as described in the next section.

5.3 Fractional charge transfer

5.3.1 Matching condition

The particle current operator $\hat{v}_z$ and charge current operator $\hat{j}_z$, both in the z-direction, are given by

$$\begin{aligned} \hat{v}_z &= \partial\mathcal{H}/\partial k_z = v_{\mathrm{F}}\nu_z\tau_z\sigma_z, \\ \hat{j}_z &= -\partial\mathcal{H}/\partial A_z = ev_{\mathrm{F}}\nu_0\tau_z\sigma_z. \end{aligned} \tag{5.7}$$

In what follows we set v_{F} and e equal to unity, for ease of notation.

The chirality $\chi = \pm 1$ of a mode in the superconductor (S) determines whether it propagates in the $+z$ direction or in the $-z$ direction. We position the normal-superconductor (NS) interface at $z = 0$, so that the mode in S approaches it from $z < 0$ for $\chi = +1$ and from $z > 0$ for $\chi = -1$.

We assume that the chemical potential μ_{N} in N is large compared to the value μ in S. The potential step at the NS interface boosts the momentum component k_z perpendicular to the interface, without affecting the parallel components k_x, k_y, so in N only modes are excited with $|k_z| \gg |k_x|, |k_y|$. These are eigenstates of $\nu_z\tau_z\sigma_z$ with eigenvalue χ, moving away from the interface in the $+z$ direction if $\chi = +1$ and in the $-z$ direction for $\chi = -1$. Continuity of the wave function Ψ at the interface then gives the matching condition

$$\nu_z\tau_z\sigma_z\Psi = \chi\Psi \ \text{ at } \ z = 0. \tag{5.8}$$

5.3.2 Projection

Because the Hamiltonian (7.5) commutes with τ_z we can replace this Pauli matrix by the subband index $\tau = \pm 1$ and rewrite the matching condition (5.8) as $\chi\tau\nu_z\sigma_z\Psi = \Psi$. We define the projection operator

$$\mathcal{P} = \tfrac{1}{2}(1 + \chi\tau\nu_z\sigma_z), \text{ such that } \mathcal{P}\Psi = \Psi \text{ at } z = 0, \tag{5.9}$$

and project the Hamiltonian (7.5),

$$\mathcal{P}\mathcal{H}\mathcal{P} = (\tau\beta_z - \chi\mu)\mathcal{P}\hat{j}_z\mathcal{P} + \mathcal{P}\hat{k}_z\hat{v}_z\mathcal{P}. \tag{5.10}$$

We have used that $\boldsymbol{A}$ only has components in the x–y plane. The hat on $\hat{k}_z = -i\partial/\partial z$ is there to remind us it is an operator.

We take the z-dependent inner product

$$\langle\Psi_1|\Psi_2\rangle_z = \int dx \int dy\, \Psi_2^*(x,y,z)\Psi_2(x,y,z) \tag{5.11}$$

of Eq. (5.10),

$$\begin{aligned} &(\tau\beta_z - \chi\mu)\langle\Psi|\mathcal{P}\hat{j}_z\mathcal{P}|\Psi\rangle_z = \langle\Psi|\mathcal{P}\delta\mathcal{H}\mathcal{P}|\Psi\rangle_z, \\ &\text{with } \delta\mathcal{H} = \mathcal{H} - \hat{k}_z\hat{v}_z. \end{aligned} \tag{5.12}$$

At the NS interface $z = 0$ the projector may be removed,

$$(\tau\beta_z - \chi\mu)\langle\Psi|\hat{j}_z|\Psi\rangle_0 = \langle\Psi|\delta\mathcal{H}|\Psi\rangle_0, \tag{5.13}$$

since neither $\hat{j}_z$ nor $\delta\mathcal{H}$ contain a z-derivative, so that these operators commute with the limit $z \to 0$ and we may replace $\mathcal{P}\Psi$ by Ψ in view of the matching condition (5.9). Eq. (5.13) is the key identity that allows us to calculate the transferred charge.

5.3.3 Transferred charge

Let Ψ be an eigenstate of $\mathcal{H}$ at energy E. The transferred charge e^* through the NS interface is given by the ratio

$$e^* = \frac{\langle\Psi|\hat{j}_z|\Psi\rangle_0}{\langle\Psi|\hat{v}_z|\Psi\rangle_0}. \tag{5.14}$$

Substitution of Eq. (5.13) equates this to

$$e^* = (\tau\beta_z - \chi\mu)^{-1}\frac{\langle\Psi|\mathcal{H} - \hat{k}_z\hat{v}_z|\Psi\rangle_0}{\langle\Psi|\hat{v}_z|\Psi\rangle_0} \tag{5.15a}$$

$$= (\tau\beta_z - \chi\mu)^{-1}\left(\chi E - \frac{\langle\Psi|\hat{k}_z\hat{v}_z|\Psi\rangle_0}{\langle\Psi|\hat{v}_z|\Psi\rangle_0}\right). \tag{5.15b}$$

The term χE appears because

$$\langle\Psi|\mathcal{H}|\Psi\rangle_0 = E\langle\Psi|\Psi\rangle_0 = \chi E\langle\Psi|\hat{v}_z|\Psi\rangle_0, \tag{5.16}$$

where in the last equality we used the matching condition (5.8).

Particle current conservation requires that

$$\frac{d}{dz}\langle\Psi|\hat{v}_z|\Psi\rangle_z = 0. \tag{5.17}$$

More generally, for our case of a z-independent Hamiltonian it holds that

$$\frac{d}{dz}\langle\Psi|f(\hat{k}_z)\hat{v}_z|\Psi\rangle_z = 0 \tag{5.18}$$

for any function of f of $\hat{k}_z$ (see App. 5.A for a proof). Each of the two expectation values $\langle\cdots\rangle_0$ on the right-hand-side of Eq. (5.15b) can thus be replaced by $\langle\cdots\rangle_z$. This ratio can then be evaluated for large $|z|$, far from the NS interface, where evanescent waves have decayed and $\Psi \propto e^{ik_z z}$ is an eigenstate of $\hat{k}_z$.

We finally obtain the transferred charge

$$e^* = e\frac{\chi E - v_\mathrm{F} k_z}{\tau\beta_z - \chi\mu}, \tag{5.19}$$

reinstating units of e and v_F. For $\mu = 0 = E$, $\beta = \beta_z$, $k_z = K = \kappa\beta/v_\mathrm{F}$ we recover the result $e^* = \pm\kappa e = \pm Q_0$ of Ref. 97.

It remains to relate the momentum k_z of a propagating mode at the Fermi level to the parameters of the Weyl superconductor. For that we need the dispersion relation $E(k_z)$ of the Landau band, which we calculate in the next section.

5.4 Dispersion relation of the Landau band

5.4.1 Block diagonalization

We calculate the dispersion relation of the Landau band by means of the block diagonalization approach of Ref. 96. Starting from the BdG Hamiltonian (7.5) we first make the Anderson gauge transformation [99]

$$\mathcal{H} \mapsto \Omega^\dagger\mathcal{H}\Omega, \quad \text{with } \Omega = \begin{pmatrix} e^{i\phi} & 0 \\ 0 & 1 \end{pmatrix}. \tag{5.20}$$

The subblocks of Ω refer to the electron-hole (ν_α) degree of freedom. The resulting Hamiltonian is

$$\begin{aligned}\mathcal{H} &= \nu_z\tau_z(\boldsymbol{k}+\boldsymbol{a})\cdot\boldsymbol{\sigma} + \nu_0\tau_z\boldsymbol{q}\cdot\boldsymbol{\sigma} + \nu_0\tau_0\boldsymbol{\beta}\cdot\boldsymbol{\sigma} \\ &\quad - \mu\nu_z\tau_0\sigma_0 + \Delta_0\nu_x\tau_0\sigma_0, \qquad (5.21)\\ \boldsymbol{a} &= \tfrac{1}{2}\nabla\phi, \quad \boldsymbol{q} = \tfrac{1}{2}\nabla\phi - \boldsymbol{A}. \qquad (5.22)\end{aligned}$$

Both fields $\boldsymbol{a}$ and $\boldsymbol{q}$ have only components in the x–y plane and are z-independent.

To focus on states near $\boldsymbol{K}$ we set $\boldsymbol{k} = \kappa\boldsymbol{\beta} + \delta\boldsymbol{k}$ and consider $\delta\boldsymbol{k}$ small. The component parallel to $\boldsymbol{\beta}$ of a vector $\boldsymbol{v}$ is denoted by $v_\parallel = \boldsymbol{v}\cdot\boldsymbol{n}_\beta$.

One more unitary transformation $\mathcal{H} \mapsto U^\dagger\mathcal{H}U$ with

$$\begin{aligned}&U = \sigma_\parallel \exp\bigl(\tfrac{1}{2}i\alpha\nu_y\tau_z\sigma_\parallel\bigr),\\ &\tan\alpha = -\frac{\Delta_0}{K}, \quad \cos\alpha = -(1+\Delta_0^2/K^2)^{-1/2} = -\kappa,\end{aligned} \qquad (5.23)$$

followed by a projection onto the $\nu = \tau = \pm 1$ blocks, gives a pair of 2×2 low-energy Hamiltonians,

$$\begin{aligned}H_\tau &= \tau\kappa\mu\sigma_0 - (\delta\boldsymbol{k} + \boldsymbol{a} - \tau\kappa\boldsymbol{q})\cdot\boldsymbol{\sigma} \\ &\quad + (1-\kappa)(\delta k_\parallel + a_\parallel + \tau q_\parallel)\sigma_\parallel. \qquad (5.24)\end{aligned}$$

Eq. (5.24) is an anisotropic Dirac Hamiltonian, the velocity parallel to the magnetization is reduced by a factor κ. The same factor renormalizes the quasiparticle charge,

$$Q = -e\frac{\partial H_\tau}{\partial\mu} = -e\tau\kappa. \qquad (5.25)$$

The two Hamiltonians $H_\tau = H_\pm$ near $\boldsymbol{k} = \boldsymbol{K}$ thus describe quasiparticles of opposite charge. Another pair of oppositely charged Weyl cones exists near $\boldsymbol{k} = -\boldsymbol{K}$.

If $\boldsymbol{\beta} = (\beta\sin\theta, 0, \beta\cos\theta)$ makes an angle θ with the magnetic field we have

$$\begin{aligned}H_\tau &= \tau\kappa\mu\sigma_0 - \sum_{\alpha=x,y}(\delta k_\alpha + a_\alpha - \tau\kappa q_\alpha)\sigma_\alpha - \delta k_z\sigma_z \\ &\quad + (1-\kappa)(\delta k_x\sin\theta + \delta k_z\cos\theta + a_x\sin\theta + \tau q_x\sin\theta)(\sigma_x\sin\theta + \sigma_z\cos\theta),\end{aligned} \qquad (5.26)$$

where we used that $a_z = 0 = q_z$.

5.4.2 Zeroth Landau band

A major simplification appears if the magnetization $\boldsymbol{\beta}$ and the magnetic field $\boldsymbol{B}$ are either parallel or perpendicular, so $\cos\theta \equiv \gamma \in \{0, \pm 1\}$. In these cases the Hamiltonian (5.26) anticommutes with σ_z when $\mu = 0 = \delta k_z$. This socalled chiral symmetry implies that the zeroth Landau band is an eigenstate of σ_z, with eigenvalue $-\tau$ [96]. The dispersion relation then follows immediately,

$$\begin{aligned} E(k_z) &= \tau\kappa\mu + \tau\delta k_z[1-(1-\kappa)\gamma^2] \\ &= \chi\kappa\mu + \chi(k_z - \kappa\beta\gamma)[1-(1-\kappa)\gamma^2]. \end{aligned} \tag{5.27}$$

In the second equation we have identified the chirality index $\chi \equiv \text{sign}\,(dE/dk_z) = \tau$.

Equating $E(k_z) = E$ and solving for k_z gives

$$k_z = \kappa\beta\gamma - \frac{\kappa\mu - \chi E}{1-(1-\kappa)\gamma^2}, \tag{5.28}$$

to first order in E and μ. (Higher order terms are not captured by the linearization around the Weyl point.)

We substitute Eq. (5.28) in the expression (5.19) for the transferred charge,

$$e^* = \frac{\chi e}{\mu - \beta\gamma}\left(\kappa\beta\gamma - \frac{\kappa\mu - \chi E}{1-(1-\kappa)\gamma^2} - \chi E\right). \tag{5.29}$$

For $\boldsymbol{\beta} \parallel \boldsymbol{B}$ this gives

$$e^* = -\chi e\,\frac{\pm\kappa\beta - \mu + \chi E(1/\kappa - 1)}{\pm\beta - \mu}, \quad \gamma = \pm 1. \tag{5.30}$$

In contrast, for $\boldsymbol{\beta} \perp \boldsymbol{B}$ the μ and E dependence drops out,

$$e^* = -\chi\kappa e, \quad \gamma = 0. \tag{5.31}$$

These are the results for the charge transferred by a mode with k_z near $+K$. The mode with k_z near $-K$ is its charge-conjugate, the transferred charge is given by $e^*(E) \mapsto -e^*(-E)$.

5.4.3 Comparison of transferred charge and charge expectation value

For the case $\chi = 1$ that $\boldsymbol{\beta}$ is parallel to $\boldsymbol{B}$ we can use the more accurate dispersion relation from Ref. 96, without making the linearization around

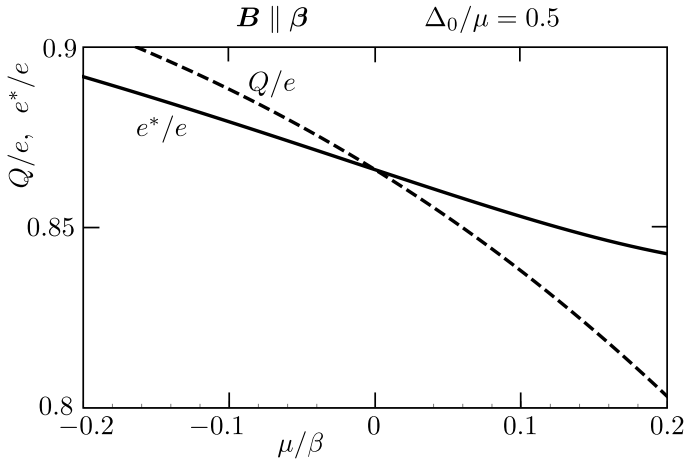

Figure 5.2: Comparison of the transferred charge e^* across the NS interface and the charge expectation value Q of the Weyl fermions. The curves are computed from Eqs. (5.33) and (5.36a) using k_0 from the full nonlinear dispersion (5.32).

the Weyl point:

$$E(k_z) = -\chi M(k_z) - \chi M'(k_z)\mu, \quad M(k_z) = \beta - \sqrt{\Delta_0^2 + k_z^2}. \tag{5.32}$$

The solution $k_z = k_0(\mu)$ of the equation $E(k_z) = 0$ then gives the transferred charge at the Fermi level ($E = 0$) via

$$e^* = -\chi e \frac{k_0(\mu)}{\beta - \mu}. \tag{5.33}$$

As a check for the linearization, to first order we find

$$k_0(\mu) = \sqrt{\beta^2 - \Delta_0^2} - \mu + \mathcal{O}(\mu^2), \tag{5.34}$$

in agreement with Eq. (5.28) for $E = 0$, $\gamma = 1$. We checked that higher order terms are relatively insignificant for $|\mu/\beta| \lesssim 0.1$.

The resulting transferred charge

$$e^* = -\chi e\kappa\big[1 + (\mu/\beta)(1 - 1/\kappa) + \mathcal{O}(\mu^2)\big] \tag{5.35}$$

can be compared with the charge expectation value

$$Q = \chi e M'(k_0) = -\frac{\chi e k_0}{\sqrt{\Delta_0^2 + k_0^2}} \tag{5.36a}$$

$$= -\chi e\kappa\big[1 + (\mu/\beta)(\kappa - 1/\kappa) + \mathcal{O}(\mu^2)\big], \tag{5.36b}$$

see Fig. 6.4. We conclude that the μ-dependence of the transferred charge e^* is not simply accounted for by the μ-dependence of the charge expectation value Q.

5.5 Conductance

5.5.1 Transmission matrix

The Landau band contains $N_\Phi = eBS/h$ modes propagating along the magnetic field through a cross-sectional area S. For each of these modes the transmission matrix $t(E)$ at energy E from contact N_1 to N_2 is a rank-two matrix of the form

$$t(E) = e^{ik_z L}|\Psi_2^+\rangle\langle\Psi_1^+| + e^{-ik_z L}|\Psi_2^-\rangle\langle\Psi_1^-|. \tag{5.37}$$

The incoming mode $|\Psi_1^\pm\rangle$ from contact N_1 is matched in S to a Landau band mode at $\pm k_z$. This chiral mode propagates over a distance L to contact N_2, picking up a phase $e^{\pm ik_z L}$, and is then matched to an outgoing mode $|\Psi_2^\pm\rangle$. The matching condition gives a charge $\pm e^*(\pm E)$ to $\Psi_n^\pm$,

$$\langle\Psi_n^\pm|\nu_z|\Psi_n^\pm\rangle = \pm e^*(\pm E). \tag{5.38}$$

The transmission matrix $t(E)$ has electron and hole submatrices t_{ee} and t_{he} (transmission of an electron as an electron or as a hole). These determine the differential conductance

$$\begin{aligned}\frac{dI_2}{dV_1} &= G_0 \lim_{E\to eV_1} \mathrm{Tr}\left(t_{ee}^\dagger t_{ee} - t_{he}^\dagger t_{he}\right)\\ &= \tfrac{1}{2}G_0\,\mathrm{Tr}\,(1+\nu_z)t^\dagger(eV_1)\nu_z t(eV_1),\end{aligned} \tag{5.39}$$

with $G_0 = N_\Phi e^2/h$.

5.5.2 Linear response

The linear response conductance $G = \lim_{V_1\to 0} dI_2/dV_1$ simplifies because at the Fermi level we can use the particle-hole symmetry relations

$$\left.\begin{aligned}&\nu_y\sigma_y t\nu_y\sigma_y = t^*\\ &|\Psi_n^+\rangle = \nu_y\sigma_y|\Psi_n^-\rangle^*\end{aligned}\right\} \text{ at } E=0. \tag{5.40}$$

These two relations imply that

$$\left.\begin{aligned}&\mathrm{Tr}\,t^\dagger\nu_z t = 0\\ &\langle\Psi_n^+|\nu_z|\Psi_n^-\rangle = 0\end{aligned}\right\} \text{ at } E=0. \tag{5.41}$$

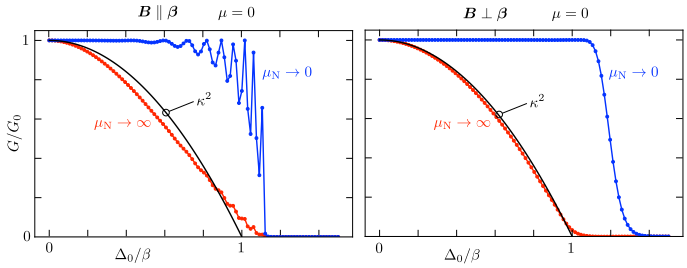

Figure 5.3: Dependence of the conductance G on the pair potential Δ_0, computed from the tight-binding model for $\boldsymbol{B}$ parallel to $\boldsymbol{\beta}$ (left panel) and for $\boldsymbol{B}$ perpendicular to $\boldsymbol{\beta}$ (right panel). The parameters are $d_0 = 18\,a_0$, $L = 30\,a_0$, and $\mu = 0$ (so there is no difference between parallel or antiparallel orientation of $\boldsymbol{B}$). The red and blue curves show the results with and without a large potential step at the NS interfaces. The black curve is the $\mu = 0$ result $G = \kappa^2 G_0$ from Ref. 97.

The equation (5.39) for the differential conductance thus reduces in linear response to

$$\begin{aligned} G &= \tfrac{1}{2} G_0 \,\mathrm{Tr}\, \nu_z t^\dagger \nu_z t \\ &= \tfrac{1}{2} G_0 \sum_{s=\pm} \langle \Psi_2^s | \nu_z | \Psi_2^s \rangle \langle \Psi_1^s | \nu_z | \Psi_1^s \rangle = N_\Phi \frac{(e^*)^2}{h}. \end{aligned} \tag{5.42}$$

The charge $e \mapsto e^*$ *quadratically* renormalizes the conductance [97].

Application of Eq. (5.29) at $E = 0$ then gives the result

$$G/G_0 = \begin{cases} \kappa^2 \pm (2\mu/\beta)(\kappa^2 - \kappa) & \text{if } \boldsymbol{\beta} \parallel \boldsymbol{B}, \\ \kappa^2 & \text{if } \boldsymbol{\beta} \perp \boldsymbol{B}, \end{cases} \tag{5.43}$$

to first order in μ. The $\pm$ sign refers to $\boldsymbol{\beta}$ parallel $(+)$ or antiparallel $(-)$ to $\boldsymbol{B}$. The difference $\delta G = G(B) - G(-B)$ is thus given by the formula (5.2) announced in the introduction.

5.6 Numerical results

To test these analytical results, we have calculated the conductance numerically from a tight-binding model obtained by discretizing the Hamiltonian (7.5) of the Weyl superconductor on a cubic lattice (lattice constant

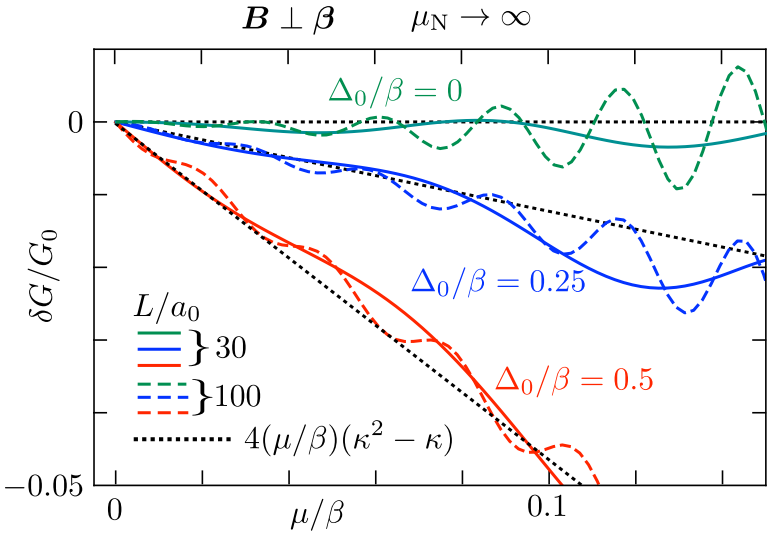

Figure 5.4: Dependence of the conductance on the orientation of $\boldsymbol{B}$, when it is perpendicular to $\boldsymbol{\beta}$ and there is a large potential step at the NS interfaces (limit $\mu_N \to \infty$). The colored curves show $\delta G = G(B) - G(-B)$ as a function of μ, computed from the tight-binding model ($d_0 = 18\,a_0$, three values of Δ_0/β, two values of L). The black dotted line is the linear μ-dependence following from Eq. (5.43).

a_0):

$$\begin{aligned} H_S = (v_F/a_0)\tau_z \sum_{\alpha=x,y,z} \sigma_\alpha \sin(a_0\nu_z k_\alpha - e a_0 \nu_0 A_\alpha) \\ + \nu_0\tau_0 \boldsymbol{\beta}\cdot\boldsymbol{\sigma} - \mu\nu_z\tau_0\sigma_0 \\ + \Delta_0(\nu_x\cos\phi - \nu_y \sin\phi)\tau_0\sigma_0 \\ + (v_F/a_0)\nu_z\tau_x\sigma_0 \sum_{\alpha=x,y,z} (1 - \cos a_0 k_\alpha). \end{aligned} \tag{5.44}$$

The term on the last line is added to avoid fermion doubling.

The vortex lattice (a square array with lattice constant d_0 and two $h/2e$ vortices per unit cell) is introduced as described in Ref. 96. The scattering matrix is calculated using the Kwant code [47], and then the linear-response conductance follows from

$$G = \frac{I_2}{V_1} = \frac{e^2}{h} \operatorname{Tr}\,(t_{ee}^\dagger t_{ee} - t_{he}^\dagger t_{he}), \tag{5.45}$$

where the trace is taken over all the N_Φ modes in the magnetic Brillouin zone and the transmission matrices are evaluated at the Fermi level ($E = 0$).

In Fig. 5.3 we compare the conductance with and without a potential step at the NS interfaces. In the absence of a potential step, when the Hamiltonian H_N in N equals H_S with $\Delta_0 = 0$, the conductance has the bare value of $G_0 = N_\Phi e^2/h$, as long as Δ_0 remains well below β. When Δ_0 exceeds β a gap opens up at the Weyl point and the three-terminal conductance G vanishes: All the carriers injected into the superconductor by contact N_1 are then drained to ground before they reach contact N_2.

The theory developed here does not apply to this case $\mu_\mathrm{N} = \mu$, but instead addresses the more realistic case $\mu_\mathrm{N} \gg \mu$ of a large potential step at the NS interfaces. In the numerics we implement the large-μ_N limit by removing the transverse hoppings from the tight-binding Hamiltonian in the normal-metal leads, which is then given by

$$\begin{aligned} H_\mathrm{N} = {} & (v_\mathrm{F}/a_0)\nu_z\tau_z\sigma_z \sin a_0 k_z + \nu_0\tau_0 \boldsymbol{\beta}\cdot\boldsymbol{\sigma} \\ & + (v_\mathrm{F}/a_0)\nu_z\tau_x\sigma_0(1-\cos a_0 k_z). \end{aligned} \tag{5.46}$$

As shown in the same Fig. 5.3, in that case the conductance at $\mu = 0$ follows the predicted $\kappa^2 = 1-\Delta_0^2/\beta^2$ parabolic profile [97]. The agreement is better for $\boldsymbol{B}$ perpendicular to $\boldsymbol{\beta}$ than it is for $\boldsymbol{B}$ parallel to $\boldsymbol{\beta}$.

Fig. 5.4 is the test of our key result, the difference (5.2) of the conductance for $\boldsymbol{B}$ parallel or antiparallel to $\boldsymbol{\beta}$. The linear μ-dependence has the predicted slope, without any adjustable parameter. Backscattering from the NS interfaces produces Fabry-Perot-type oscillations around this linear dependence, more rapidly oscillating when the separation L of the NS interfaces is larger (compare dashed and solid curves).

5.7 Conclusion

In summary, we have calculated the charge e^* that Weyl fermions in a superconducting vortex lattice transport into a normal-metal contact. When the chemical potential μ in the superconductor is at the Weyl point, the transferred charge equals the charge expectation value Q_0 of the Weyl fermions [97] (in the limit of a large chemical potential μ_N in the metal contacts). There is then no dependence on the relative orientation of the magnetic field $\boldsymbol{B}$ and the separation vector $\boldsymbol{\beta}$ of the Weyl points of opposite chirality. But when $\mu \neq 0$ a dependence on $\boldsymbol{B}\cdot\boldsymbol{\beta}$ appears.

This signature of chirality shows up in the conductance, which differs if $\boldsymbol{B}$ is parallel or antiparallel to $\boldsymbol{\beta}$. It is not a large effect, a few percent

(see Fig. 5.4), but since it is specifically tied to the sign of the magnetic field it should stand out from other confounding effects.

We have taken a simple layered model for a Weyl superconductor [6], to have a definite form for the pair potential. We expect the effect to be generic for Weyl semimetals in which superconductivity is intrinsic rather than induced [7, 100]. We also expect the effect to be robust to long-range disorder scattering, in view of the chirality of the motion along the magnetic field lines (backscattering needs to couple states at $\pm K$).

Appendices

5.A Derivation of Eq. (5.18)

We wish to show that the derivative

$$\begin{aligned}\frac{d}{dz}&\langle\Psi|f(\hat{k}_z)\hat{v}_z|\Psi\rangle_z \\ &= \langle\Psi|f(\hat{k}_z)\hat{v}_z\partial_z\Psi\rangle_z + \langle\partial_z\Psi|f(\hat{k}_z)\hat{v}_z\Psi\rangle_z \\ &= i\langle\Psi|f(\hat{k}_z)\hat{k}_z\hat{v}_z\Psi\rangle_z - i\langle\hat{k}_z\hat{v}_z\Psi|f(\hat{k}_z)\Psi\rangle_z \end{aligned} \tag{5.47}$$

vanishes for any function $f(\hat{k}_z)$ of $\hat{k}_z = -i\partial/\partial z$.

We rewrite

$$\hat{k}_z\hat{v}_z\Psi = (\mathcal{H} - \delta\mathcal{H})\Psi = (E - \delta\mathcal{H})\Psi \tag{5.48}$$

and use firstly that

$$\langle\Psi_1|\delta\mathcal{H}\Psi_2\rangle_z = \langle\delta\mathcal{H}\Psi_1|\Psi_2\rangle_z, \tag{5.49}$$

because $\delta\mathcal{H}$ does not contain any z-derivatives, and secondly that

$$[f(\hat{k}_z), \delta\mathcal{H}] = 0, \tag{5.50}$$

because $\delta\mathcal{H}$ does not depend on z. This gives the sequence of identities

$$\begin{aligned}\langle\Psi|f(\hat{k}_z)\hat{k}_z\hat{v}_z\Psi\rangle_z &= \langle\Psi|f(\hat{k}_z)(\mathcal{H} - \delta\mathcal{H})\Psi\rangle_z \\ &= \langle\Psi|f(\hat{k}_z)(E - \delta\mathcal{H})\Psi\rangle_z \\ &= \langle(E - \delta\mathcal{H})\Psi|f(\hat{k}_z)\Psi\rangle_z \\ &= \langle(\mathcal{H} - \delta\mathcal{H})\Psi|f(\hat{k}_z)\Psi\rangle_z \\ &= \langle\hat{k}_z\hat{v}_z\Psi|f(\hat{k}_z)\Psi\rangle_z. \end{aligned} \tag{5.51}$$

Substitution into Eq. (5.47) then proves Eq. (5.18) from the main text.

6 Deconfinement of Majorana vortex modes produces a superconducting Landau level

6.1 Introduction

Deconfinement transitions in physics refer to transitions into a phase where particles can exist as delocalized states, rather than only as bound states. Unlike thermodynamic phase transitions, the deconfinement transition is not associated with a spontaneously broken symmetry but with a change in the momentum space topology of the ground state [101]. A prominent example in superconductors is the appearance of a Fermi surface for Bogoliubov quasiparticles when a superconductor becomes gapless [102–105]. Such a Bogoliubov Fermi surface has been observed recently [106].

Motivated by these developments we consider here the deconfinement transition for Majorana zero-modes in the vortex core of a topological superconductor. We will demonstrate, analytically and by numerical simulations, that the delocalized phase at zero chemical potential remains a highly degenerate zero-energy level — a superconducting counterpart of the Majorana Landau level in a Kitaev spin liquid [107, 108]. Unlike a conventional electronic Landau level, the Majorana Landau level has a non-uniform density profile: quantum interference of the electron and hole components creates spatial oscillations with a wave vector set by the Cooper pair momentum that drives the deconfinement transition.

The system of Ref. 106 is shown in Fig. 7.1. It is a thin layer of topological insulator deposited on a bulk superconductor, such that the proximity effect induces a pairing gap Δ_0 in the surface states. A superflow with Cooper pair momentum $\boldsymbol{K}$ lowers the excitation energy for quasiparticles with velocity $\boldsymbol{v}$ by the Doppler shift $\boldsymbol{v}\cdot\boldsymbol{K}$, closing the gap when vK exceeds Δ_0. Following Fu and Kane [8], we add a perpendicular mag-

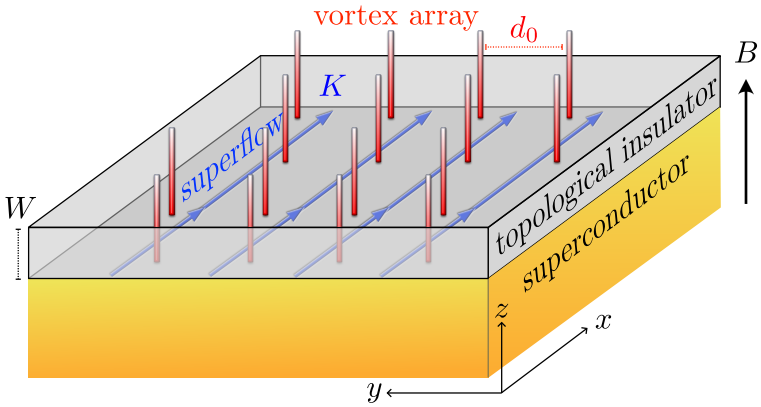

Figure 6.1: Schematic of the Fu-Kane heterostructure [8], a topological insulator with induced superconductivity (gap Δ_0) in a perpendicular magnetic field B. Vortices (red) bind midgap states known as Majorana zero-modes. Here we study the deconfinement transition in response to an in-plane supercurrent (blue arrows, momentum K). When $vK > \Delta_0$ the zero-modes delocalize into a Majorana Landau level.

netic field B to confine a Majorana zero-mode to the core of each $h/2e$ vortex that penetrates the superconductor. We seek to characterize the deconfined phase that emerges when $vK > \Delta_0$.

6.2 Confined phase

To set the stage we first investigate the confined phase for $vK < \Delta_0$. Electrons on the two-dimensional (2D) surface of a 3D topological insulator have the Dirac Hamiltonian $v\boldsymbol{k} \cdot \boldsymbol{\sigma} - \mu$, with μ the chemical potential, v the energy-independent Fermi velocity, $\boldsymbol{k} = (k_x, k_y)$ the momentum operator in the x–y surface plane, and $\boldsymbol{\sigma} = (\sigma_x, \sigma_y)$ two Pauli spin matrices. (The 2×2 unit matrix σ_0 is implicit when the Hamiltonian contains a scalar term.) Application of a perpendicular magnetic field B (in the z-direction), adds an in-plane vector potential $\boldsymbol{A} = (A_x, A_y)$ to the momentum, $\boldsymbol{k} \mapsto \boldsymbol{k} - e\boldsymbol{A}$. The electron charge is $+e$ and for ease of notation we will set v and $\hbar$ both equal to unity in most equations.

The superconducting substrate induces a pair potential $\Delta = \Delta_0 e^{i\phi}$. The phase field $\phi(\boldsymbol{r})$ winds by $\pm 2\pi$ around each vortex, at position $\boldsymbol{R}_n$,

as expressed by

$$\nabla \times \nabla\phi(\boldsymbol{r}) = \pm 2\pi \hat{z} \sum_n \delta(\boldsymbol{r} - \boldsymbol{R}_n), \quad \nabla^2 \phi = 0. \tag{6.1}$$

The pair potential couples electrons and holes in the 4×4 Bogoliubov-De Gennes (BdG) Hamiltonian

$$H = \begin{pmatrix} K\sigma_x + (\boldsymbol{k} - e\boldsymbol{A}) \cdot \boldsymbol{\sigma} & \Delta_0 e^{i\phi} \\ \Delta_0 e^{-i\phi} & K\sigma_x - (\boldsymbol{k} + e\boldsymbol{A}) \cdot \boldsymbol{\sigma} \end{pmatrix}, \tag{6.2}$$

at zero chemical potential, including a superflow momentum field $K \geq 0$ in the x-direction [1]. The superflow can be a screening current in response to a magnetic field in the y-direction [106], or it can result from an externally imposed flux bias or current bias. The Zeeman energy from an in-plane magnetic field has an equivalent effect [103] (although it was estimated to be negligible relative to the orbital effect of the field in the experiment [106]).

For $vK < \Delta_0$ a pair of Majorana zero-modes will appear in each vortex core, one at the top surface and one at the bottom surface. We consider these separately [2]. Setting $\Delta(\boldsymbol{r}) = \Delta_0(r)e^{\pm i\theta}$, in polar coordinates (r, θ) for a $\pm 2\pi$ phase vortex at the origin, we need to solve the zero-mode equation $H_\pm \Psi_\pm = 0$ with

$$H_\pm = \begin{pmatrix} K\sigma_x - (i\nabla + e\boldsymbol{A}) \cdot \boldsymbol{\sigma} & \Delta_0(r)e^{\pm i\theta} \\ \Delta_0(r)e^{\mp i\theta} & K\sigma_x + (i\nabla - e\boldsymbol{A}) \cdot \boldsymbol{\sigma} \end{pmatrix}. \tag{6.3}$$

The pair potential amplitude $\Delta_0(r)$ increases from 0 at $r = 0$ to a value $\Delta_0 > 0$ when r becomes larger than the superconducting coherence length $\xi_0 = \hbar v/\Delta_0$.

When $K = 0$ this is a familiar calculation [109], which is readily generalized to $K > 0$. The Majorana zero-mode has a definite chirality $\mathcal{C}$, meaning that its four-component wave function $\Psi_\pm$ is an eigenstate of the chirality operator $\Lambda = \mathrm{diag}\,(1, -1, -1, 1)$ with eigenvalue $\mathcal{C} = \pm 1$. One

[1] The term $K\sigma_x$ in the BdG Hamiltonian (6.2) is equivalent, upon a gauge transformation, to a gradient $2Kx$ in ϕ.

[2] The overlap of states on the top and bottom surfaces of the topological insulator thin film shifts the Majorana Landau away from $E = 0$ by the hybridization gap, while keeping the spatial structure of the wave functions intact. We include this effect in the calculations in App. 6.A of the Supplemental Material.

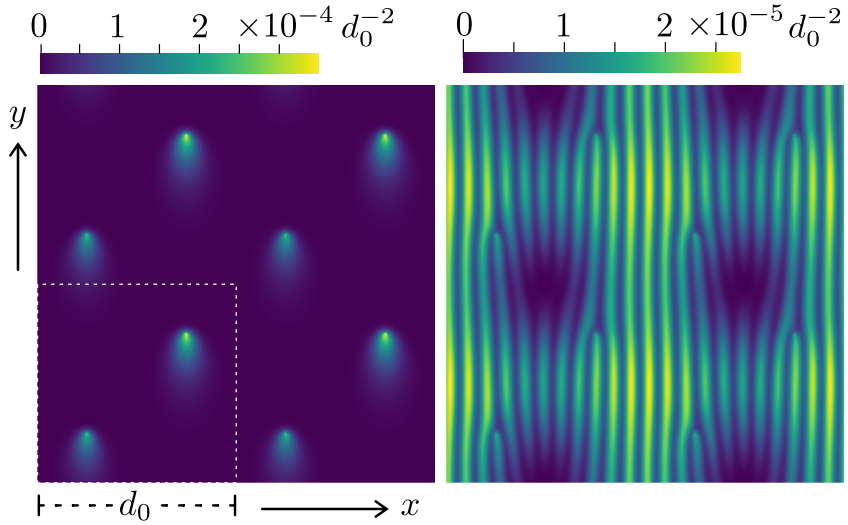

Figure 6.2: Intensity profile $|\Psi(x,y)|^2$ of a Majorana zero-mode in the vortex lattice [110]. The left panel shows the confined phase ($K < \Delta_0$), the right panel the deconfined phase ($K > \Delta_0$). The dotted square indicates the unit cell containing a pair of $h/2e$ vortices. These plots are for Majorana fermions of positive chirality, for negative chirality the density profile is inverted $y \mapsto -y$.

has $\Psi_+ = (i\psi_+, 0, 0, \psi_+)$, $\Psi_- = (0, i\psi_-, \psi_-, 0)$ with [3]

$$\psi_\pm(\boldsymbol{r}) = e^{\mp Ky} e^{\mp\chi(\boldsymbol{r})} \exp\left(-\int_0^r \Delta_0(r')\,dr'\right), \tag{6.4a}$$

$$\chi(\boldsymbol{r}) = \frac{e}{2\pi}\int d\boldsymbol{r}'\, B(\boldsymbol{r}') \ln|\boldsymbol{r}-\boldsymbol{r}'|. \tag{6.4b}$$

The factor $e^{\mp\chi(\boldsymbol{r})}$ is a power law for large r, so the zero-mode is confined exponentially to the vortex core as long as $K < \Delta_0$. When $K > \Delta_0$ the solution (6.4) is no longer normalizable, it diverges exponentially along the y-axis. This signals a transition into a deconfined phase, which we consider next.

[3] To understand how the solution (6.4) relates to the $K = 0$ solution in Ref. [109], note the (non-unitary) transformation $e^{Ky\Lambda} H_\pm e^{Ky\Lambda} = H_\pm + K\sigma_x$, with $\Lambda = \mathrm{diag}\,(1,-1,-1,1)$. The spinor $\Psi_\pm$ is an eigenstate of Λ with eigenvalue ± 1, so if $H_\pm \Psi_\pm = 0$ for $K = 0$, then $H_\pm e^{\pm Ky}\Psi_\pm = 0$ for $K \neq 0$.

6.3 Deconfined phase

In Fig. 6.2 we show results from a numerical simulation of the deconfinement transition for the model Hamiltonian described below. The left panel shows zero-modes confined to a pair of vortex cores for $K < \Delta_0$, the right panel shows the deconfined state for $K > \Delta_0$. The decay $|\Psi| \propto e^{-Ky} e^{-\Delta_0 r}$ in the confined phase is anisotropic, with a decay rate Δ_0 along the x-axis and two different decay rates $\Delta_0 \pm K$ in the $\pm y$-direction. The direction into which the zero-mode decays more slowly is set by the chirality [4]: Fig. 6.2 shows $\mathcal{C} = +1$ with a slow decay in the $-y$ direction, for $\mathcal{C} = -1$ the slow decay is in the $+y$ direction.

In the deconfined phase the zero-mode density profile has a pronounced periodic modulation in the x-direction, parallel to the superflow, with bifuration points at the vortex cores. This striped pattern is unexpected for a Landau level. We present an analytical description.

6.4 Chiral symmetry protected Majorana Landau level

The chiral symmetry of the Hamiltonian (6.2) plays a key role in our analysis of the Majorana Landau level, similar to the role it plays for Landau level quantization in graphene [111, 112] and in a Weyl superconductor [96]. Chiral symmetry means that H at $\mu = 0$ anticommutes with Λ. The Hamiltonian then becomes block-off-diagonal in the basis of eigenstates of Λ,

$$U^\dagger H U = \begin{pmatrix} 0 & \Xi \\ \Xi^\dagger & 0 \end{pmatrix}, \quad U = \begin{pmatrix} 1 & 0 & 0 & 0 \\ 0 & 0 & 1 & 0 \\ 0 & 0 & 0 & 1 \\ 0 & 1 & 0 & 0 \end{pmatrix}, \tag{6.5a}$$

$$\Xi = \begin{pmatrix} k_- - eA_- + K & \Delta_0 e^{i\phi} \\ \Delta_0 e^{-i\phi} & -k_+ - eA_+ + K \end{pmatrix}, \tag{6.5b}$$

where we have abbreviated $k_\pm = k_x \pm i k_y$, $A_\pm = A_x \pm i A_y$.

A zero-mode is either a wave function $(u, 0)$ of positive chirality with $\Xi^\dagger u = 0$, or a wave function $(0, u)$ of negative chirality with $\Xi u = 0$. The

[4] The anisotropic decay of the Majorana zero-mode in the left panel of Fig. 6.2 can be understood as the effect of the Magnus force which the superflow momentum $\boldsymbol{K} = K\hat{x}$ exerts on the axial spin $\boldsymbol{S} = \mathcal{C}\hat{z}$ of the Majorana fermions (as determined by their chirality $\mathcal{C} = \pm 1$). The direction of slow decay of the zero-mode is given by the cross product $\boldsymbol{K} \times \boldsymbol{S}$.

difference between the number of normalizable eigenstates of either chirality is called the index of the Hamiltonian. It is topologically protected, meaning insensitive to perturbations [113].

Vortices are strong scatterers [16], completely obscuring the Landau level quantization in a nontopological superconductor [114]. Here chiral symmetry ensures that the vortices cannot broaden the zeroth Landau level.

6.5 Helmholtz equation for the Majorana Landau level

Let us focus on the Landau level of positive chirality, described by the equation $\Xi^\dagger u = 0$. This 2×2 matrix differential equation can be simplified by the substitution

$$u(\boldsymbol{r}) = e^{-Ky-q(\boldsymbol{r})} e^{\frac{1}{2}i\phi(\boldsymbol{r})\sigma_z} \tilde{u}(\boldsymbol{r}), \tag{6.6}$$

$$\text{with } \partial_x q = -\tfrac{1}{2}\partial_y \phi + eA_y, \quad \partial_y q = \tfrac{1}{2}\partial_x \phi - eA_x, \tag{6.7}$$

$$\Rightarrow \begin{pmatrix} -i\partial_x + \partial_y & \Delta_0 \\ \Delta_0 & i\partial_x + \partial_y \end{pmatrix} \tilde{u} = 0. \tag{6.8}$$

The fields $\boldsymbol{A}$, ϕ, and K no longer appear explicitly in the differential equation (6.8) for $\tilde{u}$, but they still determine the solution by the requirements of normalizability and single-valuedness of the zero-mode u.

Outside of the vortex core the spatial dependence of the pair potential amplitude Δ_0 may be neglected and one further simplification is possible: Substitution of $\tilde{u} = (f, g)$ gives $g = \Delta_0^{-1}(i\partial_x - \partial_y)f$ and a scalar second-order differential equation for f,

$$\nabla^2 f = \Delta_0^2 f. \tag{6.9}$$

In the context of classical wave equations this is the Helmholtz equation with imaginary wave vector.

Eq. (6.6) requires that $\tilde{u}$ and hence f have an exponential envelope e^{Ky} in the y-direction. The Helmholtz equation (6.9) then ties that to a plane wave $\propto e^{\pm iQx}$ in the x-direction, with wave vector $Q = \sqrt{K^2 - \Delta_0^2}$. This already explains the striped pattern in the numerical simulations of Fig. 6.2. For a more detailed comparison we proceed to a full solution of the Helmholtz equation.

6.6 Analytical solution of the Majorana Landau level wave function

The solutions of Eq. (6.9) for f are constrained by the requirements of normalizability and single-valuedness of u. To determine the normalizability constraint we use that the field $q(\boldsymbol{r})$ defined in Eq. (6.7) has the integral representation [5]

$$q(\boldsymbol{r}) = \frac{1}{2\Phi_0} \int d\boldsymbol{r}'\, B(\boldsymbol{r}') \ln|\boldsymbol{r} - \boldsymbol{r}'| - \tfrac{1}{2} \sum_n \ln|\boldsymbol{r} - \boldsymbol{R}_n|. \tag{6.10}$$

We consider $\mathcal{N}$ vortices (each of $+2\pi$ vorticity) in a region S enclosing a flux $\Phi = \mathcal{N}\Phi_0$, with $\Phi_0 = h/2e$ the superconducting flux quantum [6]. If we set $B \to 0$ outside of S, the field $q(\boldsymbol{r}) \to \frac{1}{2}(\Phi/\Phi_0 - \mathcal{N}) \ln r = 0$ for $r \to \infty$. In view of Eq. (6.6), normalizability requires that $e^{-Ky} f$ is square integrable for $r \to \infty$. Near a vortex core $e^{-q} f \propto |\boldsymbol{r} - \boldsymbol{R}_n|^{1/2} f$ must be square integrable [7].

Concerning the single-valuedness, the factor $e^{i\phi/2}$ in Eq. (6.6) introduces a branch cut at each vortex position $\boldsymbol{R}_n$, across which the function f should change sign — to ensure a single-valued u. This is a local constraint: branch cuts can be connected pairwise, hence there is no sign change in f on a contour encircling a vortex pair.

We have obtained an exact analytical solution [115] of the Helmholtz equation in the limit that the separation of a vortex pair goes to zero. We place the two vortices at the origin of a disc of radius R, enclosing a flux h/e, with zero magnetic field outside of the disc. The envelope function then equals $e^{-q(r)} = r_{\min} e^{-r_{\min}^2/2R^2}$, with $r_{\min} = \min(r, R)$.

The two independent solutions are given by $\tilde{u} = (f_1, f_0)$ and $\tilde{u}' = \sigma_x \tilde{u}^*$,

[5] The integral equation (6.10) for $q(\boldsymbol{r})$ follows from the definition (6.7), which implies that $\nabla^2 q(\boldsymbol{r}) = \hat{z} \cdot \nabla \times (e\boldsymbol{A} - \frac{1}{2}\nabla\phi) = eB - \pi \sum_n \delta(\boldsymbol{r} - \boldsymbol{R}_n)$. The Green function of this 2D Poisson equation is $(2\pi)^{-1} \ln|\boldsymbol{r} - \boldsymbol{r}'|$. Also note that $\Phi_0 \equiv \pi/e$ in units where $\hbar \equiv 1$.

[6] We assume there is an even number of vortices in S. If the number of vortices is odd, a zero-energy edge state along the perimeter of S will ensure that the total number of Majorana zero-modes remains even.

[7] This normalization requirement at the vortex core ties the chirality of the Majorana zero-modes to the sign of the vorticity. If we would have chosen -2π vortices the field $q(\boldsymbol{r})$ would tend to $+\frac{1}{2}\ln|r - \boldsymbol{R}_n|$ near a vortex core, and the product $e^{-q} f \propto |\boldsymbol{r} - \boldsymbol{R}_n|^{-1/2} f$ would not have been square integrable.

with

$$f_n = 2i^n e^{-in\theta} \mathrm{K}_n(\Delta_0 r) - \int_{-Q}^{Q} dp\, C_n(p) e^{ixp+y\sqrt{\Delta_0^2+p^2}},$$
$$C_n(p) = \Delta_0^{-n}(\Delta_0^2+p^2)^{-1/2}\big(p-\sqrt{\Delta_0^2+p^2}\big)^n. \tag{6.11}$$

The vortex pair is at the origin, with $x+iy = re^{i\theta}$, and K_n is a Bessel function.

The corresponding zero-modes follow from Eq. (6.6),

$$u = e^{-q(r)} e^{-Ky}(e^{i\theta} f_1, e^{-i\theta} f_0), \quad u' = \sigma_x u^*. \tag{6.12}$$

For small r the zero-modes tend to a constant (the factor $1/r$ from K_1 is canceled by the factor r from e^{-q}). The large-r asymptotics follows upon an expansion of the integrand around the extremal points $\pm Q$, giving

$$f_n \to (-1)^n \frac{e^{Ky}}{\Delta_0^n}\left(\frac{(K+Q)^n e^{-iQx}}{iKx-Qy} - \frac{(K-Q)^n e^{iQx}}{iKx+Qy}\right). \tag{6.13}$$

The zero-modes decay as $e^{-Ky} f_n \propto 1/r$ for $r \gg R$, which needs to be regularized for a square-integrable wave function [8], [116, 117]. In a chain of vortices (spacing b), the superposition of the solution (6.13) decays exponentially in the direction perpendicular to the chain [115]. The decay length is $\lambda = bK/Q$ or $\lambda = bQ/K$ for a chain oriented along the x-axis or y-axis, respectively.

6.7 Numerical simulation

For a numerical study of the deconfinement transition we represent the topological insulator layer by the low-energy Hamiltonian [118, 119]

$$\begin{aligned} H_0(\boldsymbol{k}) &= (v/a_0)\textstyle\sum_{j=x,y}\sigma_j \sin k_j a_0 + \sigma_z M(k) - \mu, \\ M(k) &= M_0 - (M_1/a_0^2)\textstyle\sum_{j=x,y}(1-\cos k_j a_0), \end{aligned} \tag{6.14}$$

in the basis $\Psi = 2^{-1/2}(\psi_{\uparrow\mathrm{upper}} + \psi_{\uparrow\mathrm{lower}}, \psi_{\downarrow\mathrm{upper}} - \psi_{\downarrow\mathrm{lower}})$ of spin-up and spin-down states on the upper and lower surfaces [9]. The atomic lattice

[8] The $1/r$ decay of the deconfined Majorana zero-mode implies a density of states peak which decays slowly $\propto 1/\ln L$ as a function of the system size L. There is a formal similarity here with the zero-modes originating from vacancies in a 2D bipartite lattice [116, 117].

[9] In the basis $\Psi = (\psi_{\uparrow\mathrm{upper}}, \psi_{\downarrow\mathrm{upper}}, \psi_{\uparrow\mathrm{lower}}, \psi_{\downarrow\mathrm{lower}})$ the 4×4 Hamiltonian of the topological insulator layer is $H_0 = t_0 \sum_{j=x,y}\tau_z\sigma_j \sin k_j a_0 + \tau_x\sigma_0 M(k) - \mu$,

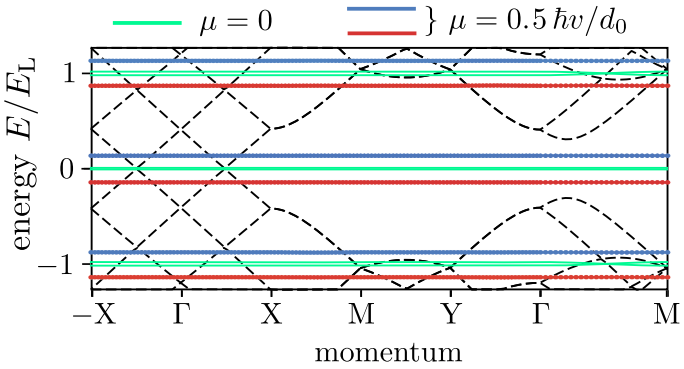

Figure 6.3: Dispersion relation of the topological superconductor, calculated from the model Hamiltonian (6.14) for zero magnetic field (black dashed lines, chemical potential $\mu = 0$) and in the presence of the magnetic vortex lattice (colored flat bands at charge $\pm q_{\rm eff} e$, for two values of μ). For both data sets $K = 2\Delta_0 = 20\,\hbar v/d_0$.

constant is a_0, the Fermi velocity is v, and μ is the chemical potential. Hybridization of the states on the two surfaces introduces the mass term $M(k)$. We set $M_0 = 0$, to avoid the opening of a gap at $k = 0$ [10], but retain a nonzero $M_1 = 0.2\,a_0 v$ in order to eliminate the fermion doubling at $a_0 \boldsymbol{k} = (\pi, \pi)$.

In the corresponding BdG Hamiltonian the electron block $H_0(\boldsymbol{k} - e\boldsymbol{A} + \boldsymbol{K})$ is coupled to the hole block $-H_0(\boldsymbol{k} + e\boldsymbol{A} - \boldsymbol{K})$ by the s-wave pair potential $\Delta_0 e^{i\phi}$, which we take the same for both layers. We assume a strong type-II superconductor, for which we can take a uniform magnetic field B and uniform pair potential amplitude Δ_0. The $+2\pi$ vortices are positioned on a square lattice (lattice constant $d_0 = 302\,a_0$) with two vortices per unit cell.

The spectrum is calculated using the *Kwant* tight-binding code [47, 120]. In Fig. 6.3 we show the dispersionless Landau levels, both for chemical potential $\mu = 0$ and for nonzero μ. The zeroth Landau level has energy $E_0 = \pm q_{\rm eff}\mu$, with $q_{\rm eff} e$ the charge expectation value. For the

with Pauli matrix τ_z acting on the layer index. A unitary transformation block-diagonalizes the Hamiltonian. One of the 2×2 blocks is given in Eq. (6.14), the other block has M replaced by $-M$.

[10] The overlap of states on the top and bottom surfaces of the topological insulator thin film shifts the Majorana Landau away from $E = 0$ by the hybridization gap, while keeping the spatial structure of the wave functions intact. We include this effect in the calculations in App. 6.A of the Supplemental Material.

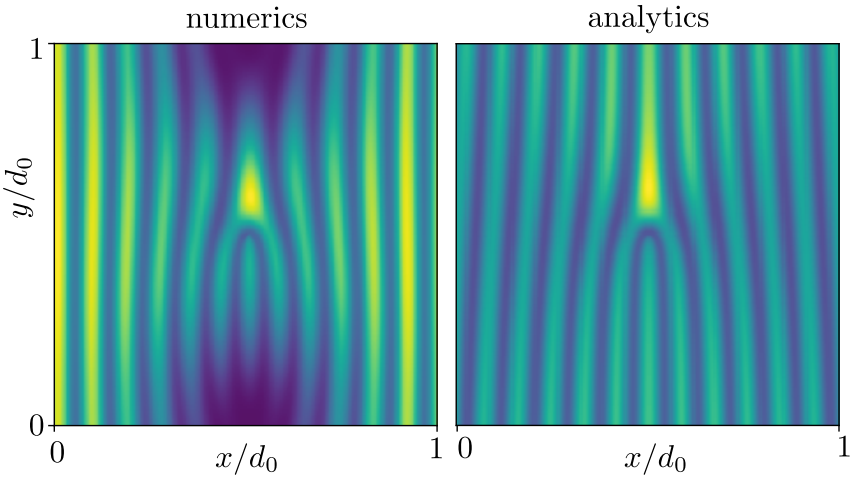

Figure 6.4: Left panel: Numerically calculated intensity profile $|\Psi(x,y)|^2$ of the zeroth Landau level in a vortex lattice with a pair of $h/2e$ vortices at the center of the unit cell ($K = 2\Delta_0 = 40\,\hbar v/d_0$, $\mu = 0$). Right panel: Analytical result from the solution of the Helmholtz equation (6.9) for a single h/e vortex.

model Hamiltonian (6.2) we have [121] $q_{\rm eff} = Q/K = \sqrt{1-\Delta_0^2/K^2}$. The numerics at $K = 2\Delta_0$ gives a value 0.85, within 2% of $\sqrt{3/4} = 0.866$. The first Landau level is expected at energy $E_1 = E_{\rm L} \pm q_{\rm eff}\mu$ with $E_{\rm L} = \sqrt{4\pi q_{\rm eff}}\,\hbar v/d_0$, again in very good agreement with the numerics. Notice that the flatness of the dispersion persists at nonzero μ — even though the topological protection due to chiral symmetry [11] is only rigorously effective at $\mu = 0$.

In Fig. 6.4 we compare numerical and analytical results for the case that the two $h/2e$ vortices are both placed at the center of the unit cell. The agreement is quite satisfactory, given the different geometries (a vortex lattice in the numerics, a single h/e vortex in the analytics) [12].

[11] The chiral symmetry at $\mu = 0$ is broken by the mass term $M(k)$ in the Hamiltonian (6.14). This residual chiral symmetry breaking is visible in Fig. 6.3 as a very small splitting of the $\mu = 0$ Landau levels (green flat bands).

[12] The comparison between numerics and analytics in Fig. 6.4 involves no adjustable parameters. To compare the same state in the degenerate zeroth Landau level we choose the state with left-right reflection symmetry. There are two of these, the other is compared in App. 6.E of the Supplemental Material.

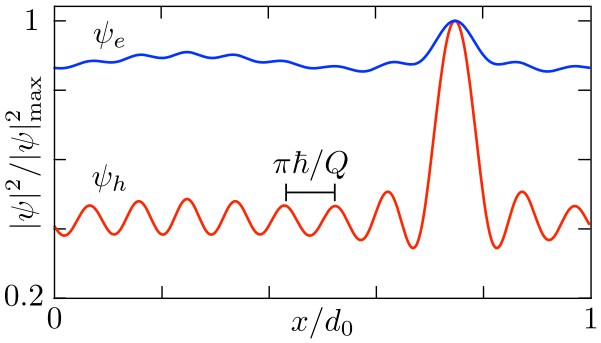

Figure 6.5: Electron and hole contributions to the local density of states in the zeroth Landau level, along a line parallel to the x-axis which passes close through a vortex core at $x = y = 3d_0/4$. The curves are plots of $\sum_{\boldsymbol{k}} |\psi_{e,h}(x,y)|^2$ normalized to unit peak height at the vortex core. The parameters are $K = 2\Delta_0 = 40\,\hbar v/d_0$, $\mu = 0.5\,\hbar v/d_0$. The expected oscillation period of $\pi\hbar/Q = 0.091\,d_0$ is indicated.

6.8 Striped local density of states

The striped pattern of the Majorana Landau level is observable by tunneling spectroscopy, which measures the local density of states

$$\rho(\boldsymbol{r}) = \sum_{\boldsymbol{k}} \big[|\psi_e(\boldsymbol{r})|^2 f'(E_0 - eV) + |\psi_h(\boldsymbol{r})|^2 f'(E_0 + eV) \big], \qquad (6.15)$$

averaged over the 2D magnetic Brillouin zone, $\sum_{\boldsymbol{k}} = (2\pi)^{-2} \int dk_x dk_y$, weighted by the derivative of the Fermi function. If E_0 is much larger than temperature, the sign of the bias voltage V determines whether the electron component ψ_e or the hole component ψ_h contributes, so these can be measured separately.

As shown in Fig. 6.5, the oscillations are most pronounced for the hole component when $\mu > 0$ (or equivalently the electron component when $\mu < 0$). This asymmetry in the tunneling current for $V = \pm E_0$ is an additional experimental signature of the effect.

6.9 Conclusion

Concerning the experimental feasibility, we note that the gap closing due to a superflow has already been observed [106], and Majorana vortex lattices in a perpendicular field of 250 mT have been detected by scanning probes in several experiments [124] — so by combining these two

ingredients the Majorana Landau level should become accessible. The main additional requirement is that the Fermi level is sufficiently small, $\mu < \min(E_{\mathrm{L}}, \Delta_0) \simeq 1\,\mathrm{meV}$ at 250 mT, to benefit from the protection afforded by chiral symmetry. Experiments [125] where μ was tuned through the charge neutrality point give confidence that this is feasible.

The striped interference pattern in the local density of states, with wave number $Q = \sqrt{K^2 - (\Delta_0/\hbar v)^2}$ ($\simeq 2\pi/0.2\,\mu\mathrm{m}$ for $K = 2\Delta_0/\hbar v$ at typical values of $\Delta_0 = 1\,\mathrm{meV}$ and $v = 10^5\,\mathrm{m/s}$) should be accessible by scanning probe spectroscopy. Surface defects would themselves introduce Friedel oscillations in the density of states, but the highly directional pattern that is the hallmark of the Majorana Landau level would stand out.

The Majorana Landau level provides a realization of a flat band with extended wave functions, in which interaction effects are expected to be enhanced due to the quenching of kinetic energy. Interacting Majorana fermions in a Fu-Kane superconductor have been studied by placing vortices in close proximity inside a quantum dot [126]. The deconfinement transition provides a means to open up the system and obtain a fully 2D flat band with widely separated vortices. An intriguing topic for further research is to investigate how the exchange of vortices operates on this highly degenerate manifold.

Appendices

6.A Details of the numerical simulation

6.A.1 Tight-binding model

The model Hamiltonian we consider is

$$\mathcal{H}_\pm = \begin{pmatrix} H_\pm(\boldsymbol{k} - e\boldsymbol{A} + \boldsymbol{K}) & \Delta_0 e^{i\phi} \\ \Delta_0 e^{-i\phi} & -H_\pm(\boldsymbol{k} + e\boldsymbol{A} - \boldsymbol{K}) \end{pmatrix}, \tag{6.16a}$$

$$H_\pm(\boldsymbol{k}) = \pm(v/a_0)\sigma_x \sin a_0 k_x \pm (v/a_0)\sigma_y \sin a_0 k_y \pm \sigma_z M(k) - \mu, \tag{6.16b}$$

$$M(k) = M_0 - (M_1/a_0^2)(2 - \cos a_0 k_x - \cos a_0 k_y). \tag{6.16c}$$

The Hamiltonian acts on a spinor with the four components

$$\Psi_\pm(\boldsymbol{k}) = \frac{1}{\sqrt{2}} \begin{pmatrix} [\psi_{\uparrow\mathrm{upper}} \pm \psi_{\uparrow\mathrm{lower}}](\boldsymbol{k}) \\ [\psi_{\downarrow\mathrm{upper}} \mp \psi_{\downarrow\mathrm{lower}}](\boldsymbol{k}) \\ -i[\psi_{\downarrow\mathrm{upper}} \pm \psi_{\downarrow\mathrm{lower}}]^*(-\boldsymbol{k}) \\ i[\psi_{\uparrow\mathrm{upper}} \mp \psi_{\uparrow\mathrm{lower}}]^*(-\boldsymbol{k}) \end{pmatrix}, \tag{6.17}$$

for spin-up and spin-down electrons on the upper and lower surface of the topological insulator layer. The first two elements of the spinor Ψ refer to electrons and the last two elements to holes. These are coupled by the s-wave pair potential Δ_0, which we take the same on both surfaces. The particle-hole symmetry relation is

$$\mathcal{H}_\pm(\boldsymbol{k}) = -\sigma_x \nu_y \mathcal{H}_\mp^*(-\boldsymbol{k}) \sigma_x \nu_y, \tag{6.18}$$

where the σ_α and τ_α Pauli matrices act on the spin and electron-hole degree of freedom, respectively.

For the mass term $M(k)$ we take $M_0 = 0$, $M_1 = 0.2\, a_0 v$, such that H_0 has a single gapless Dirac point at $\boldsymbol{k} = 0$. Near this Dirac point the upper and lower surface are uncoupled, so the eigenstate can equivalently be written in the single-surface basis $(\psi_\uparrow, \psi_\downarrow, -i\psi_\downarrow^*, i\psi_\uparrow^*)$. The effect of a gap opening due to a nonzero M_0 is examined at the end of this Appendix.

The Hamiltonian is discretized on a square lattice (lattice constant a_0) with nearest neighbor hopping (hopping energy v/a_0). The magnetic field B is uniform in the z-direction, vector potential $\boldsymbol{A} = -By\hat{x}$. The superflow momentum is $\boldsymbol{K} = K\hat{x}$. The amplitude Δ_0 of the pair potential is taken as a constant, the phase $\phi(x, y)$ winds by 2π around each vortex.

We take a square vortex lattice, with lattice constant $d_0 = Na_0$. The flux through each magnetic unit cell is h/e, so it contains a pair of $h/2e$ vortices. The integer N determines the magnetic field via $B = (Na_0)^{-2}h/e$. The vortices are placed on the diagonal of the magnetic unit cell, at the positions $(x, y) = (Na_0/4)(1, 1)$ and $(Na_0/4)(3, 3)$. By taking for N twice an odd integer, we ensure that the singularity in the phase field at the vortex core does not coincide with a lattice point. The phase field is discretized along the lines set out in App. B of Ref. 96. The eigenvalues and eigenfunctions of H are calculated using the *kwant* tight-binding code [47].

6.A.2 Additional numerical results

Here we collect some additional results to those shown in the main text. In the confined phase $vK < \Delta_0$ we show in Fig. 6.6 the anisotropic decay rates of the Majorana zero-modes bound to a vortex core, as in the left panel of Fig. 6.2. The localization length $(\Delta_0/v - K)^{-1}$ of the zero-modes diverges at the transition.

Fig. 6.7 shows how at the deconfinement transition the quasi-continuum of excited states in the vortex core is reorganized into a sequence of Landau levels. The critical exponents for the gap closing are different on the two sides of the transition. In the confined phase the gap to the first excited state scales with the inverse localization length, so $\propto (\Delta_0/v - K)^1$. In the deconfined phase the gap scales with the Landau level separation $E_{\mathrm{L}} \propto \sqrt{q_{\mathrm{eff}}}$, so $\propto (K - \Delta_0/v)^{1/4}$.

In the deconfined phase $vK > \Delta_0$ we show in Fig. 6.8 the Landau levels in the vortex lattice (complementing Fig. 6.3). Fig. 6.9 shows the local density of states in the zeroth Landau level. This shows the variation over the entire unit cell of the vortex lattice, to complement the line cut through a vortex core shown in Fig. 6.5 of the main text.

6.A.3 Effect of overlap of top and bottom surface states

A nonzero mass term $\pm M_0\sigma_z\nu_z$ in the Hamiltonian (6.16) opens up a hybridization gap in the Dirac cone. Since the Majorana Landau level is

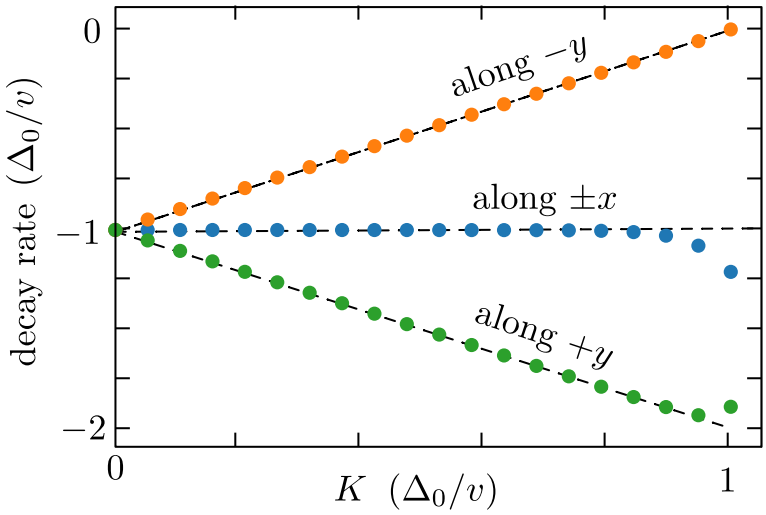

Figure 6.6: Decay rate of the Majorana mode confined to a vortex core. The data from the numerical simulation (colored points, $\Delta_0 = 20\, v/d_0$) closely follows the analytical prediction $|\Psi| \propto e^{-Ky} e^{-(\Delta_0/v)r}$ (dashed lines).

an eigenstate of the chirality operator $\Lambda = \sigma_z \nu_z$, the effect of this term is to displace the flat band away from $E = 0$ by an amount M_0. In Fig. 6.10 we show numerical results that demonstrate this. Provided that M_0 remains smaller than the Landau level separation E_L, we do not expect the overlap of top and bottom surface states to prevent the detection of the Majorana Landau level. This is helpful because the overlap will favor a strong proximity effect on both surfaces.

6.B Solution of the Helmholtz equation for the Majorana Landau level

The general solution of the 2D Helmholtz equation $\nabla^2 f = \Delta_0^2 f$ that governs the Majorana Landau level is a superposition of waves $e^{ipx \pm y\sqrt{p^2+\Delta_0^2}}$. Which superposition we need is determined by the requirement that $e^{-Ky-q(\boldsymbol{r})} f(x,y)$ is square integrable in the x–y plane, with $K > \Delta_0 > 0$. We denote $Q = \sqrt{K^2 - \Delta_0^2}$. For ease of notation we will set $\Delta_0 \equiv 1$ in this appendix.

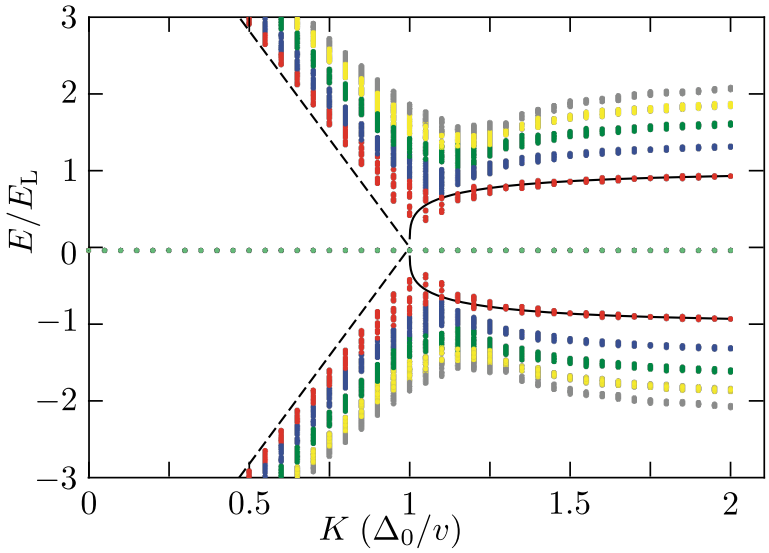

Figure 6.7: Excitation spectrum as a function of the superflow momentum (parameters as in Fig. 6.2). For $K < \Delta_0/v$ the states are confined to vortex cores and form a quasi-continuum, for $K > \Delta_0/v$ they are extended states arranged into a sequence of Landau levels (distinguished by different colors, the Majorana zero-modes are the light-green dots). The deconfinement transition at $K = \Delta_0/v$ is accompanied by a near closing of the gap to the first excited state. The dashed curves show the expected gap scaling $\propto (\Delta_0/v - K)$ and $\propto (K - \Delta_0/v)^{1/4}$ on the two sides of the transition.

We construct a class of solutions for the case

$$q(\boldsymbol{r}) = \epsilon r - \mathcal{N} \ln \min(r, 1), \quad \mathcal{N} = 1, 2, \ldots, \tag{6.19}$$

corresponding to $2\mathcal{N}$ vortices, each of vorticity $+2\pi$, at the origin. The positive infinitesimal $\epsilon > 0$ is introduced to regularize integrals at $r \to \infty$. The restriction to an even number of overlapping vortices means that the branch cut which connects vortices pairwise can be ignored. (We have not succeeded in finding an analytical solution that incorporates the branch cut, but of course in the numerics this is not a limitation.)

The superposition of elementary solutions $e^{ipx \pm y\sqrt{p^2+1}}$ that cancels the

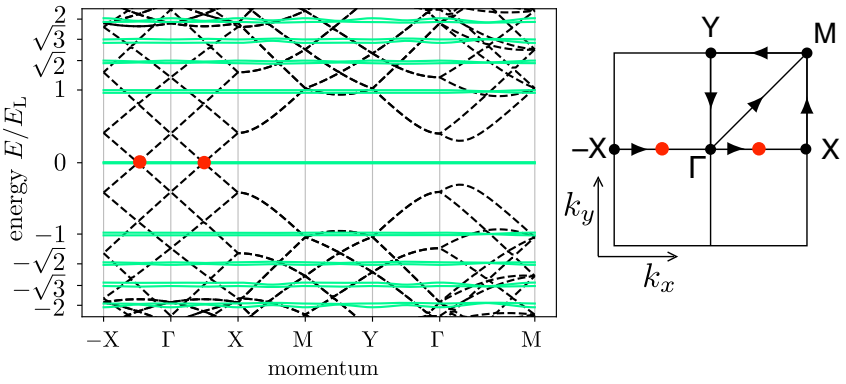

Figure 6.8: Dispersion relation in zero magnetic field (black dashed lines) and in the presence of the magnetic vortex lattice (green solid lines, the right panel shows the magnetic Brillouin zone). Both band structures are for $\mu = 0$, and the same parameters as in Fig. 6.3. The red dots indicate the Dirac points at $\boldsymbol{k} = (\pm Q, 0)$ in zero magnetic field. The Landau levels are at $\pm\sqrt{n}\,E_L$, $n = 0, 1, 2$, with $E_L = \sqrt{4\pi q_{\text{eff}}}\,\hbar v/d_0$.

exponential growth factor e^{-Ky} has the general form

$$f = \begin{cases} \int_{|p|>Q} dp\, C(p) e^{ipx+y\sqrt{p^2+1}} & \text{if } y < 0, \\ -\int_{|p|<Q} dp\, C(p) e^{ipx+y\sqrt{p^2+1}} & \\ \quad + \int dp\, D(p) e^{ipx-y\sqrt{p^2+1}} & \text{if } y > 0. \end{cases} \tag{6.20}$$

(We can use the symbol C twice without loss of generality because the integration ranges do not overlap.)

The solution should be continuously differentiable at $r \neq 0$, which is satisfied if $f(x, y)$ and $\partial_y f(x, y)$ are continuous functions of y at $y = 0$, $x \neq 0$. The continuity requirement is that the Fourier transform $\int \cdots e^{ipx} dp$ of $C(p)$ equals the Fourier transform of $D(p)$ for $x \neq 0$, which means that $C(p)$ and $D(p)$ differ by a polynomial $L(p)$ of p. [Recall that the Fourier transform of a polynomial is given by derivatives of $\delta(x)$.] Similarly, the requirement of a continuous derivative is that $\sqrt{p^2+1}\,C(p)$ and $-\sqrt{p^2+1}\,D(p)$ differ by a polynomial $T(p)$. The unique solution of these

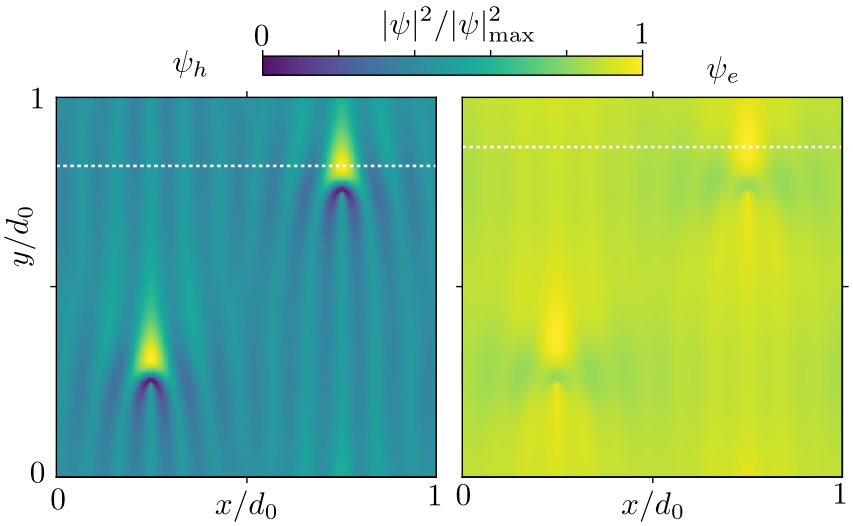

Figure 6.9: Local density of states in the unit cell of the vortex lattice, at the energy $E_0 > 0$ of the zeroth Landau level pushed above the Fermi level by a chemical potential $\mu > 0$. The color scale plot shows $\sum_{\boldsymbol{k}} |\psi_{e,h}(x,y)|^2$, summed over the magnetic Brillouin zone, normalized to unit maximum value. The white dotted line indicates the cut shown in Fig. 6.5 of the main text, at the same parameters. The electron contribution to the local density of states (right panel) and the hole contribution (left panel) can be measured separately by tunnel spectroscopy at voltages $V = E_0$ and $V = -E_0$, respectively.

two requirements is

$$\begin{aligned} C(p) &= \frac{\frac{1}{2}T(p)}{\sqrt{p^2+1}} - \tfrac{1}{2}L(p), \\ D(p) &= \frac{\frac{1}{2}T(p)}{\sqrt{p^2+1}} + \tfrac{1}{2}L(p). \end{aligned} \tag{6.21}$$

We are free to choose a convenient basis for the polynomials $T(p)$ and $L(p)$, we will choose one for which the integral over $D(p)$ has a closed-form expression. The basis polynomials $T_n(p)$ and $L_n(p)$, $n = 0, 1, 2, \ldots$ are

$$\begin{aligned} T_n(p) &= \left(p + \sqrt{p^2+1}\right)^n + \left(p - \sqrt{p^2+1}\right)^n, \\ L_n(p) &= \frac{\left(p + \sqrt{p^2+1}\right)^n}{\sqrt{p^2+1}} - \frac{\left(p - \sqrt{p^2+1}\right)^n}{\sqrt{p^2+1}}. \end{aligned} \tag{6.22}$$

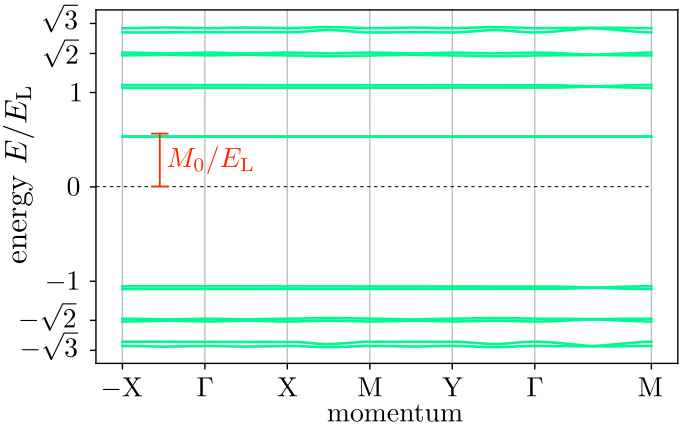

Figure 6.10: Same as Fig. 6.8, but now for a nonzero mass term M_0, to show how the hybridization gap shifts the zeroth Landau level away from $E = 0$. The plot shows the spectrum of the Hamiltonian $\mathcal{H}_+$ in Eq. (6.16), the spectrum of $\mathcal{H}_-$ has the zeroth Landau level shifted to $-M_0$ (so that the full spectrum is particle-hole symmetric). The parameters are $K = 2\Delta_0 = 20\,\hbar v/d_0$, $d_0 = 102\,a_0$, $M_0 = 0.02/a_0$, $M_1 = 0.2\,a_0$.

This choice of basis is related to a basis of Chebyshev polynomials $\mathcal{T}_n$, via the identities

$$\begin{aligned} T_n(p) &= 2(-i)^n \mathcal{T}_n(ip), \\ L_n(p) &= 2(-i)^{n-1} \sum_{m=0}^{n-1} \mathcal{T}_{2m-n+1}(ip). \end{aligned} \tag{6.23}$$

Note that

$$T_{-n}(p) = (-1)^n T_n(p), \quad L_{-n}(p) = -(-1)^n L_{-n}(p). \tag{6.24}$$

A complete basis for the pairs of polynomials $T(p), L(p)$ is therefore given by the two sets $\{T_n, L_n\} \cup \{T_n, -L_n\}$ with $n = 0, 1, 2, \ldots$, or equivalently by the single set $\{T_n, L_n\}$ with $n = 0, \pm 1, \pm 2, \ldots$. The corresponding basis of the functions $C(p)$ and $D(p)$ in Eq. (6.21) is

$$\begin{aligned} C_n(p) &= \frac{\frac{1}{2}T_n(p)}{\sqrt{p^2+1}} - \tfrac{1}{2}L_n(p) = \frac{\left(p - \sqrt{p^2+1}\right)^n}{\sqrt{p^2+1}}, \\ D_n(p) &= \frac{\frac{1}{2}T_n(p)}{\sqrt{p^2+1}} + \tfrac{1}{2}L_n(p) = \frac{\left(p + \sqrt{p^2+1}\right)^n}{\sqrt{p^2+1}}, \end{aligned} \tag{6.25}$$

with $n = 0, \pm 1, \pm 2, \ldots$.

We next use the Bessel function identities [13]

$$\mathrm{K}_n(r) = \begin{cases} \frac{1}{2i^n} e^{in\theta} \int_{-\infty}^{\infty} dp\, D_n(p) e^{ipx - y\sqrt{p^2+1}} & \text{if } y \geq 0, \\ \frac{1}{2i^n} e^{in\theta} \int_{-\infty}^{\infty} dp\, C_n(p) e^{ipx + y\sqrt{p^2+1}} & \text{if } y \leq 0, \end{cases} \tag{6.26}$$

where $r = \sqrt{x^2+y^2}$ and $e^{i\theta} = (x+iy)/r$, to write the solution (6.20) in the form

$$\begin{aligned} f_n(x,y) = &- \int_{-Q}^{Q} dp\, \frac{\left(p - \sqrt{p^2+1}\right)^n}{\sqrt{p^2+1}} e^{ixp + y\sqrt{p^2+1}} \\ &+ 2i^n e^{-in\theta} \mathrm{K}_n(r), \end{aligned} \tag{6.27}$$

which is Eq. (6.11) in the main text (upon restoring the units of Δ_0).

The function f_n is the first component of the spinor $\tilde{u} = (f, g)$, the second component is

$$g_n = (i\partial_x - \partial_y) f_n = f_{n-1}. \tag{6.28}$$

We now obtained an infinite countable set of solutions $\tilde{u}_n = (f_n, f_{n-1})$, $n = 0, \pm 1, \pm 2, \ldots$ of the Helmholtz equation, such that $e^{-Ky} e^{-\epsilon r} \tilde{u}_n$ is square integrable at infinity. The condition that $r^{\mathcal{N}} \tilde{u}$ is square integrable at the origin (containing $2\mathcal{N}$ overlapping vortices) selects a finite subset. For $r \to 0$ we have $f_n \simeq r^{-|n|}$ if $n \neq 0$ and $f_0 \simeq \ln r$. Normalizability requires that both $|n| \leq \mathcal{N}$ and $|n-1| \leq \mathcal{N}$, hence there are $2\mathcal{N}$ allowed values of $n \in \{-\mathcal{N}+1, -\mathcal{N}+2, \ldots \mathcal{N}-1, \mathcal{N}\}$.

All of this was for zero-modes $\Psi = (f, g, 0, 0)$ of positive chirality, in a lattice of $+2\pi$ vortices. Alternatively, we can consider zero-modes $\Psi = (0, 0, f, g)$ of negative chirality in a lattice of -2π vortices. The differential equations for f and g remain the same, but now the exponential factor that needs to be canceled is e^{Ky} rather than e^{-Ky}. The sign change gives the negative chirality solution

$$\begin{aligned} f_n(x,y) = &- \int_{-Q}^{Q} dp\, \frac{\left(p - \sqrt{p^2+1}\right)^n}{\sqrt{p^2+1}} e^{ixp - y\sqrt{p^2+1}} \\ &+ 2i^n e^{in\theta} \mathrm{K}_n(r), \end{aligned} \tag{6.29a}$$

$$g_n = (i\partial_x - \partial_y) f_n = -f_{n+1}. \tag{6.29b}$$

The $2\mathcal{N}$ zero-modes are now labeled by the index $n \in \{-\mathcal{N}, -\mathcal{N}+1, \ldots \mathcal{N}-2, \mathcal{N}-1\}$.

[13] The identities (6.26) follow from the integral representation $\mathrm{K}_n(r) = \frac{1}{2}(r/2)^n \int_0^\infty t^{-n-1} \exp(-t - \frac{1}{4}r^2/t)\, dt$, upon the substitution $p = \frac{1}{2}(t - 1/t)$.

6.C Chain of vortices

The regularization at infinity by the ϵ term in Eq. (6.19) is not needed if we have a periodic lattice of vortices. We demonstrate this by considering a linear chain of vortices at positions $\boldsymbol{R}_\ell$, spaced by b at an angle $\vartheta \in [0, \pi/2]$ with the x-axis. We take a linear superposition of the solutions $e^{-Ky} f_n(\boldsymbol{r} - \boldsymbol{R}_\ell)$ from Eq. (6.27), with complex weights,

$$F_n(\boldsymbol{r}) = \sum_{\ell=-\infty}^{\infty} e^{i\ell\kappa} e^{\ell K b \sin\vartheta} e^{-Ky} f_n(\boldsymbol{r} - \boldsymbol{R}_\ell). \tag{6.30}$$

We do not include the envelope e^{-q}, because it tends to unity for large r if we set $\epsilon \equiv 0$. The Bloch phase κ is arbitrary.

We substitute the large-r expansion (6.13),

$$\begin{aligned} F_n \to (-1)^n \sum_{\ell=-\infty}^{\infty} & e^{i\ell\kappa} \left(\frac{(K+Q)^n e^{-iQ(x-\ell b\cos\vartheta)}}{iK(x-\ell b\cos\vartheta) - Q(y-\ell b\sin\vartheta)} \right) \\ & - e^{i\ell\kappa} \left(\frac{(K-Q)^n e^{iQ(x-\ell b\cos\vartheta)}}{iK(x-\ell b\cos\vartheta) + Q(y-\ell b\sin\vartheta)} \right). \end{aligned} \tag{6.31}$$

We seek the decay of F_n in the direction perpendicular to the chain, so for large $|\rho|$ when $(x, y) = (-\rho\sin\vartheta, \rho\cos\vartheta)$.

We thus need to evaluate an infinite sum of the form [14]

$$S(\alpha, z) = \sum_{\ell=-\infty}^{\infty} \frac{e^{i\ell\alpha}}{z+\ell}, \quad \alpha \in (0, 2\pi), \quad z \in \mathbb{C}\backslash\mathbb{Z}, \tag{6.32a}$$

$$S(\alpha, z) = \frac{2\pi i}{e^{i\alpha z} - e^{i(\alpha-2\pi)z}}. \tag{6.32b}$$

In the limit $|\mathrm{Im}\, z| \to \infty$ this tends to

$$S(\alpha, z) \to \begin{cases} -2\pi i e^{-(2\pi-\alpha)\mathrm{Im}\, z} & \text{if } \mathrm{Im}\, z \to \infty, \\ 2\pi i e^{\alpha \mathrm{Im}\, z} & \text{if } \mathrm{Im}\, z \to -\infty. \end{cases} \tag{6.33}$$

Substitution of Eq. (6.32) into Eq. (6.31) gives, for $x = -\rho\sin\theta$, $y = \rho\cos\theta$,

$$\begin{aligned} F_n \to & \frac{(-1)^n (K+Q)^n e^{iQ\rho\sin\vartheta}}{Qb\sin\vartheta - iKb\cos\vartheta} S(\alpha_+, z_-) \\ & + \frac{(-1)^n (K-Q)^n e^{-iQ\rho\sin\vartheta}}{Qb\sin\vartheta + iKb\cos\vartheta} S(\alpha_-, z_+), \end{aligned} \tag{6.34}$$

[14] For a derivation of Eq. (6.32b), and its relation to the Lerch zeta function, see https://mathoverflow.net/q/379157/11260.

where we abbreviated

$$\begin{aligned} \alpha_\pm &= \kappa \pm Qb\cos\vartheta \mod 2\pi, \\ z_\pm &= \frac{\rho}{b}\frac{\frac{1}{2}\sin 2\vartheta \pm iKQ}{K^2-\sin^2\vartheta}. \end{aligned} \tag{6.35}$$

Provided that $\alpha_\pm \neq 0 \mod 2\pi$, the decay is exponential: $|F_n| \simeq e^{-c|\rho|/\lambda}$, with (reinserting the units of Δ_0)

$$\lambda = b\frac{K^2-\Delta_0^2\sin^2\vartheta}{K\sqrt{K^2-\Delta_0^2}} \tag{6.36}$$

and c a coefficient of order unity that depends on the sign of ρ,

$$c = \begin{cases} \min(\alpha_+, 2\pi-\alpha_-) & \text{if } \rho>0, \\ \min(\alpha_-, 2\pi-\alpha_+) & \text{if } \rho<0. \end{cases} \tag{6.37}$$

For a chain oriented along the x-axis or y-axis we have λ equal to bK/Q or bQ/K, respectively.

6.D Renormalized charge in the Majorana Landau level

The charge expectation value of the deconfined zero-mode can be calculated by means of the block diagonalization approach of Ref. 96. Starting from the BdG Hamiltonian (6.2) we first make the gauge transformation $H \mapsto U^\dagger H U$ with $U = \begin{pmatrix} e^{i\phi} & 0 \\ 0 & 1 \end{pmatrix}$, resulting in

$$\begin{aligned} H &= \begin{pmatrix} (\boldsymbol{k}+\boldsymbol{a}+\boldsymbol{q})\cdot\boldsymbol{\sigma}-\mu & \Delta_0 \\ \Delta_0 & -(\boldsymbol{k}+\boldsymbol{a}-\boldsymbol{q})\cdot\boldsymbol{\sigma}+\mu \end{pmatrix}, \\ \boldsymbol{a} &= \tfrac{1}{2}\nabla\phi, \quad \boldsymbol{q} = \tfrac{1}{2}\nabla\phi - e\boldsymbol{A} + K\hat{x}. \end{aligned} \tag{6.38}$$

We have included the chemical potential μ.

For $K > \Delta_0$ in zero magnetic field there are gapless Dirac points at $\boldsymbol{k} = (k_x, k_y) = (\tilde{K}, 0)$ with

$$\tilde{K} = \pm\kappa K, \quad \kappa = \sqrt{1-\Delta_0^2/K^2}. \tag{6.39}$$

To focus on the effect of a magnetic field on states near $\tilde{K}$ we set $k_x = \tilde{K} + \delta k_x$ and consider δk_x small.

A unitary transformation $H \mapsto V^\dagger H V$ with

$$V = \begin{pmatrix} \sigma_0 \cos(\alpha/2) & \sigma_x \sin(\alpha/2) \\ -\sigma_x \sin(\alpha/2) & \sigma_0 \cos(\alpha/2) \end{pmatrix}, \tag{6.40}$$
$$\tan\alpha = -\Delta_0/\tilde{K}, \;\; \cos\alpha = -(1+\Delta_0^2/\tilde{K}^2)^{-1/2} = -\kappa,$$

approximately block-diagonalizes the Hamiltonian; the 2×2 off-diagonal blocks contribute to the spectrum in second order in δk_x, $\boldsymbol{a}$, $\boldsymbol{q}$, and μ. The 2×2 block along the diagonal that describes the hole-like states near $\boldsymbol{k} = (\kappa K, 0)$ is given by

$$H_+ = \kappa\mu - (\kappa\delta k_x + \kappa a_x - q_x)\sigma_x + (k_y + a_y - \kappa q_y)\sigma_y, \tag{6.41}$$

while the electron-like states near $\boldsymbol{k} = (-\kappa K, 0)$ are described by

$$H_- = -\kappa\mu + (\kappa\delta k_x + \kappa a_x + q_x)\sigma_x - (k_y + a_y + \kappa q_y)\sigma_y. \tag{6.42}$$

The block diagonalization removes any interference between the electron and hole blocks, so this approximation cannot describe the striped density of states of Fig. 6.2 — for that we need the Helmholtz equation considered in the main text. Because the charge operator $\hat{Q} = -e\partial H_\pm/\partial\mu = \mp\kappa e$ commutes with $H_\pm$, the expectation value is given simply by

$$\langle\hat{Q}\rangle = \mp\kappa e \Rightarrow q_{\text{eff}} = \kappa. \tag{6.43}$$

The Fermi velocity in the x-direction is renormalized by the same factor, $v_x = \kappa v$, while v_y is unaffected. This affects the Landau level energy $E_{\text{L}} = \sqrt{4\pi}\,\hbar v_{\text{eff}}/d_0$ of the anisotropic Dirac cone, via $v_{\text{eff}} = \sqrt{v_x v_y} = \sqrt{\kappa} v$.

6.E Comparison of numerics and analytics

In order to compare the analytic solution (6.11) of the Helmholtz equation with the numerical results from the tight-binding Hamiltonian (6.14) we proceed as follows. For the analytic solution we take a single pair of vortices located at $\boldsymbol{r} = 0$, in a uniform magnetic field with total flux h/e in a large disc centered at the origin. There are then two independent zero-modes u, u' given by Eq. (6.12) with $q(r) = -\ln r$.

For the numerical calculation we consider an infinite lattice of vortices, with pairs of vortices positioned at points $\boldsymbol{R_n} = d_0\boldsymbol{n}$, $\boldsymbol{n} \in \mathbb{Z}^2$, in a uniform magnetic field $B = (h/e)d_0^{-2}$, vector potential $\boldsymbol{A} = -B(y, 0)$.

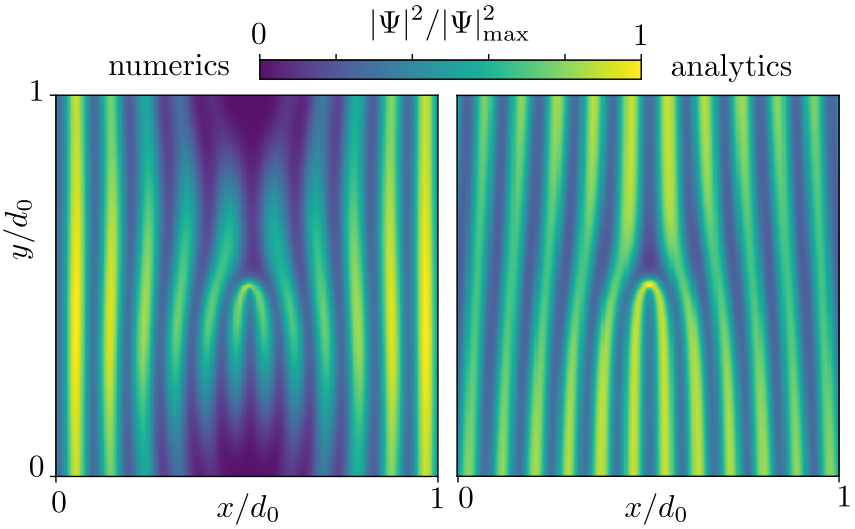

Figure 6.11: Comparison between numerical and analytical intensity profiles $|\Psi(x,y)|^2$, normalized to unit maximal value, for one of the two reflection-symmetric states in the zeroth Landau level. The parameter values are the same as in Fig. 6.4, which compared the other state.

The Hamiltonian commutes with the magnetic translation operator

$$\begin{aligned} \mathcal{T}_{\boldsymbol{n}} &= \begin{pmatrix} e^{ihn_y x/d_0} & 0 \\ 0 & e^{-ihn_y x/d_0} \end{pmatrix} T_{\boldsymbol{n}}\,, \\ T_{\boldsymbol{n}} \boldsymbol{r} T_{\boldsymbol{n}}^\dagger &= \boldsymbol{r} + d_0 \boldsymbol{n}\,. \end{aligned} \tag{6.44}$$

(The 2×2 matrix acts on the electron-hole degree of freedom.) The eigenvalue $e^{i\boldsymbol{k}\cdot\boldsymbol{n}}$ of the eigenstates defines the magnetic momentum $\boldsymbol{k} \in [0, 2\pi)^2$. At each value of $\boldsymbol{k}$ there are two independent zero-modes.

To make sure we are comparing the same state in the degenerate manifold we consider the operator product

$$\mathcal{P}_x = \begin{pmatrix} 0 & e^{\frac{1}{2}i\phi(\boldsymbol{r})} \\ e^{-\frac{1}{2}i\phi(\boldsymbol{r})} & 0 \end{pmatrix} \sigma_x P_x \begin{pmatrix} e^{-\frac{1}{2}i\phi(\boldsymbol{r})} & 0 \\ 0 & e^{\frac{1}{2}i\phi(\boldsymbol{r})} \end{pmatrix}, \tag{6.45}$$

with eigenvalues ± 1, which is a symmetry respected both by the analytic and by the numerical calculation. The operator P_x is the mirror symmetry operator in the x-direction,

$$P_x x P_x^\dagger = -x\,, \quad P_x y P_x^\dagger = y\,. \tag{6.46}$$

The magnetic momentum transforms under $\mathcal{P}_x$ as $k_x \mapsto -k_x$, $k_y \mapsto k_y$.

For the comparison we set $\boldsymbol{k} = 0$, which is invariant under the action of $\mathcal{P}_x$. Then we can take the two zero-modes obtained numerically to be eigenstates of $\mathcal{P}_x$, and compare them with the corresponding eigenstates obtained analytically. Those are

$$u_{\pm}(\boldsymbol{r}) = u(\boldsymbol{r}) \pm u'(\boldsymbol{r})\,, \tag{6.47}$$

which, in view of the fact that

$$f_n(-x, y) = f_n^*(x, y) \tag{6.48}$$

are eigenfunctions of $\mathcal{P}_x$ with eigenvalues ± 1. Figs. 6.4 and 6.11 compare the modulus squared of the $+1$ and -1 eigenstates of $\mathcal{P}_x$ respectively, with quite satisfactory correspondence.

7 Magnus effect on a Majorana zero-mode

7.1 Introduction

A topological superconductor can bind a Majorana fermion as a midgap state in the core of a magnetic vortex [8, 127, 128]. This Majorana zero-mode has been dubbed the "Zen particle" [129], because it embodies nothingness: it has zero charge, zero spin, zero energy, and zero mass [130–132]. It does have a definite chirality, set by the sign of the $\pm 2\pi$ winding of the superconducting phase around the vortex [109].

A superflow couples to the circulating phase, producing a sideways force on the vortex known as the Magnus force [133–136]. It was recently shown [137] that the superflow also acts on the zero-mode, causing a deconfinement transition when the Cooper pair momentum K exceeds the critical value Δ_0/v_F (with Δ_0 the superconducting gap and v_F the Fermi velocity).

Here we follow up on that work and investigate the dynamics of the transition, when the superconductor is quenched by the sudden application of a superflow. Computer simulations show that the Majorana zero-mode escapes from the vortex core as a wave packet with a constant velocity v_escape. A key result of our analysis is a calculation of the dependence of this quantity on K, Δ_0, and v_F, in a semiclassical approximation that is found to agree well with the simulations. That calculation is presented in Sec. 7.4, after we have formulated the problem (Sec. 7.2) and solved for the short-time dynamics (Sec. 7.3). We compare with computer simulations in Sec. 7.5 and conclude in Sec. 7.6.

7.2 Quenched topological superconductor

The effect of a superflow on a topological superconductor has been demonstrated experimentally [138] at the proximitized surface of a topological insulator [8]. We focus on that platform [11, 12], see Fig. 7.1, described

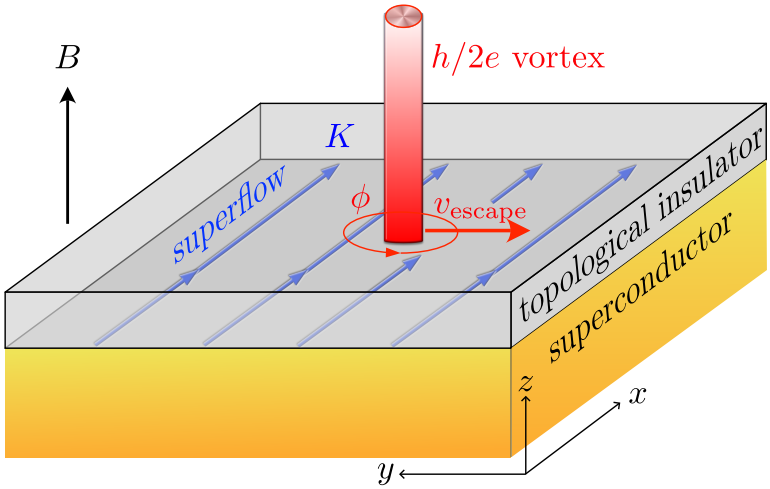

Figure 7.1: Schematic of a topological insulator with induced superconductivity (gap Δ_0) in a perpendicular magnetic field B. A vortex (red, with a 2π winding of the superconducting phase ϕ) binds a Majorana zero-mode. An in-plane supercurrent (blue arrows, Cooper pair momentum K) can deconfine the zero-mode, producing a Majorana fermion wave packet that escapes with velocity $v_{\rm escape}$ in a direction perpendicular to the superflow.

by the four-band Bogoliubov-De Gennes Hamiltonian

$$\begin{aligned}\mathcal{H}_0 = {} & v_{\rm F}(k_x\sigma_x + k_y\sigma_y)\nu_z - ev_{\rm F}(A_x\sigma_x + A_y\sigma_y)\nu_0 \\ & - \mu\sigma_0\nu_z + \Delta\sigma_0(\nu_x\cos\phi - \nu_y\sin\phi).\end{aligned} \tag{7.1}$$

The surface is in the x–y plane, the in-plane momentum is $\boldsymbol{k} = -i\partial_{\boldsymbol{r}}$. The electron charge is taken as $+e$, the Fermi velocity is $v_{\rm F}$ and $\hbar$ is set to unity. The Pauli matrices $\sigma_\alpha, \nu_\alpha$ act, respectively, on the spin and particle-hole degree of freedom. The corresponding 2×2 unit matrices are σ_0 and ν_0. An s-wave superconducting pair potential $\Delta e^{i\phi}$ couples electrons and holes. Time-reversal symmetry is broken by a perpendicular magnetic field B, with vector potential $\boldsymbol{A}$.

Charge-conjugation symmetry $\mathcal{C} = \sigma_y\nu_y\mathcal{K}$ is expressed by

$$\mathcal{C}\mathcal{H}_0\mathcal{C} = \sigma_y\nu_y\mathcal{H}_0^*\sigma_y\nu_y = -\mathcal{H}_0. \tag{7.2}$$

The complex conjugation operation $\mathcal{K}$ is taken in the real-space basis, so the momentum changes sign. When the Fermi energy $\mu = 0$ is at the

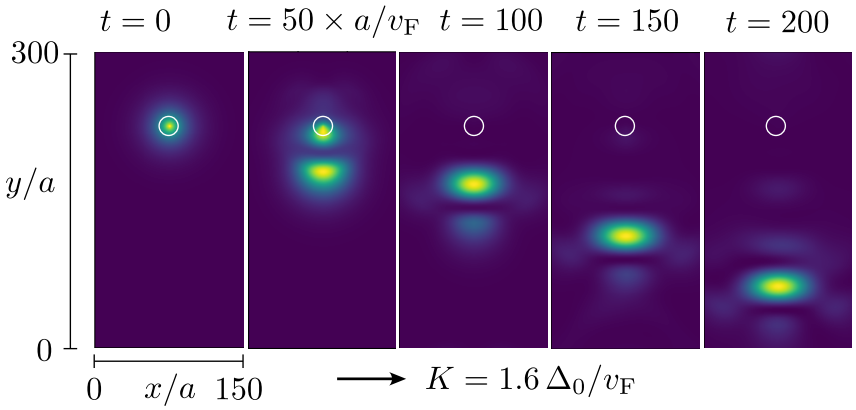

Figure 7.2: Majorana fermion wave packet that escapes from a vortex (white circle) in response to a quench of the superflow momentum K (in the x-direction). The images show a color scale plot of $|\Psi(x, y, t)|^2$ in the plane of the superconductor, at different times following the quench at $t = 0$. This is a numerical solution of the evolution equation (7.6), with Hamiltonian (7.5) discretized on a square lattice (lattice constant a, $\Delta_0 = 0.04\,\hbar v_F/a$, $B = (h/e)(302\,a)^{-2}$, $\mu = 0$). The initial condition at $t = 0$ is the Majorana zero-mode Ψ_+.

Dirac point there is additionally a chiral symmetry,

$$\sigma_z \nu_z \mathcal{H}_0 \sigma_z \nu_z = -\mathcal{H}_0. \tag{7.3}$$

We consider an $h/2e$ vortex at the origin. The gap Δ increases from 0 at the vortex core to Δ_0 outside, on the scale of the superconducting coherence length $\xi_0 = \hbar v_F/\Delta_0$. The superconducting phase $\phi(\boldsymbol{r})$ winds by $\pm 2\pi$ around the vortex, $e^{i\phi(\boldsymbol{r})} = r^{-1}(x \pm iy)$. In a strong type-II superconductor (ξ_0 much less than the London penetration length) the magnetic field is approximately uniform. We take the gauge where $\boldsymbol{A} = -By\hat{x}$.

The vortex contains a Majorana zero-mode, a charge neutral bound state with zero excitation energy [8]. Its wave function Ψ is an eigenstate of the charge conjugation operator $\mathcal{C}$. For $\mu = 0$ chiral symmetry demands that Ψ is also an eigenstate of $\sigma_z \nu_z$. The combination of the two symmetries enforces the form

$$\begin{aligned} \Psi_+ &= (e^{i\gamma}\psi_+, 0, 0, e^{-i\gamma}\psi_+), \\ \Psi_- &= (0, e^{i\gamma}\psi_-, e^{-i\gamma}\psi_-, 0), \end{aligned} \tag{7.4}$$

for a phase shift γ and a pair of real scalar functions $\psi_\pm(\boldsymbol{r})$. The sign of the vorticity selects either Ψ_+ or Ψ_-. An explicit solution [8, 109] of $\mathcal{H}_0\Psi = 0$ gives $\gamma = \pi/4$ and an exponential decay of $\psi_\pm$ on the scale of ξ_0.

The gapped surface is brought out of equilibrium by a superflow momentum quench $\boldsymbol{K}(t)$. The superflow exerts a Magnus force on the Majorana zero mode, which may cause it to escape from the vortex core [137]. A computer simulation of the escape is shown in Fig. 7.2.

The superflow momentum quench enters the Hamiltonian in the form

$$\mathcal{H} = \mathcal{H}_0 - \boldsymbol{K}\cdot\frac{\partial\mathcal{H}_0}{e\partial\boldsymbol{A}} = \mathcal{H}_0 + v_{\mathrm{F}}(\boldsymbol{K}\cdot\boldsymbol{\sigma})\nu_0, \tag{7.5}$$

in accord with Galilean invariance. We assume an instantaneous quench in the x-direction, $\boldsymbol{K}(t) = K\theta(t)\hat{x}$, so we seek the solution of the evolution equation

$$i\partial_t\Psi(t) = (\mathcal{H}_0 + v_{\mathrm{F}}K\sigma_x\nu_0)\Psi(t), \tag{7.6}$$

with initial condition $\Psi(0) = \Psi_\pm$ given by Eq. (7.4) The quench preserves both particle-hole and chiral symmetries.

The full superflow momentum

$$\boldsymbol{P}(\boldsymbol{r}) = \boldsymbol{p}_s(\boldsymbol{r}) + \boldsymbol{K} \tag{7.7}$$

includes also the contribution from the circulating momentum field $\boldsymbol{p}_s$ around the vortex cores. This divergence-free field has the gauge invariant expression [139]

$$\boldsymbol{p}_s(\boldsymbol{r}) = \tfrac{1}{2}\nabla\phi(\boldsymbol{r}) - e\boldsymbol{A}(\boldsymbol{r}). \tag{7.8}$$

For later use we note that the gauge transformation

$$\begin{aligned}\mathcal{H} &\mapsto e^{-i\phi(\boldsymbol{r})\nu_z/2}\mathcal{H}e^{i\phi(\boldsymbol{r})\nu_z/2}\\ &= v_{\mathrm{F}}(\boldsymbol{k}\cdot\boldsymbol{\sigma})\nu_z + v_{\mathrm{F}}(\boldsymbol{P}\cdot\boldsymbol{\sigma})\nu_0 - \mu\sigma_0\nu_z + \Delta\sigma_0\nu_x\end{aligned} \tag{7.9}$$

explicitly writes the Hamiltonian in terms of the full superflow momentum.

7.3 Short-time dynamics

For the initial time dependence we may truncate the Taylor expansion of the propagator $e^{-it\mathcal{H}}$,

$$\Psi(t) = e^{-it\mathcal{H}}\Psi_\pm = \sum_{n=0}^{\infty}\frac{(-it)^n}{n!}\mathcal{H}^n\Psi_\pm. \tag{7.10}$$

We calculate $\Psi(t)$ to order t^4, with the help of the polar-coordinate identity

$$(k_x \pm ik_y)f(r,\varphi) = \mp e^{\pm i\varphi}\left(\pm i\frac{\partial f}{\partial r} - r^{-1}\frac{\partial f}{\partial \varphi}\right), \tag{7.11}$$

and then compute the expectation value of the velocity,

$$\langle \dot{r}_\alpha(t)\rangle = \langle \Psi(t)|\partial\mathcal{H}/\partial k_\alpha|\Psi(t)\rangle = v_{\rm F}\langle\Psi(t)|\sigma_\alpha\nu_z|\Psi(t)\rangle. \tag{7.12}$$

We focus on the case $\mu = 0$ of chiral symmetry.

To simplify the calculation we note that the magnetic field only affects the dynamics on the scale of the magnetic length $l_m = \sqrt{\hbar/eB}$, which is large compared to the vortex size ξ_0 for magnetic fields small compared to the upper critical field of the superconductor. For the short-time dynamics we may ignore the magnetic field. In terms of the gap profile $\Delta(r)$ the scalar function $\psi_\pm$ in the initial state (7.4) is then given by [8, 109]

$$\psi_+(r) = \psi_-(r) = c\exp\left(-v_{\rm F}^{-1}\int_0^r dr'\Delta(r')\right), \tag{7.13}$$

with c a normalization constant.

A simple closed-form expression results for a constant $\Delta \equiv \Delta_0$,

$$\langle \dot{x}(t)\rangle = -2v_{\rm F}^2\Delta_0^2 K t^3\cos 2\gamma + \mathcal{O}(t^5), \tag{7.14a}$$

$$\langle \dot{y}(t)\rangle = -2v_{\rm F}^2 K t + \tfrac{4}{3}v_{\rm F}^4K^3t^3 + \tfrac{2}{3}v_{\rm F}^2\Delta_0^2Kt^3(10 - 9\sin 2\gamma) + \mathcal{O}(t^5). \tag{7.14b}$$

These are the formulas for $+2\pi$ vorticity (initial condition Ψ_+); for -2π vorticity (initial condition Ψ_-) the component $\langle\dot{x}\rangle$ is unchanged while $\langle\dot{y}\rangle$ changes sign.

The zero-mode has $\gamma = \pi/4$, hence the motion is fully in the y-direction, with initial velocity

$$\langle \dot{y}(t)\rangle = \pm 2v_{\rm F}^2 Kt\big(-1 + \tfrac{1}{3}t^2(\Delta_0^2 + 2v_{\rm F}^2K^2) + \mathcal{O}(t^4)\big), \tag{7.15}$$

for $\pm 2\pi$ vorticity. Because of the dependence on the vorticity, we interpret the initial acceleration $\pm 2v_{\rm F}^2K$ as a manifestation of the Magnus force acting on the zero-mode.

One may wonder whether the Lorentz force, which we have ignored in this calculation, would deflect the particle away from the y-axis. This is not the case, chiral symmetry enforces $\langle\dot{x}(t)\rangle = 0$ for all $t > 0$ when $\gamma = \pi/4$, see App. 7.A.

7.4 Semiclassical calculation of the escape velocity

A semiclassical approximation will allow us to obtain a simple analytical expression for the velocity at which the Majorana fermion escapes from the vortex core. For simplicity, we set $\mu = 0$, so chiral symmetry applies.

Quite generally, a wave packet at position $\boldsymbol{r}$ and with wave vector $\boldsymbol{k}$ has the semiclassical equations of motion [140, 141]

$$\dot{\boldsymbol{r}} = \partial_{\boldsymbol{k}} E - \dot{\boldsymbol{k}} \times (\partial_{\boldsymbol{k}} \times \mathcal{A}) + (\dot{\boldsymbol{r}} \cdot \partial_{\boldsymbol{r}})\mathcal{A} - \partial_{\boldsymbol{k}}(\boldsymbol{a} \cdot \dot{\boldsymbol{r}}) \tag{7.16a}$$

$$\dot{\boldsymbol{k}} = -\partial_{\boldsymbol{r}} E + \dot{\boldsymbol{r}} \times (\partial_{\boldsymbol{r}} \times \boldsymbol{a}) - (\dot{\boldsymbol{k}} \cdot \partial_{\boldsymbol{k}})\boldsymbol{a} + \partial_{\boldsymbol{r}}(\mathcal{A} \cdot \dot{\boldsymbol{k}}). \tag{7.16b}$$

The energy $E(\boldsymbol{r}, \boldsymbol{k})$ is an eigenvalue of the 4×4 matrix $H(\boldsymbol{r}, \boldsymbol{k})$, obtained from the Hamiltonian $\mathcal{H}$ by treating $\boldsymbol{r}$ and $\boldsymbol{k}$ as parameters — not as operators. The corresponding eigenfunction $|u(\boldsymbol{r}, \boldsymbol{k})\rangle$ is a rank-4 spinor, normalized to unity, $\langle u|u\rangle = 1$.

The fields $\mathcal{A}$ and $\boldsymbol{a}$ are defined by the connections

$$\mathcal{A}(\boldsymbol{r}, \boldsymbol{k}) = \langle u(\boldsymbol{r}, \boldsymbol{k})| i\partial_{\boldsymbol{k}} |u(\boldsymbol{r}, \boldsymbol{k})\rangle, \tag{7.17a}$$

$$\boldsymbol{a}(\boldsymbol{r}, \boldsymbol{k}) = \langle u(\boldsymbol{r}, \boldsymbol{k})| i\partial_{\boldsymbol{r}} |u(\boldsymbol{r}, \boldsymbol{k})\rangle. \tag{7.17b}$$

The state $|u\rangle$ is defined up to a complex phase factor. If $|u\rangle \mapsto e^{if(\boldsymbol{r},\boldsymbol{k})}|u\rangle$ the connections transform as $\mathcal{A} \mapsto \mathcal{A} - \partial_{\boldsymbol{k}} f$ and $\boldsymbol{a} \mapsto \boldsymbol{a} - \partial_{\boldsymbol{r}} f$. These two transformations leave the right-hand-side of Eq. (7.16) unchanged.

We apply this general formalism to the Hamiltonian (7.9), to ensure that the full gauge invariant superflow momentum appears in the equations of motion. Diagonalization of $H(\boldsymbol{r}, \boldsymbol{k})$ for $\mu = 0$ gives four eigenstates $|u_n(\boldsymbol{r}, \boldsymbol{k})\rangle$ with eigenvalues

$$E_n(\boldsymbol{r}, \boldsymbol{k}) = s_n \sqrt{v_{\mathrm{F}}^2 P(\boldsymbol{r})^2 + \Delta(\boldsymbol{r})^2 + v_{\mathrm{F}}^2 k^2 + 2 s_n' v_{\mathrm{F}} \sqrt{P(\boldsymbol{r})^2 \Delta(\boldsymbol{r})^2 + v_{\mathrm{F}}^2 \big(\boldsymbol{k} \cdot \boldsymbol{P}(\boldsymbol{r})\big)^2}},$$
$$\{s_1, s_1'\} = \{+,+\}, \;\; \{s_2, s_2'\} = \{-,+\}, \;\; \{s_3, s_3'\} = \{+,-\}, \;\; \{s_4, s_4'\} = \{-,-\}. \tag{7.18}$$

We find that the connections (7.17) do not contribute to the equations of motion (7.16), because they are given by the gradient of a scalar field,

$$\mathcal{A}_n(\boldsymbol{r}, \boldsymbol{k}) = \partial_{\boldsymbol{k}} f_n(\boldsymbol{r}, \boldsymbol{k}), \;\; \boldsymbol{a}_n(\boldsymbol{r}, \boldsymbol{k}) = \partial_{\boldsymbol{r}} f_n(\boldsymbol{r}, \boldsymbol{k}), \tag{7.19}$$

$$f_n = \tfrac{1}{2} \arctan\left(\frac{P^2 + s_n' \sqrt{(\boldsymbol{k} \cdot \boldsymbol{P})^2 + P^2 \Delta^2 / v_{\mathrm{F}}^2}}{k_x P_y - k_y P_x} \right) - \tfrac{1}{2} \arctan(P_y / P_x). \tag{7.20}$$

The semiclassical dynamics is therefore fully determined by the energy landscape,

$$\dot{\boldsymbol{r}} = \partial_{\boldsymbol{k}} E_n, \quad \dot{\boldsymbol{k}} = -\partial_{\boldsymbol{r}} E_n. \tag{7.21}$$

We consider a rotationally symmetric vortex, $\Delta(\boldsymbol{r}) = \Delta(r)$, $\boldsymbol{P}(\boldsymbol{r}) = \boldsymbol{K}\hat{x} + p_s(r)\hat{z}\times\hat{\boldsymbol{r}}$, so that $E(-x, y, -k_x, k_y) = E(x, y, k_x, k_y)$. A trajectory that starts out with $x = 0$, $k_x = 0$ at $t = 0$ then will retain these values for $t > 0$. The motion along the y-axis is determined by the equations of motion

$$\dot{y} = \partial_{k_y} E_n = v_{\rm F}^2 k_y / E_n, \tag{7.22a}$$

$$\dot{k}_y = -\partial_y E_n = -\frac{1}{2E_n}\frac{d}{dy}\left[s_n' v_{\rm F} P(y) + \Delta(y)\right]^2. \tag{7.22b}$$

We denote $\Delta(x = 0, y) \equiv \Delta(y)$ and $P(x = 0, y) \equiv P(y)$.

Since $dE_n/dt = 0$, the energy E_n is equal to its value at $t = 0$. Assuming $\Delta(0) = 0$ and $P(0) = |K|$ (vanishing pair potential and no circulating superflow deep inside the vortex core), we have $E_n = s_n v_{\rm F}|K|$.

Far outside of the core, where $\Delta \approx \Delta_0$ and $P \approx |K|$ are both y-independent, one has $\dot{k}_y = 0$. The terminal k_y should satisfy

$$v_{\rm F}^2 K^2 = E_n^2 \Rightarrow v_{\rm F}^2 k_y^2 = -\Delta_0^2 - 2s_n' v_{\rm F}|K|\Delta_0, \tag{7.23}$$

which has a real solution for $s_n' = -1$ if $v_{\rm F}|K| > \Delta_0/2$. That is the condition for escape of the Majorana fermion. The escape velocity is given by

$$|v_{\rm escape}| = |K|^{-1}\sqrt{2v_{\rm F}|K|\Delta_0 - \Delta_0^2}. \tag{7.24}$$

The maximum $|v_{\rm escape}| = v_{\rm F}$ is reached at $|K| = \Delta_0/v_{\rm F}$.

Notice that the quenched superconductor supports a quasiparticle escape even though the excitation gap has not closed: the reduced gap $\Delta_{\rm eff} = \Delta_0 - v_{\rm F}|K|$ only closes for $v_{\rm F}|K| > \Delta_0$, while quasiparticle escape is possible for $v_{\rm F}|K| > \Delta_0/2$. The reason is that the quench gives a finite energy $v_{\rm F}|K|$ to the quasiparticle, so escape becomes possible when $v_{\rm F}|K| > \Delta_{\rm eff} \Rightarrow v_{\rm F}|K| > \Delta_0/2$.

The escaping wave packet is a superposition of the two states $|u_n\rangle$ with $s_n' = -1$ and $s_n = \pm 1$. They satisfy the same equation of motion

$$\begin{aligned} &\ddot{y} = -v_{\rm F}^2 U'(y), \\ &U(y) = \frac{1}{2K^2}\Big(\big[P(y) - \Delta(y)/v_{\rm F}\big]^2 - K^2\Big), \end{aligned} \tag{7.25}$$

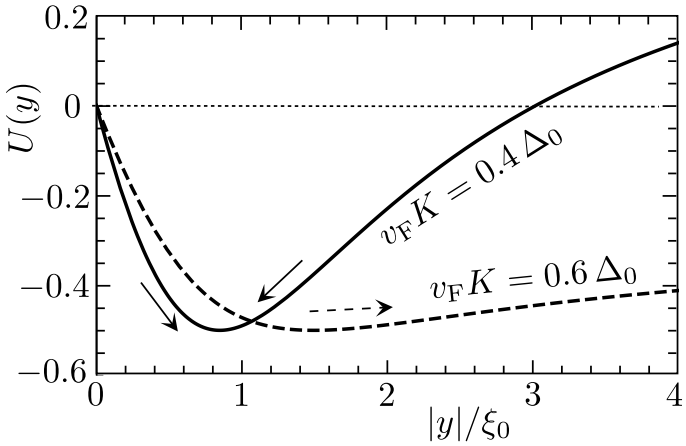

Figure 7.3: Plot of the potential $U(y)$ that governs the equation of motion (7.25) of the wave pet, calculated for the gap and superflow velocity profiles (7.26). The arrows indicate the oscillatory motion for $v_{\rm F}|K| < \Delta_0/2$ and the escape to infinity for $v_{\rm F}|K| > \Delta_0/2$. The direction in which the wave packet escapes is minus the sign of K times the sign of the vorticity.

with initial conditions $\dot{y}(0) = 0$ and $y(0)$ infinitesimal (needed to avoid the discontinuous derivative $\Delta'(y)$ at $y = 0$) [1]. This is the frictionless motion in the potential landscape $U(y)$, plotted in Fig. 7.3 for the functional forms

$$\Delta(y) = \frac{\Delta_0|y|}{\sqrt{y^2+\xi_0^2}}, \quad P(y) = |K| + \frac{|y|/2}{y^2+\xi_0^2} \tag{7.26}$$

appropriate for a vortex with coherence length ξ_0 much smaller than the London penetration length [139, 142].

For $v_{\rm F}|K| > \Delta_0/2$ one has $U(\infty) < U(0)$ so the motion escapes to infinity, with a constant terminal velocity (7.24), for $v_{\rm F}|K| < \Delta_0/2$ the motion is oscillatory.

The two states $s_n = \pm 1$, at energies $\pm v_{\rm F}|K|$, are related by particle-hole symmetry, they have the same position but opposite momentum. The semiclassical calculation neglects interference of the positive and negative energy states, which is reliable for the long-time dynamics outside of the vortex core, when the momentum difference is large and interference effects average out. In contrast, inside the vortex core the two states both

[1] The sign of the infinitesimal $y(0)$ for the equation of motion (7.25) is minus the sign of K times the sign of the vorticity, in accord with the short-time dynamics (7.15).

still have momentum approximately equal to zero, and their interference cannot be neglected.

7.5 Computer simulations

We have simulated the wave packet dynamics by discretizing the Bogoliubov-De Gennes Hamiltonian (7.1) on a square lattice (lattice constant a),

$$\begin{aligned} H = {} & (v_{\mathrm{F}}/a)(\sigma_x \sin ak_x + \sigma_y \sin ak_y)\nu_z - \mu\sigma_0\nu_z \\ & + M(k)\sigma_z\nu_0 - ev_{\mathrm{F}}(A_x\sigma_x + A_y\sigma_y)\nu_0 \\ & + \Delta\sigma_0(\nu_x \cos\phi - \nu_y \sin\phi) + v_{\mathrm{F}}K\sigma_x\nu_0, \qquad (7.27\mathrm{a}) \\ M(k) = {} & M_0 - (M_1/a^2)(2 - \cos ak_x - \cos ak_y), \qquad (7.27\mathrm{b}) \end{aligned}$$

and evolving the zero-mode wave function via a finite-difference algorithm. The $M(k)$ term in Eq. (7.27) includes the effect of a small coupling between the top and bottom surfaces of the topological insulator of Fig. 7.1. As in Ref. 137 we set $M_0 = 0$, to avoid the opening of a gap at $\boldsymbol{k} = 0$, but retain a nonzero $M_1 = 0.2\, av_{\mathrm{F}}$ in order to eliminate the fermion doubling at $\boldsymbol{k} = (\pi/a, \pi/a)$.

We take a uniform magnetic field $B\hat{z} = \nabla \times \boldsymbol{A}$, appropriate for a strong type-II superconductor. The vortex array has a pair of $h/2e$ vortices in a magnetic unit cell of size $d_0 \times d_0$, with $d_0 = 302\, a$ (corresponding to a magnetic field $B = h/ed_0^2$.) The phase field $\phi(\boldsymbol{r})$ winds by 2π around each vortex, at position $\boldsymbol{R}_n$, as expressed by

$$\nabla \times \nabla\phi(\boldsymbol{r}) = 2\pi\hat{z}\textstyle\sum_n \delta(\boldsymbol{r} - \boldsymbol{R}_n), \quad \nabla^2\phi = 0. \qquad (7.28)$$

For the pair potential in a vortex core we take the gap profile $\Delta(r) = \Delta_0 \tanh(r/r_0)$, with $\Delta_0 = 0.2\, v_{\mathrm{F}}/a$. The core size r_0 is of order $\xi_0 = v_{\mathrm{F}}/\Delta_0$, but for the sake of comparison with the semiclassics (which assumes a smooth gap profile) we will also consider larger values of r_0. The gap $\Delta(r)$ is saturated at Δ_0 for $r > 70\, a$, to ensure that the vortex core is fully contained within a single magnetic unit cell. We follow the dynamics of the wave packet on a time scale that is sufficiently short that only a single vortex plays a dominant role. To avoid interference from the other vortex we set its core size to zero.

We use the package Tkwant for the calculations [85, 143]. See App. 7.B for details on the simulation.

In Fig. 7.4 we show the time dependence of the propagation of the wave packet along the y-axis, following a superflow quench at $t = 0$. We compare $\int |\Psi(x, y, t)|^2\, dx$ from the simulation with $y(t)$ from the semiclassical

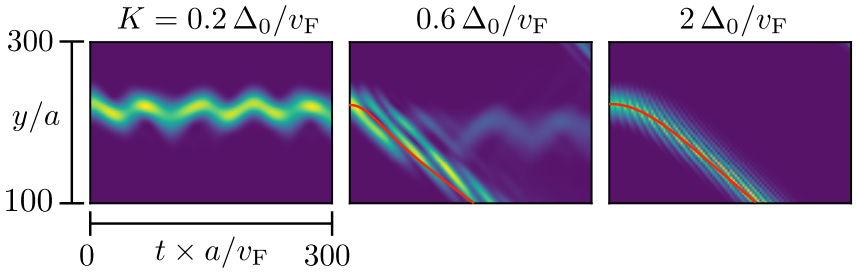

Figure 7.4: Propagation of the zero-mode along the y-axis after the superflow momentum quench at $t = 0$. The color scale shows the density profile $\int |\Psi(x, y, t)|^2\, dx$ following from the computer simulation ($\Delta_0 = 0.2\, v_\mathrm{F}/a$, $r_0 = 40\, a$, $B = (h/e)(302\, a)^{-2}$). The red curve results from integration of the semiclassical equation of motion (7.25), for the same $\Delta(r) = \Delta_0 \tanh(r/r_0)$ gap profile as in the numerics.

equation of motion (7.25) [2]. The comparison has no adjustable parameters. As anticipated, the agreement is good outside of the vortex core ($K \gtrsim \Delta_0/v_\mathrm{F}$), where the interference of the positive and negative energy wave packets can be neglected. The oscillatory motion of the wave packet inside the vortex, for small K, is not well described by the semiclassics.

Fig. 7.5 compares the escape velocity obtained from the simulation with the semiclassical formula (7.24). The numerical data nicely approaches the semiclassics for larger and larger core sizes.

7.6 Conclusion

In summary, we have investigated the dynamics of the Majorana delocalization transition reported in Ref. 137. A supercurrent can be used to extract a Majorana fermion from the zero-mode bound to a vortex core. The extraction process is governed by an effective potential well, see Fig. 7.3, which allows for escape with a constant terminal velocity v_escape once the supercurrent exceeds a critical value. A simple semiclassical calculation of this velocity agrees well with computer simulations.

The escape of the Majorana fermion should be observable by scanning probe spectroscopy, as a current pulse when the probe is positioned near a vortex, at right angles from the superflow. Close to the deconfinement

[2] For the comparison beween numerics and semiclassics in Fig. 7.4 it makes no significant difference whether we take $P(y) \equiv K$ or include the near-field contribution from the circulating superfluid momentum, as in Eq. (7.26).

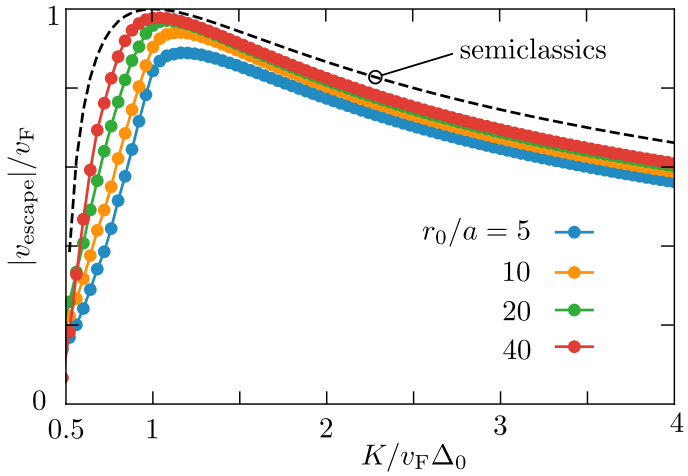

Figure 7.5: Escape velocity of a zero-mode wave packet from the vortex core, as a function of the superflow momentum K. The data points follow from the computer simulation, for different core sizes r_0 (at fixed $\Delta_0 = 0.2\, v_{\rm F}/a$). The black dashed curve is the semiclassical result (7.24).

transition the escape velocity will be much smaller than the Fermi velocity $v_{\rm F} \approx 10^5\,{\rm m/s}$ (see Fig. 7.5), which should make the observation more feasible.

The internal degree of freedom of the Majorana zero-mode that couples to the superflow via the Magnus effect is the chirality — zero-modes of opposite chirality escape from the vortex in opposite directions. The conformal field theory of non-Abelian anyons associates a "topological spin" to a Majorana zero-mode [144–146]. As a topic for future research we ask whether there is an analogous Magnus effect for the topological spin. We note that the phase shift γ in the Majorana wave function (7.4) affects the direction in which the superflow drives the quasiparticle, see Eq. (7.14). The motion is strictly perpendicular to the superflow only for $\gamma = \pi/4$. That this also happens to be the value of the topological spin may or may not be accidental.

Appendices

7.A Chiral symmetry prevents lateral deflection by the Lorentz force

Fig. 7.2 shows that the Majorana fermion escapes from the vortex along the y-direction, perpendicular to the superflow. We address the question why the motion is not bent in the x-direction by the Lorentz force. Since electrons and holes are deflected in *the same* direction by the Lorentz force, charge-neutrality of the quasiparticle does not prevent the deflection. Chiral symmetry is essential.

To demonstrate this, we calculate the expectation value at $\mu = 0$ of the x-component of the velocity operator,

$$\langle \dot{x}(t) \rangle = v_{\rm F} \langle \Psi(0) | e^{i\mathcal{H}t} \sigma_x \nu_z e^{-i\mathcal{H}t} | \Psi(0) \rangle. \tag{7.29}$$

The superconducting vortex at the origin has pair potential $\Delta(r)e^{\pm i\phi}$, in polar coordinates (r, ϕ), with a rotationally symmetric amplitude $\Delta(r)$ and a $\pm 2\pi$ vorticity. The magnetic field $B(r)\hat{z}$ is also assumed to be rotationally symmetric, with vector potential $\boldsymbol{A}(\boldsymbol{r}) = g(r)(-y, x, 0)$ [so that $B(r) = 2g(r) + rg'(r)$].

The initial state $\Psi(0) = \Psi_\pm$ is a zero-mode bound to the vortex core, given by [8, 109]

$$\begin{aligned}
\Psi_+ &= c_+ e^{+\chi(\boldsymbol{r})} \exp\left(-v_{\rm F}^{-1} \int_0^r \Delta(r')dr' \right) \begin{pmatrix} e^{i\pi/4} \\ 0 \\ 0 \\ e^{-i\pi/4} \end{pmatrix}, \\
\Psi_- &= c_- e^{-\chi(\boldsymbol{r})} \exp\left(-v_{\rm F}^{-1} \int_0^r \Delta(r')dr' \right) \begin{pmatrix} 0 \\ e^{i\pi/4} \\ e^{-i\pi/4} \\ 0 \end{pmatrix},
\end{aligned} \tag{7.30}$$

with $c_\pm$ a normalization constant and $\chi(\boldsymbol{r})$ chosen such that

$$\partial_y \chi = eA_x, \;\; \partial_x \chi = -eA_y. \tag{7.31}$$

Note that $\chi(-x,y)=\chi(x,y)$.

We introduce the operator $\mathcal{P}_x$ which reflects $x\mapsto -x$, $k_x\mapsto -k_x$. Its action on the Hamiltonian $\mathcal{H}=\mathcal{H}_0+v_{\rm F}K\sigma_x\nu_0$ is given by

$$\mathcal{P}_x\mathcal{H}\mathcal{P}_x=\sigma_x\nu_y\mathcal{H}\sigma_x\nu_y \ \text{ if } \ \mu=0, \tag{7.32}$$

see Eq. (7.1). The zero-mode (7.30) is unchanged upon reflection, $\Psi_\pm(x,y)=\Psi_\pm(-x,y)$, and moreover

$$\Psi_\pm=-\sigma_x\nu_y\Psi_\pm. \tag{7.33}$$

These identities imply that

$$\mathcal{P}_x e^{-i\mathcal{H}t}\Psi_\pm=-\sigma_x\nu_y e^{-i\mathcal{H}t}\Psi_\pm. \tag{7.34}$$

We now calculate, using also $\sigma_x\nu_z=\mathcal{P}_x\sigma_x\nu_z\mathcal{P}_x$, the expectation value (7.29),

$$\begin{aligned}\langle\dot{x}(t)\rangle &= v_{\rm F}\langle\Psi_\pm|e^{i\mathcal{H}t}\sigma_x\nu_z e^{-i\mathcal{H}t}|\Psi_\pm\rangle\\ &= v_{\rm F}\langle\Psi_\pm|e^{i\mathcal{H}t}\mathcal{P}_x\sigma_x\nu_z\mathcal{P}_x e^{-i\mathcal{H}t}|\Psi_\pm\rangle\\ &= v_{\rm F}\langle\Psi_\pm|e^{i\mathcal{H}t}(-\sigma_x\nu_y)(\sigma_x\nu_z)(-\sigma_x\nu_y)e^{-i\mathcal{H}t}|\Psi_\pm\rangle\\ &= -v_{\rm F}\langle\Psi_\pm|e^{i\mathcal{H}t}\sigma_x\nu_z e^{-i\mathcal{H}t}|\Psi_\pm\rangle\\ &= -\langle\dot{x}(t)\rangle \Rightarrow \langle\dot{x}(t)\rangle\equiv 0.\end{aligned} \tag{7.35}$$

The velocity component in the x-direction has zero expectation value for all t, there is no lateral deflection by the Lorentz force at $\mu=0$.

7.B Details of the numerical calculations

The velocity operator is given by $\boldsymbol{v}=\partial H/\partial\boldsymbol{k}$, with H the tight-binding Hamiltonian (7.27). (In the continuous limit this reduces to $v_i=v_{\rm F}\sigma_i\nu_z$.) We compute the expectation value $\langle v_y\rangle(t)$ as function of time. As a consistency check we show in Fig. 7.6 the short-time dynamics together with the analytical result (7.15). For longer times the wave packet may escape from the vortex core. We determine the escape velocity by averaging $\langle v_y\rangle(t)$ over a brief time interval, see Fig. 7.7.

This is all data for $\mu=0$, when the expectation value of the velocity component v_x parallel to the superflow vanishes. A nonzero μ breaks chiral symmetry and introduces a nonzero $\langle v_x\rangle$, see Fig. 7.8. The sign of μ dictates the direction of the deflection away from the y-axis.

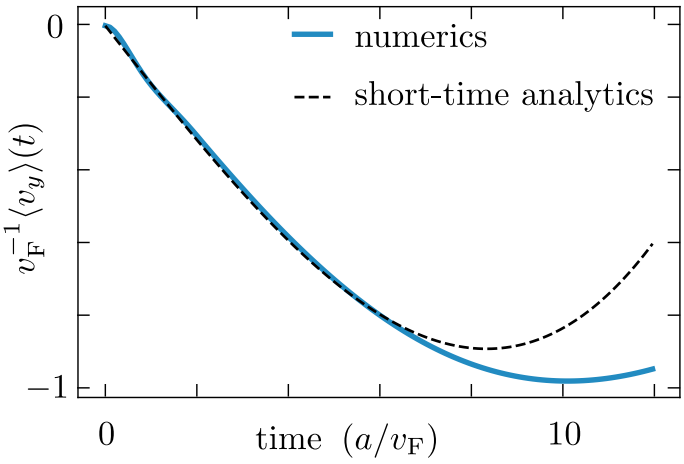

Figure 7.6: Initial time dependence of the expectation value of the velocity v_y of the Majorana wave packet (perpendicular to the superflow), for $\Delta_0 = 0.04\, v_F/a$, $K = 2\Delta_0/v_F$, in the limit $r_0 \to 0$ of a small vortex core. The dashed curve is the analytical result from Eq. (7.15).

The short-time result (7.14) indicates that a deflection in the x-direction is also possible without breaking chiral symmetry, if the initial wave packet has a phase shift $\gamma \neq \pi/4$. Such a phase shift between the electron and hole components could be induced by a voltage pulse. In Fig. 7.9 we show that the numerics confirms this analytical expectation.

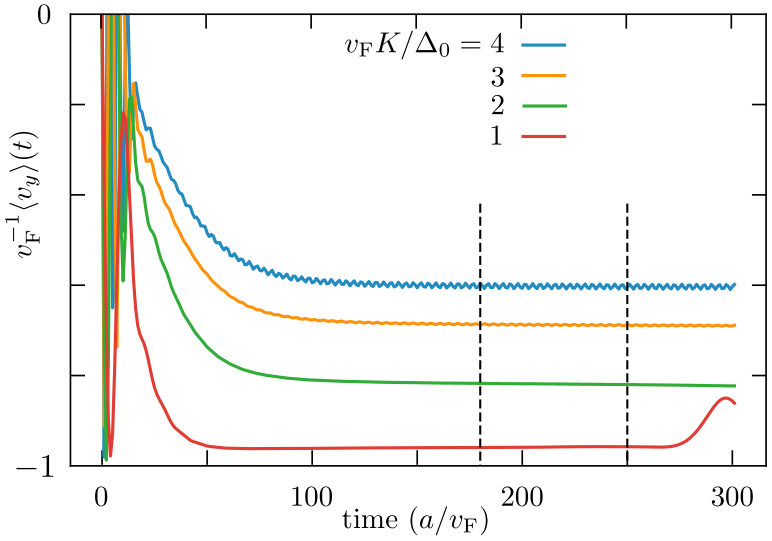

Figure 7.7: Time dependence of the velocity when the Majorana wave packet is driven out of the vortex core by the Magnus force. Four values of the superflow momentum K are shown at fixed $\Delta_0 = 0.2\,v_F/a$. The average over the time interval between the dashed lines is the escape velocity plotted in Fig. 7.5 (green curve, for $r_0 = 20\,a$). For much shorter times the wave packet is still trapped in the vortex core. For longer times the wave packet reaches the boundary of the magnetic unit cell.

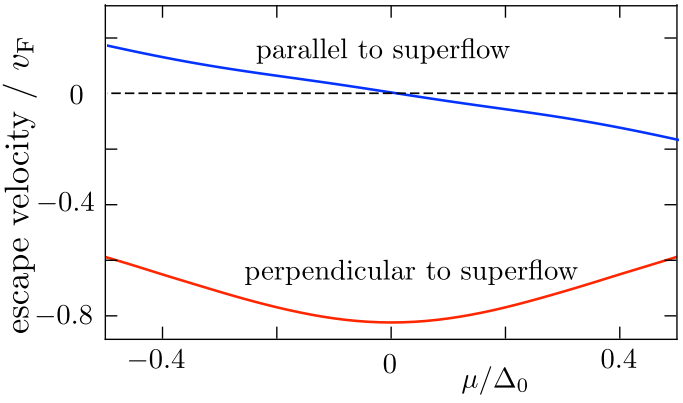

Figure 7.8: Dependence of the direction of the escape velocity on the chemical potential μ (for fixed $\Delta_0 = 0.2\,v_F/a$, $K = 2\Delta_0/v_F$, and vortex core size $r_0 = 40\,a$).

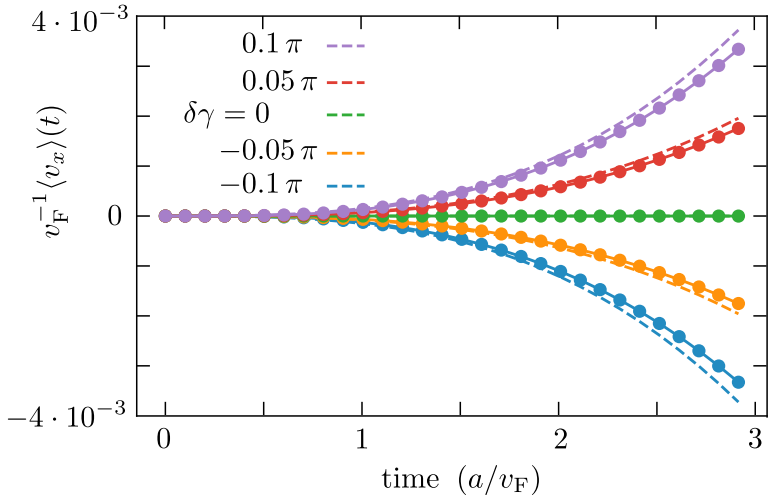

Figure 7.9: Dependence of the velocity v_x parallel to the superflow on the phase shift $\gamma = \pi/4 + \delta\gamma$ between the electron and hole components of the initial wave packet (for $\Delta_0 = 0.04\, v_{\mathrm{F}}/a$, $K = 2\Delta_0/v_{\mathrm{F}}$, $r_0 \to 0$). This is data for $\mu = 0$, the deflection in the x-direction happens when γ is pushed away from $\pi/4$ by an initial voltage pulse. The solid curves are numerical results, the dashed curves are the short-time analytics (7.14).

Bibliography

[1] A. H. Castro Neto, F. Guinea, N. M. R. Peres, K. S. Novoselov, and A. K. Geim, *The electronic properties of graphene*, Rev. Mod. Phys. **81**, 109 (2009).

[2] M. I. Katsnelson, *Graphene: carbon in two dimensions*, materialstoday **10**, 20 (2007).

[3] J. Bardeen, L. N. Cooper, and J. R. Schrieffer, *Theory of Superconductivity*, Phys. Rev. **108**, 1175 (1957).

[4] E. Majorana, *Teoria simmetrica dell'elettrone e del positrone*, Il Nuovo Cimento **14**, 171-184 (2010).

[5] J. K. Asbóth , L. Oroszlány and A. Palyi, *A Short Course on Topological Insulators*, Lect. Notes Phys **919**, (2016).

[6] T. Meng and L. Balents, *Weyl superconductors*, Phys. Rev. B **86**, 054504 (2012). *Erratum:* Phys. Rev. B **96**, 019901 (2017).

[7] G. Bednik, A. A. Zyuzin, and A. A. Burkov, *Superconductivity in Weyl metals*, Phys. Rev. B **92**, 035153 (2015).

[8] Liang Fu and C. L. Kane, *Superconducting proximity effect and Majorana fermions at the surface of a topological insulator*, Phys. Rev. Lett. **100**, 096407 (2008).

[9] G. Chang, B. J. Wieder, F. Schindler, D. S. Sanchez, I. Belopolski, S.-M. Huang, B. Singh, D. Wu, T. Neupert, T.-R. Chang, S.-Y. Xu, H. Lin, and M. Z. Hasan, *Topological quantum properties of chiral crystals*, Nature Mat. **17**, 978 (2018).

[10] C. Shekhar, *Chirality meets topology*, Nature Mat. **17**, 953 (2018).

[11] M. Z. Hasan and C. L. Kane, *Colloquium: Topological insulators*, Rev. Mod. Phys. **82**, 3045 (2010).

[12] Xiao-Liang Qi and Shou-Cheng Zhang, *Topological insulators and superconductors*, Rev. Mod. Phys. **83**, 1057 (2011).

[13] B. Yan and C. Felser, *Topological Materials: Weyl Semimetals*, Annu. Rev. Condens. Matter Phys. **8**, 337 (2017).

[14] L. D. Landau and E. M. Lifshitz *Quantum Mechanics: Non-Relativistic Theory*, Course of Theoretical Physics **3**, (1965).

[15] A.A. Abrikosov, *The magnetic properties of superconducting alloys*, Journal of Physics and Chemistry of Solids **3**, 199 (1957).

[16] A. S. Mel'nikov, *Quantization of the quasiparticle spectrum in the mixed state of d-wave superconductors*, J. Phys. Condens. Matter **11**, 4219 (1999).

[17] L. Alvarez-Gaumé, *Supersymmetry and the Atiyah-Singer index theorem*, Communications in Mathematical Physics **90**, 161 (1983).

[18] M. Filoche and S. Mayboroda, *Universal mechanism for Anderson and weak localization*, PNAS **109**, 14761 (2012).

[19] M. Filoche and S. Mayboroda, *The landscape of Anderson localization in a disordered medium*, Contemp. Math. **601**, 113 (2013).

[20] D. N. Arnold, G. David, D. Jerison, S. Mayboroda, and M. Filoche, *Effective confining potential of quantum states in disordered media*, Phys. Rev. Lett. **116**, 056602 (2016).

[21] S. Steinerberger, *Localization of quantum states and landscape functions*, Proc. Amer. Math. Soc. **145**, 2895 (2017).

[22] M. Filoche, M. Piccardo, Y.-R. Wu, C.-K. Li, C. Weisbuch, and S. Mayboroda, *Localization landscape theory of disorder in semiconductors. I. Theory and modeling*, Phys. Rev. B **95**, 144204 (2017).

[23] M. Piccardo, C.-K. Li, Y.-R. Wu, J. S. Speck, B. Bonef, R. M. Farrell, M. Filoche, L. Martinelli, J. Peretti, and C. Weisbuch, *Localization landscape theory of disorder in semiconductors. II. Urbach tails of disordered quantum well layers*, Phys. Rev. B **95**, 144205 (2017)

[24] C.-K. Li, M. Piccardo, L.-S. Lu, S. Mayboroda, L. Martinelli, J. Peretti, J. S. Speck, C. Weisbuch, M. Filoche, and Y.-R. Wu, *Localization landscape theory of disorder in semiconductors. III. Application to carrier transport and recombination in light emitting diodes*, Phys. Rev. B **95**, 144206 (2017).

[25] Y. Chalopin, F. Piazza, S. Mayboroda, C. Weisbuch, and M. Filoche *Universality of fold-encoded localized vibrations in enzymes*, arXiv:1902.09939

[26] D. Arnold, D. Guy, M. Filoche, D. Jerison, and S. Mayboroda, *Computing spectra without solving eigenvalue problems*, SIAM J. Scientif. Comput. **41**, B69 (2019).

[27] E. M. Harrell II and A. V. Maltsev, *Localization and landscape functions on quantum graphs*, arXiv:1803.01186.

[28] C. W. J. Beenakker, *Hidden landscape of an Anderson insulator*, J. Club Cond. Matt. (August, 2019,

[29] A. Ostrowski, *Über die Determinanten mit überwiegender Hauptdiagonale*, Comment. Mathemat. Helvet. **10**, 69 (1937). The comparison inequality is on page 71.

[30] A. Ostrowski, *Determinanten mit überwiegender Hauptdiagonale und die absolute Konvergenz von linearen Iterationsprozessen*, Comment. Mathemat. Helvet. **30**, 175 (1956).

[31] Ostrowski originally used the name "companion matrix" (*Begleitmatrix*), which now refers to a different construction. The notation $\langle H \rangle$ for the comparison matrix of H is common in the mathematical literature, but to avoid confusion with the physics notation for expectation value we use $\overline{H}$ instead. One more piece of nomenclature: If $\overline{H}$ is positive-definite, then it is called an M-matrix while H is called an H-matrix.

[32] For background on comparison matrices, see A. Berham and R. J. Plemmons, *Nonnegative Matrices in the Mathematical Sciences* (SIAM, 1994).

[33] The discretization (2.9) is appropriate near the bottom of the tight-binding band at $p = 0$. Near the top of the band at $p = \pi/a$ a different discretization produces a different landscape function, as discussed by M. L. Lyra, S. Mayboroda, and M. Filoche, *Dual landscapes in Anderson localization on discrete lattices*, EPL **109**, 47001 (2015).

[34] G. Giovannetti, P. A. Khomyakov, G. Brocks, P. J. Kelly, and J. van den Brink, *Substrate-induced band gap in graphene on hexagonal boron nitride*, Phys. Rev. B **76**, 073103 (2007).

[35] R. Stacey, *Eliminating lattice fermion doubling*, Phys. Rev. D **26**, 468 (1982).

[36] J. Tworzydło, C. W. Groth, and C. W. J. Beenakker, *Finite difference method for transport properties of massless Dirac fermions*, Phys. Rev. B **78**, 235438 (2008).

[37] L. Susskind, *Lattice fermions*, Phys. Rev. D **16**, 3031 (1977).

[38] A. R. Hernández and C. H. Lewenkopf, *Finite-difference method for transport of two-dimensional massless Dirac fermions in a ribbon geometry*, Phys. Rev. B **86**, 155439 (2012).

[39] C. W. J. Beenakker and L. P. Kouwenhoven, *A road to reality with topological superconductors*, Nature Physics **12**, 618 (2016).

[40] N. Read and D. Green, *Paired states of fermions in two dimensions with breaking of parity and time-reversal symmetries and the fractional quantum Hall effect*, Phys. Rev. B **61**, 10267 (2000).

[41] M. Wimmer, A. R. Akhmerov, M. V. Medvedyeva, J. Tworzydło, and C. W. J. Beenakker, *Majorana bound states without vortices in topological superconductors with electrostatic defects*, Phys. Rev. Lett. **105**, 046803 (2010).

[42] A. F. Tzortzakakis, K. G. Makris, and E. N. Economou, *Non-Hermitian disorder in two-dimensional optical lattices*, Phys. Rev. B **101**, 014202 (2020).

[43] Yi Huang and B. I. Shklovskii, *Anderson transition in three-dimensional non-Hermitian disorder*, arXiv:1911.00562.

[44] D. S. Wiersma, *The physics and applications of random lasers*, Nature Phys. **4**, 359 (2008).

[45] F. Evers and A. D. Mirlin, *Anderson transitions*, Rev. Mod. Phys. **80**, 1355 (2008).

[46] S. Balasubramanian, Y. Liao, and V. Galitski, *Many-body localization landscape*, Phys. Rev. B **101**, 014201 (2020).

[47] C. W. Groth, M. Wimmer, A. R. Akhmerov, and X. Waintal, *Kwant: A software package for quantum transport*, New J. Phys. **16**, 063065 (2014).

[48] Zhicheng Rao, Hang Li, Tiantian Zhang, Shangjie Tian, Chenghe Li, Binbin Fu, Cenyao Tang, Le Wang, Zhilin Li, Wenhui Fan, Jiajun Li, Yaobo Huang, Zhehong Liu, Youwen Long, Chen Fang, Hongming Weng, Youguo Shi, Hechang Lei, Yujie Sun, Tian Qian, and Hong Ding, *Observation of unconventional chiral fermions with long Fermi arcs in CoSi*, Nature **567**, 496 (2019).

[49] D. S. Sanchez, I. Belopolski, T. A. Cochran, X. Xu, J.-X. Yin, G. Chang, W. Xie, K. Manna, V. Süß, C.-Y. Huang, N. Alidoust, D. Multer, S. S. Zhang, N. Shumiya, X. Wang, G.-Q. Wang, T.-R. Chang, C. Felser, S.-Y. Xu, S. Jia, H. Lin, M. Z. Hasan, *Topological chiral crystals with helicoid-arc quantum states*, Nature **567**, 500 (2019).

[50] D. Takane, Z. Wang, S. Souma, K. Nakayama, T. Nakamura, H. Oinuma, Y. Nakata, H. Iwasawa, C. Cacho, T. Kim, K. Horiba, H. Kumigashira, T. Takahashi, Y. Ando, T. Sato, *Observation of chiral fermions with a large topological charge and associated Fermi-arc surface states in CoSi*, Phys. Rev. Lett. **122**, 076402 (2019).

[51] Qian-Qian Yuan, Liqin Zhou, Zhi-Cheng Rao, Shangjie Tian, Wei-Min Zhao, Cheng-Long Xue, Yixuan Liu, Tiantian Zhang, Cen-Yao Tang, Zhi-Qiang Shi, Zhen-Yu Jia1, Hongming Weng, Hong Ding, Yu-Jie Sun, Hechang Lei, and Shao-Chun Li, *Quasiparticle interference evidence of the topological Fermi arc states in chiral fermionic semimetal CoSi*, Science Adv. **5**, eaaw9485 (2019).

[52] N. B. M. Schröter, D. Pei, M. G. Vergniory, Y. Sun, K. Manna, F. de Juan, J.. A. Krieger, V. Süss, M. Schmidt, P. Dudin, B. Bradlyn, T. K. Kim, T. Schmitt, C. Cacho, C. Felser, V. N. Strocov, and Y. Chen, *Chiral topological semimetal with multifold band crossings and long Fermi arcs*, Nature Phys. **15**, 759 (2019).

[53] C.-L. Zhang, F. Schindler, H. Liu, T.-R. Chang, S.-Y. Xu, G. Chang, W. Hua, H. Jiang, Z. Yuan, J. Sun, H.-T. Jeng, H.-Z. Lu, H. Lin, M. Z. Hasan, X. C. Xie, T. Neupert, and S. Jia, *Ultraquantum magnetoresistance in Kramers Weyl semimetal candidate β–Ag_2Se*, Phys. Rev. B **96**, 165148 (2017).

[54] B. Wan, F. Schindler, K. Wang, K. Wu, X. Wan, T. Neupert, and H.-Z. Lu, *Theory for the negative longitudinal magnetoresistance in the quantum limit of Kramers Weyl semimetals*, J. Phys. Condens. Matter **30**, 505501 (2018).

[55] Wen-Yu He, Xiao Yan Xu, K. T. Law, *Kramers Weyl semimetals as quantum solenoids and their applications in spin-orbit torque devices*, arXiv:1905.12575.

[56] R. R. Gerhardts, D. Weiss, and K. von Klitzing, *Novel magnetoresistance oscillations in a periodically modulated two-dimensional electron gas*, Phys. Rev. Lett. **62**, 1173 (1989).

[57] R. W. Winkler, J. P, Kotthaus, and K. Ploog, *Landau band conductivity in a two-dimensional electron system modulated by an artificial one-dimensional superlattice potential*, Phys. Rev. Lett. **62**, 1177 (1989).

[58] C. W. J. Beenakker, *Guiding-center-drift resonance in a periodically modulated two-dimensional electron gas*, Phys. Rev. Lett. **62**, 2020 (1989).

[59] P. Středa and A. H. MacDonald, *Magnetic breakdown and magnetoresistance oscillations in a periodically modulated two-dimensional electron gas*, Phys. Rev. B **41**, 11892 (1990).

[60] V. M. Gvozdikov, *Magnetoresistance oscillations in a periodically modulated two-dimensional electron gas: The magnetic-breakdown approach*, Phys. Rev. B **75**, 115106 (2007).

[61] A. C. Potter, I. Kimchi, and A. Vishwanath, *Quantum oscillations from surface Fermi-arcs in Weyl and Dirac semi-metals*, Nature Comm. **5**, 5161 (2014).

[62] Y. Zhang, D. Bulmash, P. Hosur, A. C. Potter, and A. Vishwanath, *Quantum oscillations from generic surface Fermi arcs and bulk chiral modes in Weyl semimetals*, Sci. Rep. **6**, 23741 (2016).

[63] A. R. Akhmerov and C. W. J. Beenakker, *Boundary conditions for Dirac fermions on a terminated honeycomb lattice*, Phys. Rev. B **77**, 085423 (2008).

[64] M. Z. Hasan, S.-Y. Xu, I. Belopolski, and S.-M. Huang, *Discovery of Weyl fermion semimetals and topological Fermi arc states*, Annu. Rev. Condens. Matter Phys. **8**, 289(2017).

[65] A. A. Burkov, *Weyl Metals*, Annu. Rev. Condens. Matter Phys. **9**, 359 (2018).

[66] N. P. Armitage, E. J. Mele, and A. Vishwanath, *Weyl and Dirac semimetals in three-dimensional solids*, Rev. Mod. Phys. **90**, 15001 (2018).

[67] N. Bovenzi, M. Breitkreiz, T. E. O'Brien, J. Tworzydło, and C. W. J. Beenakker, *Twisted Fermi surface of a thin-film Weyl semimetal*, New J. Phys. **20**, 023023 (2018).

[68] V. Barsan and V. Kuncser, *Exact and approximate analytical solutions of Weiss equation of ferromagnetism and their experimental relevance*, Phil. Mag. Lett. **97**, 359 (2017).

[69] A. B. Pippard, *Magnetic breakdown*, in: *Physics of Solids in Intense Magnetic Fields* (Springer, Boston, 1969).

[70] M. I. Kaganov and A. A. Slutskin, *Coherent magnetic breakdown*, Phys. Rep. **98**, 189 (1983).

[71] R. W. Stark and L. M. Falicov, *Magnetic breakdown in metals*, Prog. Low Temp. Phys **5**, 235 (1967).

[72] V. M. Gvozdikov, *Thermodynamic oscillations in periodic magnetic breakdown structures*, Fiz. Nizk. Temp. **12**, 705 (1986).

[73] A. Alexandradinata and L. Glazman, *Geometric phase and orbital moment in quantization rules for magnetic breakdown*, Phys. Rev. Lett. **119**, 256601 (2017).

[74] M. Breitkreiz, N. Bovenzi, and J. Tworzydło, *Phase shift of cyclotron orbits at type-I and type-II multi-Weyl nodes*, Phys. Rev. B **98**, 121403 (2018).

[75] E. P. Wigner, *Random matrices in physics*, SIAM Rev. **9**, 1 (1967).

[76] F. Haake, S. Gnutzmann, and M. Kuś, *Quantum Signatures of Chaos* (Springer, Berlin, 2018).

[77] F. J. Dyson, *The threefold way: Algebraic structure of symmetry groups and ensembles in quantum mechanics*, J. Math. Phys. **3**, 1199 (1962).

[78] T. Guhr, A. Mueller-Groeling, and H. A. Weidenmüller, *Random matrix theories in quantum physics: common concepts*, Phys. Rep. **299**, 189 (1998).

[79] Ying-Cheng Lai, Hong-Ya Xu, Liang Huang, Celso Grebogi, *Relativistic quantum chaos — An emergent interdisciplinary field*, Chaos **28**, 052101 (2018).

[80] M. Kieburg, J. J. M. Verbaarschot, and S. Zafeiropoulos, *Dirac spectra of two-dimensional QCD-like theories*, Phys. Rev. D **90**, 085013 (2014).

[81] M. Kieburg and T. R. Würfel, *Shift of symmetries of naive and staggered fermions in QCD-like lattice theories*, Phys. Rev. D **96**, 034502 (2017).

[82] C. W. J. Beenakker, *Random-matrix theory of quantum transport*, Rev. Mod. Phys. **69**, 731 (1997).

[83] B. L. Altshuler, *Fluctuations in the extrinsic conductivity of disordered conductors*, JETP Lett. **41**, 648 (1985).

[84] P. A. Lee and A. D. Stone, *Universal conductance fluctuations in metals*, Phys. Rev. Lett. **55**, 1622 (1985).

[85] Our computer codes are available at a repository: 10.5281/zenodo.6394211

[86] Y. Y. Atas, E. Bogomolny, O. Giraud, and G. Roux, *Distribution of the ratio of consecutive level spacings in random matrix ensembles*, Phys. Rev. Lett. **110**, 084101 (2013).

[87] R. Modak and S. Mukerjee, *Finite size scaling in crossover among different random matrix ensembles in microscopic lattice models*, New J. Phys. **16**, 093016 (2014).

[88] H. B. Nielsen and M. Ninomiya, *A no-go theorem for regularizing chiral fermions*, Phys. Lett. B **105**, 219 (1981).

[89] D. B. Kaplan, *Chiral symmetry and lattice fermions*, in: *Modern Perspectives in Lattice QCD: Quantum Field Theory and High Performance Computing*, Lecture Notes of the Les Houches Summer School (Oxford University Press, 2009).

[90] N. P. Ong and Sihang Liang, *Review of experiments on the chiral anomaly in Dirac-Weyl semimetals*, Nature Rev. Phys. **3** 394 (2021).

[91] M. Zahid Hasan, Guoqing Chang, Ilya Belopolski, Guang Bian, Su-Yang Xu, and Jia-Xin Yin, *Weyl, Dirac and high-fold chiral fermions in topological quantum matter*, arXiv:2103.01714, to appear in Nature Rev. Mat. (2021).

[92] H. B. Nielsen and M. Ninomiya, *The Adler-Bell-Jackiw anomaly and Weyl fermions in a crystal*, Nucl. Phys. B **130**, 389 (1983).

[93] D. Kharzeev, *The Chiral Magnetic Effect and anomaly-induced transport*, Progr. Part. Nucl. Phys. **75**, 133 (2014).

[94] A. A. Burkov, *Chiral anomaly and transport in Weyl metals*, J. Phys. Condens. Matter **27**, 113201 (2015).

[95] T. E. O'Brien, C. W. J. Beenakker, and I. Adagideli, *Superconductivity provides access to the chiral magnetic effect of an unpaired Weyl cone*, Phys. Rev. Lett. **118**, 207701 (2017).

[96] M. J. Pacholski, C. W. J. Beenakker, and I. Adagideli, *Topologically protected Landau level in the vortex lattice of a Weyl superconductor*, Phys. Rev. Lett. **121**, 037701 (2018).

[97] G. Lemut, M. J. Pacholski, I. Adagideli, and C. W. J. Beenakker, *Effect of charge renormalization on the electric and thermoelectric transport along the vortex lattice of a Weyl superconductor*, Phys. Rev. B **100**, 035417 (2019).

[98] A. Donís Vela, G. Lemut, M. J. Pacholski, and C. W. J. Beenakker, *Chirality inversion of Majorana edge modes in a Fu-Kane heterostructure*, arXiv:2105.04433.

[99] P. W. Anderson, *Anomalous magnetothermal resistance of high-T_c superconductors: Anomalous cyclotron orbits at a Dirac point*, arXiv:cond-mat/9812063.

[100] Z. Faraei and S. A. Jafari, *Superconducting proximity in three dimensional Dirac materials: odd-frequency, pseudoscalar, pseudovector and tensor-valued superconducting orders*, Phys. Rev. B **96**, 134516 (2017).

[101] G. E. Volovik, *Quantum phase transitions from topology in momentum space*, Lect. Notes Phys. **718**, 31 (2007).

[102] D. F. Agterberg, P. M. R. Brydon, and C. Timm, *Bogoliubov Fermi surfaces in superconductors with broken time-reversal symmetry*, Phys. Rev. Lett. **118**, 127001 (2017).

[103] Noah F. Q. Yuan and Liang Fu, *Zeeman-induced gapless superconductivity with a partial Fermi surface*, Phys. Rev. B **97**, 115139 (2018).

[104] S. Autti, J. T. Mäkinen, J. Rysti, G. E. Volovik, V. V. Zavjalov, and V. B. Eltsov, *Exceeding the Landau speed limit with topological Bogoliubov Fermi surfaces*, Phys. Rev. Res. **2**, 033013 (2020).

[105] J. M. Link and I. F. Herbut, *Bogoliubov-Fermi surfaces in noncentrosymmetric multi-component superconductors*, Phys. Rev. Lett. **125**, 237004 (2020).

[106] Zhen Zhu, Michał Papaj, Xiao-Ang Nie, Hao-Ke Xu, Yi-Sheng Gu, Xu Yang, Dandan Guan, Shiyong Wang, Yaoyi Li, Canhua Liu, Jianlin Luo, Zhu-An Xu, Hao Zheng, Liang Fu, and Jin-Feng Jia, *Discovery of segmented Fermi surface induced by Cooper pair momentum*, arXiv:2010.02216. For a commentary on this experiment, see DOI: 10.36471JCCM_October_2020_01

[107] S. Rachel, L. Fritz, and M. Vojta, *Landau levels of Majorana fermions in a spin liquid*, Phys. Rev. Lett. **116**, 167201 (2016).

[108] B. Perreault, S. Rachel, F. J. Burnell, and J. Knolle, *Majorana Landau-level Raman spectroscopy*, Phys. Rev. B **95**, 184429 (2017).

[109] R. Jackiw and P. Rossi, *Zero modes of the vortex-fermion system*, Nucl. Phys. B **190**, 681 (1981).

[110] The data in Fig. 6.2 is obtained from the tight-binding Hamiltonian (6.14) of the topological insulator layer. The parameters are $\Delta_0 = 20\,\hbar v/d_0$, $d_0 = 302\,a_0$, $B = h/ed_0^2$, $\mu = 0$, $M_0 = 0$, $M_1 = 0.2\,a_0$. The vortex pair in a unit cell is at the positions $(x, y) = (d_0/4)(1, 1)$ and $(d_0/4)(3, 3)$. The superflow momentum K equals $0.8\,\Delta_0/v$ in the left panel and $2\,\Delta_0/v$ in the right panel.

[111] M. I. Katsnelson and M. F. Prokhorova, *Zero-energy states in corrugated bilayer graphene*, Phys. Rev. B **77**, 205424 (2008).

[112] J. Kailasvuori, *Pedestrian index theorem à la Aharonov-Casher for bulk threshold modes in corrugated multilayer graphene*, EPL **87**, 47008 (2009).

[113] Y. Aharonov and A. Casher, *Ground state of a spin-1/2 charged particle in a two-dimensional magnetic field*, Phys. Rev. A **19**, 2461 (1979).

[114] M. Franz and Z. Tešanović, *Quasiparticles in the vortex lattice of unconventional superconductors: Bloch waves or Landau levels?*, Phys. Rev. Lett. **84**, 554 (2000).

[115] Details of the solution of the Helmholtz equation are given in Apps. 6.B and 6.C of the Supplemental Material.

[116] B. Sutherland, *Localization of electronic wave functions due to local topology*, Phys. Rev. B **34**, 5208 (1986).

[117] V. M. Pereira, F. Guinea, J. M. B. Lopes-dos Santos, N. M. R. Peres, and A. H. Castro-Neto, *Disorder induced localized states in graphene*, Phys. Rev. Lett. **96**, 036801 (2006).

[118] Wen-Yu Shan, Hai-Zhou Lu, and Shun-Qing Shen, *Effective continuous model for surface states and thin films of three-dimensional topological insulators*, New J. Phys. **12**, 043048 (2010).

[119] Song-Bo Zhang, Hai-Zhou Lu, and Shun-Qing Shen, *Edge states and integer quantum Hall effect in topological insulator thin films*, Scientif. Rep. **5**, 13277 (2015).

[120] Details of the method of numerical simulation, with supporting data, are given in App. 6.A of the Supplemental Material.

[121] The renormalized charge q_{eff} in the Majorana Landau level is calculated in App. 6.D of the Supplemental Material. That calculation also gives the renormalized Fermi velocity $v_{\text{eff}} = \sqrt{v_x v_y} = \sqrt{q_{\text{eff}}}\, v$ that appears in the Landau level energy E_{L}.

[122] The chiral symmetry at $\mu = 0$ is broken by the mass term $M(k)$ in the Hamiltonian (6.14). This residual chiral symmetry breaking is visible in Fig. 6.3 as a very small splitting of the $\mu = 0$ Landau levels (green flat bands).

[123] The comparison between numerics and analytics in Fig. 6.4 involves no adjustable parameters. To compare the same state in the degenerate zeroth Landau level we choose the state with left-right reflection symmetry. There are two of these, the other is compared in App. 6.E of the Supplemental Material.

[124] Hao-Hua Sun and Jin-Feng Jia, *Detection of Majorana zero mode in the vortex*, npj Quantum Mat. **2**, 34 (2017).

[125] S. Cho, B. Dellabetta, A. Yang, J. Schneeloch, Z. Xu, T. Valla, G. Gu, M. J. Gilbert, and N. Mason, *Symmetry protected Josephson supercurrents in three-dimensional topological insulators*, Nature Comm. **4**, 1689 (2013).

[126] D. I. Pikulin and M. Franz, *Black hole on a chip: proposal for a physical realization of the SYK model in a solid-state system*, Phys. Rev. X **7**, 031006 (2017).
$\mathrm{K}_n(r) = \frac{1}{2}(r/2)^n \int_0^\infty t^{-n-1} \exp(-t - \frac{1}{4}r^2/t)\, dt$, upon the substitution $p = \frac{1}{2}(t - 1/t)$. https://mathoverflow.net/q/379157/11260.

[127] N. B. Kopnin and M. M. Salomaa, *Mutual friction in superfluid ^{3}He: Effects of bound states in the vortex core*, Phys. Rev. B **44**, 9667 (1991).

[128] G. Volovik, *Fermion zero modes on vortices in chiral superconductors*, JETP Lett. **70**, 609 (1999).

[129] S. Frolov, https://espressospin.org/2012/04/18/zen-particle/

[130] C. W. J. Beenakker, *Search for Majorana fermions in superconductors*, Annu. Rev. Con. Mat. Phys. **4**, 113 (2013).

[131] S. Das Sarma, M. Freedman, and C. Nayak *Majorana zero modes and topological quantum computation*, npj Quantum Inf. **1**, 15001 (2015) .

[132] R. M. Lutchyn, E. P. A. M. Bakkers, L. P. Kouwenhoven, P. Krogstrup, C. M. Marcus, and Y. Oreg, *Majorana zero modes in superconductor–semiconductor heterostructures*, Nature Rev. Mat. **3**, 52 (2018).

[133] P. Nozières and W. F. Vinen, *The motion of flux lines in type II superconductors*, Phil. Mag. **14**, 667 (1966) 10.1080/14786436608211964.

[134] Yu. G. Makhlin and G. E. Volovik, *Spectral flow in Josephson junctions and effective Magnus force*, JETP Lett. **62**, 941 (1995).

[135] M. L. Stone, *Spectral flow, Magnus force, and mutual friction via the geometric optics limit of Andreev reflection*, Phys. Rev. B **54**, 13222 (1996).

[136] E. B. Sonin *Magnus force in superfluids and superconductors*, Phys. Rev. B **55**, 485 (1997) 10.1103/PhysRevB.55.485.

[137] M. J. Pacholski, G. Lemut, O. Ovdat, I. Adagideli, and C. W. J. Beenakker, *Deconfinement of Majorana vortex modes produces a superconducting Landau level*, Phys. Rev. Lett. **126**, 226801 (2021).

[138] Zhen Zhu, Michał Papaj, Xiao-Ang Nie, Hao-Ke Xu, Yi-Sheng Gu, Xu Yang, Dandan Guan, Shiyong Wang, Yaoyi Li, Canhua Liu, Jianlin Luo, Zhu-An Xu, Hao Zheng, Liang Fu, and Jin-Feng Jia, *Discovery of segmented Fermi surface induced by Cooper pair momentum*, Science **374**, 1381 (2021).

[139] M. Tinkham, *Introduction to Superconductivity* (Dover, New York, 2004).

[140] D. Xiao, M.-C. Chang, and Q. Niu, *Berry phase effects on electronic properties*, Rev. Mod. Phys. **82**, 1959 (2010) 10.1103/RevModPhys.82.1959.

[141] Zhi Wang, Liang Dong, Cong Xiao, and Qian Niu, *Berry curvature effects on quasiparticle dynamics in superconductors*, Phys. Rev. Lett. **126**, 187001 (2021).

[142] J. R. Clem, *Simple model for the vortex core in a type II superconductor*, J. Low Temp. Phys. **18**, 427 (1975)

[143] T. Kloss, J. Weston, B. Gaury, B. Rossignol, C. Groth, and X. Waintal, *Tkwant: a software package for time-dependent quantum transport*, New J. Phys. **23**, 023025 (2021).

[144] C. Nayak, S. H. Simon, A. Stern, M. Freedman, and S. Das Sarma, *Non-Abelian anyons and topological quantum computation*, Rev. Mod. Phys. **80**, 1083 (2008).

[145] Hong-Hao Tu, Yi Zhang, and Xiao-Liang Qi, *Momentum polarization: An entanglement measure of topological spin and chiral central charge*, Phys. Rev. B **88**, 195412 (2013).

[146] D. Ariad and E. Grosfeld, *Signatures of the topological spin of Josephson vortices in topological superconductors*, Phys. Rev. B **95**, 161401(R) (2017).

Samenvatting

Massaloze fermionen zijn een bijzonder type elementaire excitatie dat kan ontstaan in elektronische systemen. In deze materialen gedragen elektronen zich als massaloze deeltjes, waarmee ze het relativistische gedrag van fotonen nabootsen. De massaloze aard van deze excitaties, samen met hun karakteristieke lineaire dispersierelatie, kan een grote invloed hebben op de macroscopische eigenschappen van elektronische systemen. Sinds de ontdekking van grafeen in 2004 zijn verschillende nieuwe materialen ontdekt die zulke massaloze excitaties bevatten, wat heeft geleid tot interessant en innovatieve toepassingen. Wiskundige methodes uit de topologie hebben ons in staat gesteld om de lage-energie-eigenschappen van veel van dergelijke massaloze systemen te beschrijven en te begrijpen.

Dit proefschrift is gewijd aan het onderzoeken van de effecten van magnetische velden op drie types van massaloze fermionen, genoemd naar hun ontdekkers: Dirac-, Weyl- en Majorana-fermionen. We hebben enkele nieuwe verschijningsvormen ontdekt, we geven aan hoe deze in experimenten kunnen worden gedetecteerd, en we beschrijven theoretische methodes om ze diepgaander te onderzoeken.

Hoofdstuk 2 van dit proefschrift presenteert een nieuwe methode voor het berekenen van een functie (het zogenaamde localisatielandschap), waarmee we kunnen bestuderen hoe massaloze Dirac-fermionen door wanorde worden gelocaliseerd.

De volgende drie hoofdstukken richten zich op Weyl-fermionen. Zo worden massaloze fermionen in een drie-dimensionaal systeem genoemd. In hoofdstukken 3 en 4 richten wij ons op de situatie dat de massaloze eigenschap het gevolg is van Kramers-ontaarding (men spreekt dan ook wel van Kramers-Weyl fermionen). Hoofdstuk 5 voegt supergeleiding toe, we laten zien hoe de elektrische geleiding in de aanwezigheid van een magnetisch veld kan worden gebruikt om de chiraliteit (links- of rechtshandigheid) van de deeltjes te bestuderen.

De laatste twee hoofdstukken van dit proefschrift richten zich op de Majorana-fermionen in het Fu-Kane-model (een topologische isolator in contact met een supergeleider). De Majorana-fermionen zitten vast in een magnetische vortex, maar in hoofdstuk 6 laten we zien dat een superstroom ze uit de vortex kan drijvern. Dit is het gevolg van de Mag-

nuskracht, die werkzaam is ook al zijn de Majorana-fermionen ladingsneutraal. De dynamische eigenschappen van de Magnuskracht onderzoeken we in hoofdstuk 7.

Summary

Massless fermions are a unique type of elementary excitation that can arise in electronic systems. In such materials, electrons behave as massless particles, mimicking the relativistic behavior of photons. The massless nature of these excitations, along with their characteristic linear dispersion, can have a major impact on the macroscopic properties of electronic systems. Since the discovery of graphene in 2004, several new materials have been discovered that contain such massless excitations, leading to interesting and innovative applications. Mathematical methods from topology have enabled us to describe and understand the low-energy properties of many such massless systems, facilitating the use of strong analytical and numerical tools for their study.

This thesis is dedicated to investigating the effects of magnetic fields on massless topological systems, with a focus on those that exhibit Dirac, Weyl, and Majorana fermions, named after their discoverers. Its main contribution lies in the discovery of new sub-gap states, identification of their experimental signatures, and development of new techniques for the study of such condensed matter systems.

Chapter 2 presents a new method for computing a function, called the "localization landscape", which allows us to study how massless Dirac fermions are localized by disorder.

The next three chapters focus on Weyl fermions, which are what massless fermions are called in a three-dimensional system. In chapters 3 and 4, we focus on the situation where the massless property is the result of Kramers degeneracy (also known as Kramers-Weyl fermions). Here, we find new signatures in the magnetoconductance and spectral behavior that are unique to this class of systems. In Chapter 5, we add superconductivity and show how the electrical conductivity in the presence of a magnetic field can be used to study the chirality (left- or right-handedness) of the particles.

The last two chapters of this thesis focus on Majorana fermions in the Fu-Kane model (a topological insulator in contact with a superconductor). The Majorana fermions are trapped in a magnetic vortex, but in Chapter 6, we show that a supercurrent can drive them out of the vortex, giving rise to a new extended zero-mode solution. This is due to the Magnus force,

which is active even though the Majorana fermions are charge-neutral. We explore the dynamic properties of the Magnus force in Chapter 7.

Curriculum Vitæ

I was born on the 14th of December 1994, in Postojna, Slovenia and grew up in a small village outside of Ajdovščina. During my primary school, I quickly became interested in mathematics, physics and astronomy. With the help of my motivating teachers, I continued this passion throughout my high school, where I competed in various national competitions and joined a local astronomical society.

In 2013, I began my Bachelor's studies in Physics at the University of Ljubljana, where I discovered my interest for theoretical physics, in particular the field of condensed matter physics. Outside of classes, I pursued astrophotography and continued to assist with astronomy camps for kids and students.

After completing my Bachelor's Degree, I secured an internship in 2016 at the Jozef Stefan Institute, working under Prof. dr. Janez Bonča on many-body localization, co-authoring my first publication. In 2017, I moved to Leiden, Netherlands, to pursue a Master's Degree in Theoretical Physics, graduating with summa cum laude honors for my research on the transport properties of a Weyl superconductor in a vortex lattice, under the guidance of Prof. dr. Carlo Beenakker. In 2019, I began my PhD studies at the Lorentz Institute, continuing my work in Beenakker's theoretical nanophysics group. I focused on the study of topological systems in the presence of a magnetic field, with a particular emphasis on studying Weyl, Dirac, and Majorana fermions. Throughout my PhD, I participated in various conferences and summer schools, expanding my knowledge and presenting my research. I also worked as a teaching assistant for courses in computational physics, quantum theory, and quantum information, earning the Teaching Assistant Prize in 2023 for my contributions to the latter course.

Going forward, I will join the Free University of Berlin, as a postdoctoral researcher in the group of Prof. dr. Piet Brouwer. There I will delve deeper into the study of topological systems and other novel phenomena emerging in the field of condensed matter physics.

List of publications

[1] G. Lemut, M. J. Pacholski, S. Plugge, C. W. J. Beenakker and İ. Adagideli, *Magnus effect on a Majorana zero-mode*, arXiv:2303.05959, (2023) [Chapter 7].

[2] C. W. J. Beenakker, A. Donís Vela, G. Lemut, M. J. Pacholski and J. Tworzydło, *Tangent fermions: Dirac or Majorana fermions on a lattice without fermion doubling*, arXiv:2302.12793, (2023).

[3] A. Donís Vela, G. Lemut, J. Tworzydło and C. W. J. Beenakker, *Method to preserve the chiral-symmetry protection of the zeroth Landau level on a two-dimensional lattice*, Annals of Physics, 169208, (2023).

[4] A. Donís Vela, G. Lemut, M. J. Pacholski, J. Tworzydło and C. W. J. Beenakker, *Reflectionless Klein tunneling of Dirac fermions: comparison of split-operator and staggered-lattice discretization of the Dirac equation*, J. Phys. Cond. Matt. **34**, 364003 (2022).

[5] A. Donís Vela, M. J. Pacholski, G. Lemut, J. Tworzydło and C. W. J. Beenakker, *Massless Dirac fermions on a space-time lattice with a topologically protected Dirac cone*, Annalen der Physik **534**, 2200206, (2022).

[6] G. Lemut, M. J. Pacholski, J. Tworzydło and C. W. J. Beenakker, *Supercell symmetry modified spectral statistics of Kramers-Weyl fermions*, J. Phys. A: Math. Theor. **55**, 234003 (2022) [Chapter 4].

[7] M. J. Pacholski, G. Lemut, J. Tworzydło and C. W. J. Beenakker, *Generalized eigenproblem without fermion doubling for Dirac fermions on a lattice*, SciPost Physics **11**, 105 (2021).

[8] A. Donís Vela, G. Lemut, M. J. Pacholski and C. W. J. Beenakker, *Chirality inversion of Majorana edge modes in a Fu-Kane heterostructure*, New J. Phys. **23**, 103006 (2021).

[9] G. Lemut, M. J. Pacholski and C. W. J. Beenakker, *Chiral charge transfer along magnetic field lines in a Weyl superconductor*, Phys. Rev. B **104**, 125444 (2021) [Chapter 5].

[10] M. J. Pacholski, G. Lemut, O. Ovdat, İ. Adagideli and C. W. J. Beenakker, *Deconfinement of Majorana vortex modes produces a superconducting Landau level*, Phys. Rev. Lett. **126**, 226801 (2021) [Chapter 6].

[11] G. Lemut, A. Donís Vela, M. J. Pacholski, J. Tworzydło and C. W. J. Beenakker, *Magnetic breakdown spectrum of a Kramers-Weyl semimetal*, New J. Phys. **22**, 093022 (2020) [Chapter 3].

[12] G. Lemut, M. J. Pacholski, O. Ovdat, A. Grabsch, J. Tworzydło and C. W. J. Beenakker, *Localization landscape for Dirac fermions*, Phys. Rev. B **101**, 081405(R) (2020) [Chapter 2].

[13] G. Lemut, M. J. Pacholski, İ. Adagideli and C. W. J. Beenakker, *Effect of charge renormalization on electric and thermo-electric transport along the vortex lattice of a Weyl superconductor*, Phys. Rev. B **100**, 035417 (2019).

[14] G. Lemut, M. Mierzejewski and J. Bonča, *Complete Many-Body Localization in the t-J Model Caused by a Random Magnetic Field*, Phys. Rev. Lett. **119**, 246601 (2017).